GEOLOGICAL SURVEY OF CANADA
CURRENT RESEARCH 1999-F

RADIOGENIC AGE AND ISOTOPIC STUDIES: REPORT 12

1999

Natural Resources Canada Ressources naturelles Canada

GEOLOGICAL SURVEY OF CANADA
CURRENT RESEARCH 1999-F

RADIOGENIC AGE AND ISOTOPIC STUDIES: REPORT 12

1999

Catalogue No. M44-1999/6E
ISBN 0-660-17747-1

Available in Canada from
Geological Survey of Canada offices:

601 Booth Street
Ottawa, Ontario K1A 0E8

3303-33rd Street N.W.
Calgary, Alberta T2L 2A7

101-605 Robson Street
Vancouver, B.C. V6B 5J3

A deposit copy of this publication is also available for reference
in selected public libraries across Canada

Price subject to change without notice

Cover illustration

The ca. 4100 m above sea level Crucero Depression of the southeastern Peruvian Andes, an intermontane basin bounded to the northeast by snow-covered peaks of the Cordillera de Carabaya. The basin is filled by Eocene and younger sedimentary and volcanic rocks, including the Cerro Huancahuancane Formation, the host unit for sample MAC-83 (*see* Sandeman et al., p. 13–26). The sample was prepared as an international interlaboratory calibration standard through a partnership with Queen's University.

Photo en page couverture

La dépression de Crucero, qui se trouve à environ 4 100 m au-dessus du niveau de la mer dans le sud-est des Andes du Pérou, est un bassin intermontagneux qui est limité au nord par les pics enneigés de la Cordillera de Carabaya. Le bassin est comblé de roches volcaniques et sédimentaires éocènes et plus jeunes, y compris les roches de la Formation de Cerro Huancahuancane, d'où provient l'échantillon MAC-83 (voir Sandeman et al., p. 13–26). L'échantillon a été préparé dans le cadre d'un partenariat avec l'Université Queen's et servira d'étalon international interlaboratoire.

CONTENTS

RADIOGENIC AGE AND ISOTOPIC STUDIES: REPORT 12

INTRODUCTION

Radiogenic Age and Isotopic Studies is an annual report on recently obtained radiometric age and tracer isotope data generated by the Geochronology Subdivision at the Geological Survey of Canada. Report 12 consists of six papers on various geoscience research topics within the fields of U-Pb and ^{40}Ar-^{39}Ar geochronology as well as Sm-Nd isotopic tracer studies. Readers are reminded that the contributions often contain provisional results and interpretations of ongoing research, or consist of completed studies of limited scope. Typically, articles of greater depth and magnitude are published in external journals. A list of such recent works as well as other publications that report data from the GSC Geochronology Laboratory is provided at the end of this volume. Two open file geochronogical compilations on Archean rocks of the Canadian Shield are also listed. These compilations are now on the network. All articles published since 1987 in Radiogenic Age and Isotopic Studies reports 1 to 12 are listed on the GSC Geochronology Laboratory web page (http://gis.NRCan.gc.ca/cgd/geochron/gl_main.htm).

In this report, a method is described for converting digital photographs of mineral grains to weights, thereby obviating the need for the time-consuming procedure of weighing on a microbalance. Microchemistry techniques for extracting Pb from mineral and organic samples for thermal ionization mass spectrometry (TIMS) analysis are also described. A third technical paper characterizes in detail an interlaboratory standard for ^{40}Ar-^{39}Ar analysis. Reports herein of geochronogical applications present brief regional and local field settings and relate data in an appropriate geological context. Two papers present Nd isotopic data obtained under the umbrella of the Western Churchill NATMAP Project. One paper presents ^{40}Ar-^{39}Ar data that provides absolute data about a detailed magnetostratigraphic study.

The continued vitality of the Geochronology Subdivision's program would not be possible without the diligent work of its support staff. Gerry Gagnon and Ron Christie produce pure mineral separates from rock specimens. Fred Quigg assures continued production of $^{40}Ar/^{39}Ar$ data. Diane Bellerive and Jack MacRae perform the delicate procedures to extract nanogram levels of Pb and U from carefully selected mineral separates. Klaus Santowski and Carole Lafontaine meticulously measure isotopic ratios on a solid source mass spectrometer. Natalie Morisset plays a vital role in supporting SHRIMP ion microprobe operations, from sample preparation to data collection. All are warmly thanked for their reliability and commitment.

INTRODUCTION

La Sous-division de la géochronologie de la Commission géologique du Canada publie un rapport annuel sur la datation radiométrique et les études isotopiques afin de diffuser les données de datation radiométrique et de traceurs isotopiques récemment acquises. Le rapport n° 12 fait état de six études traitant de divers sujets dans les domaines de la géochronologie U-Pb et ^{40}Ar-^{39}Ar et des études des traceurs isotopiques Sm-Nd. On rappelle aux lecteurs que les interprétations comprennent souvent des résultats et des interprétations provisoires issus de recherches en cours ou consistent en études complétées d'envergure restreinte. Des articles plus approfondis sont publiés d'ordinaire dans des revues de l'extérieur. Une liste de tels travaux récents ainsi que d'autres publications faisant état de données du Laboratoire de géochronologie de la CGC est fournie à la fin du présent ouvrage. Deux compilations de données géochronologiques sous forme de dossiers publics visant les roches de l'Archéen du Bouclier canadien figurent également dans cette liste et sont maintenant disponibles sur le réseau. Tous les articles publiés depuis 1987 dans les rapports n^{os} 1 à 12 de la CGC sur la datation radiométrique et les études isotopiques sont énumérés à la page Web du Laboratoire de géochronologie de la CGC (http://gis.NRCan.gc.ca/cgd/geochron/gl_main.htm).

Dans le présent rapport, on décrit une méthode permettant la conversion en poids de photographies numériques de grains de minéraux, qui élimine la nécessité de la chronophage procédure de la pesée à la microbalance. On décrit également des méthodes microchimiques d'extraction du Pb d'échantillons minéraux et organiques à soumettre à l'analyse par thermo-ionisation et spectrométrie de masse (TIMS). Dans une troisième étude technique, on caractérise de manière détaillée une norme interlaboratoire pour les analyses ^{40}Ar-^{39}Ar. Les rapports sur des applications en géochronologie présentent brièvement les cadres régionaux et locaux et y relient les données dans un contexte géologique approprié. Dans deux des études on présente des données isotopiques pour le Nd obtenues dans le cadre du Projet de la Province de Churchill occidentale du CARTNAT. Dans une autre des études on présente les données ^{40}Ar-^{39}Ar recueillies dans le cadre d'une étude magnétostratigraphique détaillée.

Le maintien de la vitalité du programme de la Sous-division de la géochronologie serait impossible sans le travail assidu de son personnel. Gerry Gagnon et Ron Christie produisent des extraits purs de minéraux à partir d'échantillons de roches. Fred Quigg assure la production continue de données $^{40}Ar/^{39}Ar$. Diane Bellerive et Jack MacRae exécutent les délicates procédures d'extraction de quantités de Pb et d'U de l'ordre du nanogramme d'extraits de minéraux sélectionnés avec soin. Klaus Santowski et Carole Lafontaine mesurent méticuleusement les rapports isotopiques au spectromètre de masse à source solide. Natalie Morisset joue un rôle essentiel à l'appui de l'utilisation de la microsonde ionique SHRIMP, depuis la préparation des échantillons jusqu'à la collecte des données. Tous sont chaleureusement remerciés pour leur assiduité et leur engagement.

Otto van Breemen

– 1 –

A practical image analysis technique for estimating the weight of abraded mineral fractions used in U-Pb age dating

W. Matthews[2] and W.J. Davis[1]

Matthews, W. and Davis, W.J., 1999: A practical image analysis technique for estimating the weight of abraded mineral fractions used in U-Pb age dating; in *Radiogenic Age and Isotopic Studies: Report 12; Geological Survey of Canada, Current Research 1999-F, p. 1–7.*

Abstract: A simple method for estimating the weight of abraded zircon grains from a digital photomicrograph is presented. It requires less than five minutes, uses image analysis software to determine the lengths of the two principal axes of a zircon grain from a digital image, and, combined with user-specified morphological characteristics, calculates the weight using an empirically derived factor. The accuracy of the method is demonstrated using ten abraded zircon fractions of varied morphologies and sizes. Model weight calculations for nine of the ten samples are within ±10 per cent of the weights measured by an electronic microbalance. The method can be used for single grains or individual grains in a multigrain fraction. This method is unlikely to eliminate entirely the need to weigh zircon samples, but it will help reduce or eliminate grain loss between the selection and microchemistry stages for many analyses.

Résumé : On présente une méthode simple permettant d'estimer le poids de grains de zircon abrasés à partir d'une photomicrographie numérique. Cette méthode exige moins de cinq minutes, fait appel à un logiciel d'analyse d'images pour déterminer la longueur des deux axes principaux d'un grain de zircon sur une image numérique et, grâce aux caractéristiques morphologiques précisées par l'utilisateur, calcule le poids en utilisant un facteur empirique. On illustre la précision de la méthode en utilisant dix fractions de zircon abrasé de morphologie et de taille diverses. Dans neuf des dix échantillons, le poids calculé avec le modèle concorde à ±10 p. 100 avec le poids mesuré avec une microbalance électronique. La méthode peut être utilisée pour mesurer la taille de grains uniques ou de grains individuels dans une fraction multigrains. Elle n'éliminera probablement pas entièrement la pesée des échantillons de zircon, mais elle permettra de réduire ou d'éliminer la perte de grains entre les étapes de la sélection et de l'analyse microchimique lors de nombreuses analyses.

---

[1] Geological Survey of Canada, 601 Booth Street, Ottawa, Ontario K1A 0E8

[2] Department of Earth Sciences, University of Waterloo, Waterloo, Ontario, Canada N2L 3G1

INTRODUCTION

Improvements in procedural blank lead levels (Krogh, 1973; 1982; Parrish et al., 1987) and mass spectrometry (Roddick et al., 1987) routinely permit precise Th-U-Pb isotopic ratios to be determined on zircon samples weighing less than a few micrograms. While allowing for more intricate and detailed geochronological studies, the small sample sizes introduce considerable difficulty in manipulating and weighing samples in the clean laboratory prior to analysis. Zircon fractions can be weighed using an electronic microbalance to precisions of better than ±1 µg (Parrish et al. 1987). However, the precise determination of the weight of a zircon fraction is required only to determine the concentration of Th, U, and Pb by isotope dilution, but not the precision of isotopic ratios. Uncertainty in concentration data does not affect the calculation of U-Pb ages, nor the reliability of geochronological interpretations. Concentration data is often useful to characterize different zircon populations in a quantitative fashion and may provide information useful in interpreting mixing arrays on concordia diagrams, or petrogenetic interpretations. For the most part, concentration data is not typically used at the confidence level achieved by careful weighing and isotope dilution analysis.

The manipulation of extremely small (<1 to 3 µg) samples during the weighing process may lead to grain loss, or increased blank lead levels due to excessive handling, and may ultimately compromise the quality of the isotopic analysis. To avoid these problems, a simple method was developed that uses image analysis software to measure dimensions of abraded zircon grains from a digital photomicrograph and calculate weights of individual grains. The method was developed empirically using a data set of 25 precisely weighed zircon fractions. We estimate the accuracy of the method to be better than ±15 per cent for abraded, subelliptical zircon grains. This level of accuracy is satisfactory for many geochronological applications, but direct weighing of samples will be necessary in those cases requiring precise concentration data.

IMAGE ACQUISITION, EDITING, AND ANALYSIS

Digital images of zircon and other mineral samples are acquired using a Kodak™ DCS200 24 bit digital camera mounted on a Nikon™ binocular petrographic microscope. The camera is operated via a TWAIN driver from Adobe Photoshop IV™. The digital images are stored for archival purposes. Editing and analysis of the digital image are performed entirely within Adobe Photoshop IV™. Image analysis is performed using plug-in filters available in the Image Analysis Tool Kit V.2.5™ by Reindeer Games[2]. The image analysis software can recognize and identify individual grains and measure various parameters from calibrated digital images, including length of major and orthogonal axes, area, and perimeter. The dimensions of the images are calibrated relative to a scale bar of known length appropriate to the magnification of the image.

The recognition and identification of grains by the image analysis plug-ins is improved if the scale bar and all blemishes are removed from the image and the background is uniformly white. Juxtaposed grains must be separated so that the software can distinguish and accurately measure each individual grain. This can be accomplished either by erasing a small number of pixels between adjoining grains or by selecting and moving entire grains using Adobe editing tools.

The data measured by the image analysis software is stored in a text file along with grain identifier information and other morphological characteristics. The text file is imported into a spreadsheet that calculates a model weight for each individual grain. The basis for the calculations are described below. An example of the output from the spreadsheet program is shown in Figure 1. The total process from acquiring the image of the grains, through image analysis, and spreadsheet calculations requires approximately 3 minutes per sample. On average, this procedure is significantly quicker than weighing fractions using an electronic scale, which may take 5 to 10 minutes under ideal conditions, to as long as 15 minutes.

ESTIMATION OF WEIGHT FROM TWO DIMENSIONAL PARAMETERS

The morphology of abraded zircon grains most closely resembles an ellipsoid, depending on original grain shape and the extent of abrasion and rounding. The volume of a symmetrical ellipse is given by the following:

$$v = \frac{4}{3}\pi abc \qquad (1)$$

where a, b, and c equal half of the principal axis D_1, D_2, and D_3, respectively. For the special case of a sphere, $a = b = c$. The weight of a mineral grain of known volume can then be calculated from the following:

$$w = v \bullet \rho \qquad (2)$$

where v = the calculated volume (equation 1) and ρ is the density of the mineral. In the case of zircon, the density is assumed to be 4.7 g/cc^3.

The volume and weight of a symmetrical ellipsoid zircon grain can be calculated from the principal (D_1) and secondary axes (D_2) measured by the image analysis software, and a visual estimate of the third axis (D_3) in proportion to the (D_2) axis. In most cases, the minimum axis (D_3) is oriented vertically. Although crystal thickness (D_3) could be more accurately determined by focusing through the grain using a calibrated microscope stage, to save time, a visual estimate of the third axis was found to be suitable for the empirical approach adopted here.

---

[2] Reindeer Games, Inc., One North Pack Square, Suite 419, Asheville, North Carolina 28801

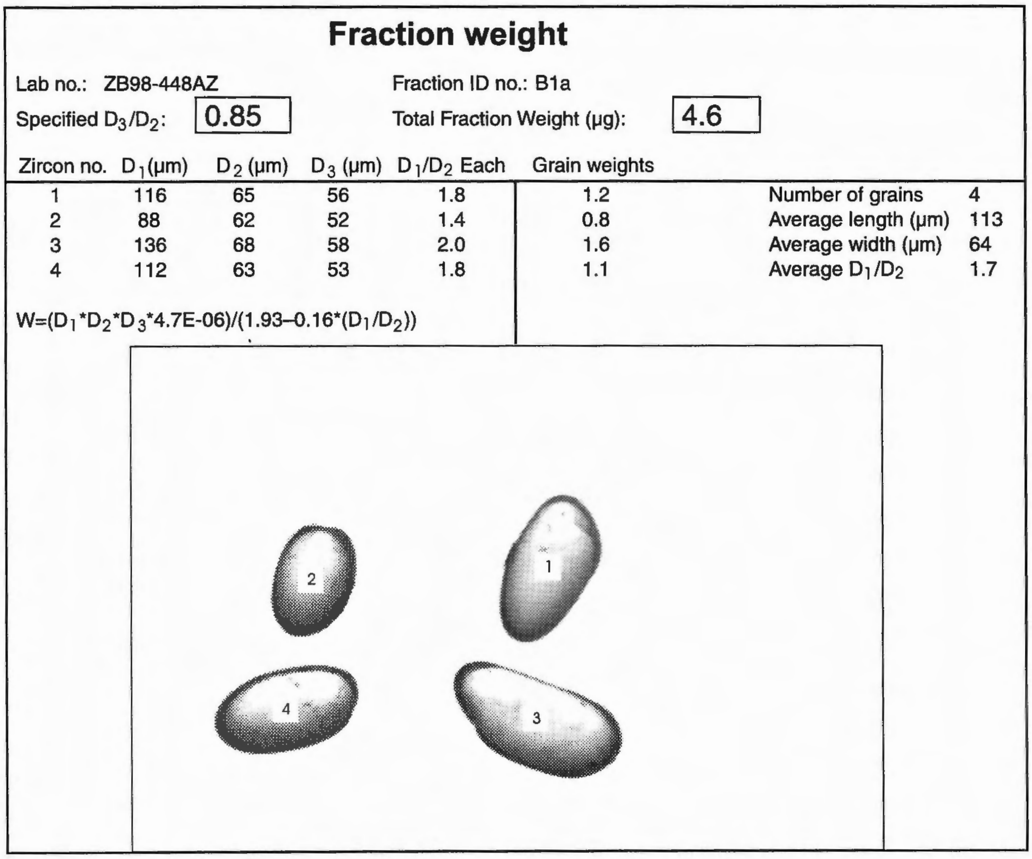

Fraction weight

Lab no.: ZB98-448AZ

Fraction ID no.: B1a

Specified D_3/D_2: 0.85

Total Fraction Weight (µg): 4.6

Zircon no.	D_1 (µm)	D_2 (µm)	D_3 (µm)	D_1/D_2 Each	Grain weights
1	116	65	56	1.8	1.2
2	88	62	52	1.4	0.8
3	136	68	58	2.0	1.6
4	112	63	53	1.8	1.1

Number of grains	4
Average length (µm)	113
Average width (µm)	64
Average D_1/D_2	1.7

$W=(D_1*D_2*D_3*4.7E\text{-}06)/(1.93-0.16*(D_1/D_2))$

Figure 1. Example of the results file from the spreadsheet program including an image of the grains analyzed.

The applicability of this approach was first tested on a set of 25 single and multigrain zircon fractions of varied grain morphologies (Table 1). Precise, measured weights (±1 µg) for these fractions are presented in Table 1. Grain dimensions (D_1 and D_2) were determined with the image analysis software, the ratio of D_3 to D_2 was visually estimated, and the weights were calculated using equations (1) and (2). The assumption of a symmetrical ellipsoidal morphology consistently yielded weights less than the precisely measured weights determined using the electronic balance (Table1; Fig 2).

To overcome this shape problem, we empirically calculated a morphological correction factor based on grain elongation. This factor was determined by first calculating the weight of grains assuming a prismatic, rectangular habit, where:

$$w = D_1 \bullet D_2 \bullet D_3 \bullet \rho \qquad (3)$$

Orthorhombic model weights for all 25 fractions estimated by this method are consistently higher than measured values (Table 1; Fig. 2). A correction factor (CF) for each fraction was determined to adjust the model weight determined from equation (3) to the measured weight. The calculated correction factors are presented in Table 1.

Figure 3 plots the correction factors for each of the 25 fractions against average aspect ratio (D_1/D_2) as a measure of grain morphology. Although there is considerable scatter on this diagram, the correction factor correlates negatively with grain elongation. The best-fit line determined by least squares linear regression of this data set is defined by the following:

$$CF = 1.93 - 0.16(D_1/D_2) \qquad (4)$$

This relationship suggests that the shape of elongate grains following abrasion more closely resembles a prism with rounded corners, whereas more equant grains approach more perfect ellipsoids.

The weight can then be estimated from the following:

$$w = D_1 \bullet D_2 \bullet D_3 \bullet \rho / CF \qquad (5)$$

It is evident that this relationship can only be appropriate over a finite range in aspect ratio. For example, at grain elongations greater than 5.8, the correction factor would be less than 1 and would increase the weight relative to that of a

Figure 2.

Plot of calculated model weight versus measured weight for the developmental data set of 25 samples. Open circles indicate weight calculated assuming ellipsoidal morphology and using equations 1 and 2; open squares indicate weights assuming prismatic shape (equation 3); filled triangles indicate corrected weight (equation 5). The solid line is for reference and traces 1:1 correlation.

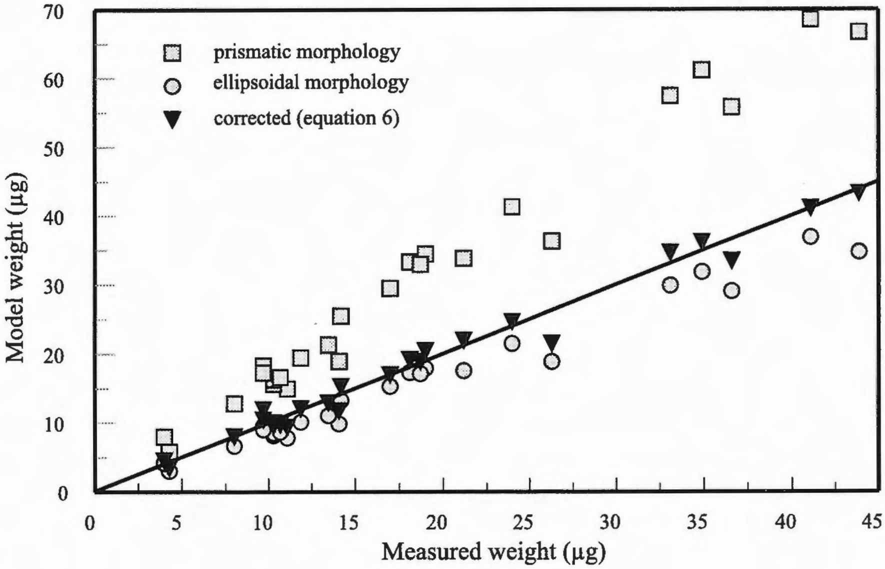

Table 1. Dimensional parameters and weights of zircon fractions used in the empirical calibration.

Sample number	Number of grains	Average aspect ratio	D_3/D_2	Measured weight[b] (μg)	Ellipsoid weight[c] (μg)	Prism weight[c] (μg)	Model weight[d] (μg)	Relative difference[e] (%)	Correction factor (CF)
1	16	2.5	0.85[a]	9.7	9.5	18.3	12.0	23.5	1.89
2	18	2.5	0.85	21.2	17.6	33.8	22.0	3.8	1.60
3	6	2.5	0.90[a]	43.9	34.7	66.7	43.3	-1.3	1.52
4	12	2.1	0.85[a]	11.1	7.8	15.0	9.4	-15.2	1.35
5	15	2.1	0.85[a]	8.0	6.7	12.8	8.1	0.6	1.60
6	12	2.0	0.85[a]	11.9	10.2	19.5	12.1	1.8	1.64
7	1	2.0	0.85[a]	14.1	9.9	19.0	11.8	-16.2	1.35
8	6	1.9	0.85[a]	10.3	8.2	15.7	9.6	-6.5	1.52
9	12	1.9	0.85[a]	10.3	8.5	16.3	10.0	-2.5	1.59
10	1	1.8	0.85[a]	9.7	9.0	17.3	10.5	8.3	1.79
11	8	1.8	0.75	13.5	11.1	21.3	13.0	-3.8	1.58
12	1	1.7	0.85[a]	33.1	29.9	57.5	34.7	4.8	1.74
13	15	1.7	0.85[a]	4.3	3.0	5.8	3.5	-18.2	1.36
14	1	1.7	0.80[a]	14.2	13.3	25.5	15.4	8.3	1.80
15	1	1.6	0.75[a]	19.0	18.0	34.5	20.5	8.0	1.82
16	5	1.6	0.90	24.0	21.5	41.3	24.7	2.9	1.72
17	10	1.6	0.80	36.6	29.1	55.8	33.4	-8.6	1.53
18	1	1.5	0.85[a]	34.9	31.9	61.2	36.2	3.7	1.75
19	15	1.5	0.75	26.3	18.9	36.3	21.5	-18.2	1.38
20	1	1.4	0.85[a]	10.7	8.7	16.7	9.8	-8.5	1.56
21	1	1.3	0.85[a]	17.0	15.4	29.5	17.1	0.4	1.74
22	1	1.3	0.85[a]	41.1	36.9	70.8	41.1	0.1	1.72
23	5	1.3	0.85[a]	18.1	17.4	33.3	19.3	6.5	1.84
24	5	1.2	0.85[a]	18.7	17.2	33.0	19.0	1.6	1.76
25	4	1.1	0.85	4.0	4.2	8.0	4.6	14.3	2.00

Aspect ratio = D_1/D_2
a – estimated from archival image
b – measured weight (±1 μg)
c – ellipsoid weight calculated using equations 1and 2; prism weight from equation 3
d – model weight calculated using equation 5
e – relative difference between model and measured weight
Correction factor = prism weight/measured weight

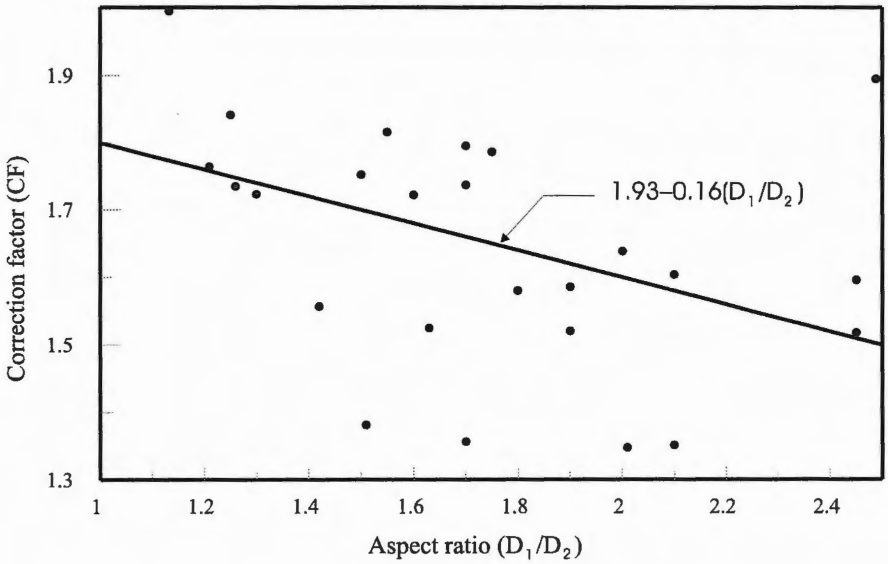

Figure 3.

Plot of correction factor versus aspect ratio. The correction factor equals the weight of prism/measured weight. The average aspect ratio (D_1/D_2) of the fraction is measured by image analysis software. The negatively sloping solid line is least squares best fit line to data, relating correction factor to aspect ratio.

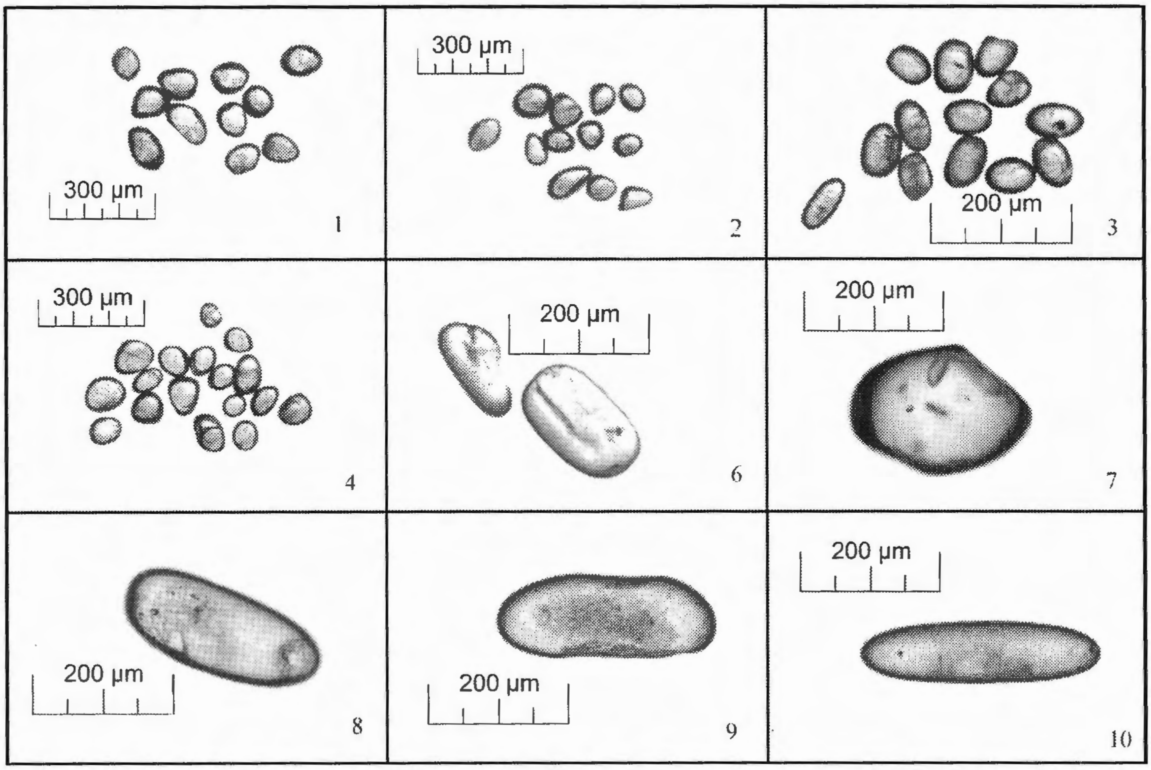

Figure 4. *Digital photomicrographs of zircon fractions used to test the empirical calibration method. Fraction 5 is not shown. The numbers are crossreferenced to Table 2 and Figure 5.*

prism, which is clearly impossible. For this reason, weights of grains with elongations greater than 2.5 are corrected by a fixed factor of 1.5, the approximate correction factor at the high end of the calibrated range. In our experience, relatively few abraded zircon grains lie significantly outside the calibrated range shown in Figure 3.

Corrected weights of the 25 samples using equation 5 are shown in Figure 2 and Table 1. The majority of the fractions (76 per cent) yield corrected weights within 10 per cent of their measured values, with a maximum difference of 23 per cent.

The method was independently tested using a set of 10 precisely weighed zircon fractions. These fractions were selected to test the method for a broader range of morphologies than were present in the developmental data set. Photomicrographs of most of the fractions are presented in Figure 4 and the calculated weights are given in Table 2 and shown graphically in Figure 5. With one exception, discussed below, the calculated weights approximate the measured values to within better than 10 per cent.

Figure 5.

Plot of model weight versus measured weight for 10 zircon fractions. The solid line is for reference and traces 1:1 correlation. The shaded field outlines area ±10 per cent from the reference line.

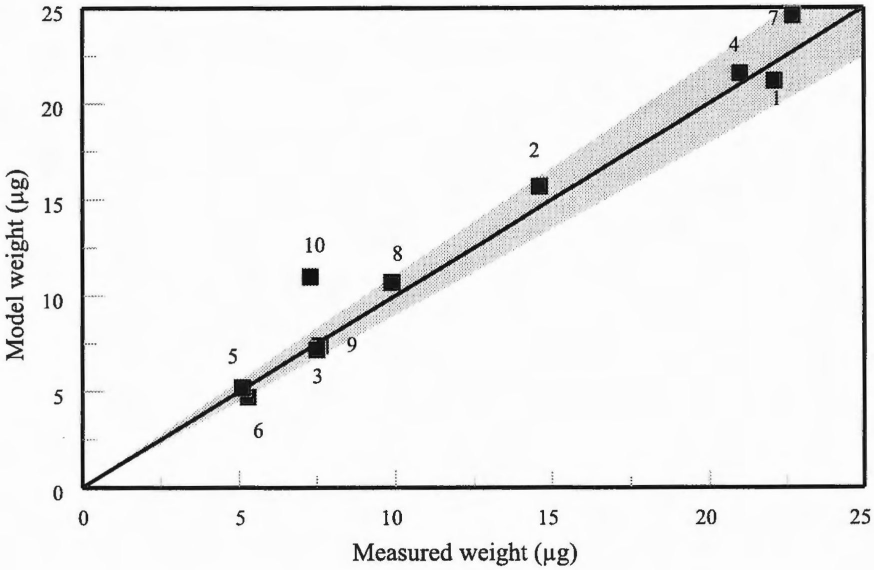

Table 2. Dimensional parameters and weights of zircon fractions of test data set.

Sample number	Number of grains in fraction	Average aspect ratio	D_3/D_2	Measured weight^a (μg)	Model weight^b (μg)	Relative difference (%)
1	11	1.3	0.75	22.1	21.2	-4.1
2	12	1.4	0.70	14.6	15.7	7.5
3	14	1.5	0.95	7.6	7.4	-2.6
4	17	1.3	0.70	21.0	21.6	2.9
5	2	1.6	0.85	5.3	4.7	-10.9
6	2	1.8	0.50	5.1	5.2	2.0
7	1	1.4	1.00	22.7	24.6	8.6
8	1	2.3	0.75	9.9	10.7	8.1
9	1	2.6	0.50	7.5	7.2	-4.0
10	1	3.8	1.00	7.3	11.0	46.7

Images for all grains excluding no. 5 are shown in Figure 4.
Aspect ratio = D_1/D_2
a – measured weight (±1 μg)
b – model weight using equation 5

As noted above and in Table 1, the correction factor was developed using grains with aspect ratios (D_1/D_2) between 2.5:1 and 1.1:1 and D_3/D_2 ratios in the range of 0.75 to 0.9 (Table 2; Fig. 5). Results for fractions 1, 5, and 8 demonstrate the accuracy of our approach within the above range. Fractions 2, 3, 4, 6, 7, and 9 all have D_3/D_2 ratios slightly outside the above range, yet comparable accuracy is achieved. Only sample 10, an elongate grain with an aspect ratio of 3.8:1 and circular cross-section, yielded a poor result. Further work is required to calibrate the method for grain elongations greater than 3.

DISCUSSION AND LIMITATIONS OF THE METHOD

The application of this image analysis technique has a number of specific limitations. In particular, grain shape is very important to achieving accurate results. The empirical correction factor was calibrated only for abraded grains with approximately symmetrical ellipsoid shapes and aspect ratios of 1:1 to 3:1, similar to those seen in Figure 4. Although some variation and irregularity may be tolerated, samples not conforming to the studied range of morphologies (such as irregular fragments or grain tips) are not presently suitable for weight calculation using this method. Weight calculations of grains with aspect ratios greater than approximately 3:1 are not well calibrated and may produce less accurate results. Further development of the method may accommodate a broader range of aspect ratios and grain shapes including non-abraded morphologies.

This method is not limited to zircon and could be applied to other minerals used in geochronology. Monazite often displays an equant, subrounded morphology. With monazite samples containing sufficient uranium to allow <1 μg samples to be analyzed, these samples present the same difficulties as zircon analyses. Modifications to the correction factor and density used in the weight calculation likely would lead to results similar to those shown here for zircon. Baddeleyite varies considerably less in morphology than monazite or zircon and a different approach, perhaps based on the area of the baddeleyite grains in plan view, is likely to produce satisfactory results.

In summary, image analysis of digital photomicrographs can accurately estimate weights of abraded zircon grains to within better than 15 per cent of measured values. The method is suitable to determine semiquantitative concentration data appropriate for broad characterization of potentially different zircon populations within a sample. Although the method outlined here is specific to a certain grain morphology, it can be readily modified to accommodate a broader range of grain shapes and mineral types.

ACKNOWLEDGMENTS

We would like to thank Jack Macrae for precisely weighing the mineral fractions used in this study. Pat Hunt directed us to the Adobe-compatible image analysis software. Reg Thériault, Vicki McNicoll, Tom Skulski and Otto van Breemen are thanked for comments and suggestions concerning earlier versions of the manuscript.

REFERENCES

Krogh, T.E.
1973: A low contamination method for hydrothermal decomposition of zircon and extraction of U and Pb for isotopic age determinations; Geochimica et Cosmochimica Acta, v. 37, p. 484–494.
1982: Improved accuracy of U-Pb ages by the creation of more concordant systems using an air abrasion technique; Geochimica et Cosmochimica Acta, v. 46, p. 637–649.

Parrish, R.R., Roddick, J.C., Loveridge, W.D., Sullivan, R.W.
1987: Uranium-lead analytical techniques at the geochronology laboratory, Geological Survey of Canada; *in* Radiogenic Age and Isotope Studies: Report 1; Geological Survey of Canada, Paper 87-2, p. 3–7.

Roddick, J.C., Loveridge, W.D., and Parrish, R.R.
1987: Precise U/Pb dating of zircon at the sub-nanogram Pb level; Chemical Geology, v. 66, p. 111–121.

– 2 –

Rapid extraction of Sr and Pb by ion-specific chromatography for thermal ionization mass spectrometry analysis

R.J. Thériault[1] and W.J. Davis[1]

Thériault, R.J. and Davis, W.J., 1999: Rapid extraction of Sr and Pb by ion-specific chromatography for thermal ionization mass spectrometry analysis; in *Radiogenic Age and Isotopic Studies: Report 12; Geological Survey of Canada, Current Research 1999-F, p. 9–12.*

Abstract: A laboratory procedure is described for the removal and purification of Sr and Pb using Sr-Resin™, for the purpose of thermal ionization mass spectrometry. Column preparation and elution can be accomplished within six hours, increasing efficiency in terms of time and reagent use relative to other established methods. The procedure is particularly useful for isotopic studies of organic-rich samples, as the extracted Sr and Pb yield quality analyses by thermal ionization mass spectrometry, with no evidence of elemental or organic interferences.

Résumé : On décrit une méthode de laboratoire permettant d'extraire et de purifier le Sr et le Pb à l'aide de Sr-Resin™, en vue de l'analyse par spectrométrie de masse à ionisation thermique. Comme la préparation de la colonne et l'élution peuvent être réalisées en moins de six heures, cette méthode est plus efficace en termes de temps et de réactifs utilisés en comparaison d'autres méthodes établies. Elle est particulièrement utile lors d'études isotopiques d'échantillons riches en matière organique, car le Sr et le Pb extraits permettent de réaliser des analyses de qualité par spectrométrie de masse à ionisation thermique, sans signe d'interférences causées par des espèces élémentaires ou des substances organiques.

---

[1] Geological Survey of Canada, 601 Booth Street, Ottawa, Ontario K1A 0E8

INTRODUCTION

The use of Sr-Resin™ (Eichrom Industries Inc., Darien, Illinois), a bis-t-butyl-cis-dicyclohehano-18-crown-6 ether, for selective sorption and removal of Sr and Pb was previously demonstrated (Horowitz et al., 1991, 1994). Its capability for selectively retaining Sr and Pb over a broad range of nitric acid concentrations allows for separation of these metallic elements from other matrix constituents in solution. This is of particular interest to workers seeking pure concentrates of Sr and Pb from geological, biological, and environmental samples for isotopic analysis by thermal ionization mass spectrometry (TIMS). The presence of interfering metallic or organic components in a metal concentrate may cause isobaric interferences, impede ionization, yield unstable signals, and result in strong mass fractionation and imprecise data during TIMS analysis. Given the wide range of bulk compositions of sample materials in geological, environmental, and biological studies, it is highly desirable to use a chromatographic medium that will strip metallic elements of interest from bulk matrix and other potentially interfering elements. The use of Sr-Resin™ offers several advantages over other established chromatography procedures. Strontium and lead can be stripped sequentially from one sample solution. Complete removal of Sr and Pb is easily achieved within six hours and multiple passes through chromatographic columns to purify Pb are not required, as they are in other methods currently in use (e.g. Manhes et al., 1984). This report describes a rapid procedure to extract Sr and Pb, free of constituent matrix interference during TIMS analysis, using Sr-Resin™ chromatographic columns.

CHEMICAL PROCEDURE

Column calibration and efficiency of extraction were determined using SRM 1400 bone ash, organic lake sediments, and carbonate rock, thus allowing for evaluation of laboratory procedures with respect to treatment of organic and mineral samples of interest in Sr and Pb isotopic investigations. All laboratory procedures were conducted under Class 100 clean air conditions. Pure reagents were prepared by subboiling double quartz and teflon™ two-bottle distillation (Mattinson, 1972; Parrish et al., 1987) at the Geochronology Laboratory of the Geological Survey of Canada, or purchased from Seastar Chemicals, Inc. of Sidney, British Columbia. Distilled water was obtained from a Milli-Q™ water purification system.

The columns are made from heat shrink PFTE Teflon™ and have a resin volume of 250 µL over a bed length of 30 mm. This bed yields a minimum working capacity of approximately 225 µg of Sr, based on specifications by Eichrom Industries Inc. of 10 to 20 per cent of the total column capacity of 8.9 mg Sr/mL of resin bed.

Extraction of Sr and Pb from 250 µL Sr-Resin™ columns

Calibration of the ion exchange columns for sequential extraction of Sr and Pb utilized SRM 1400 bovine bone ash reference material. National Institute of Standards in Technology (NIST) certified abundances for Sr and Pb are 249 ± 7 ppm and 9.07 ± 0.12 ppm respectively. Aliquots of approximately 0.1 g of SRM 1400 were weighed in 7 mL Savillex™ vials, dissolved in 3 mL 6.2 N HCl at room temperature, and dried and redissolved overnight in a mixture of 1 mL 12 N HCl and 1 mL 16 N HNO_3 on a hot plate at 100°C. Clear HCl–HNO_3 solutions were dried before being taken up in 1 ml 3.2 N HNO_3. Sr-Resin™ was cleaned by soaking in water and 6.2 N HCl for two hours each before being packed in the columns. Following conditioning of the columns, the 3.2 N HNO_3 solutions of SRM 1400 were loaded. In order to assess the removal of various analytes in different acidic media, 1 mL aliquots of H_2O and 6.2 N HCl were analyzed by inductively-coupled plasma mass spectrometry (ICP-MS). The resulting elution curve for Sr and Pb is displayed in Figure 1 and details of the procedure are outlined in Table 1.

The ICP-MS analyses demonstrated that most matrix elements, including Na, K, Rb, Mg, Ti, Ca, Fe, Zn, Y, and rare-earth elements, were stripped from the column with 5 mL (33 free column volumes) 3.2 N HNO_3. No measurable amounts of Sr and Pb were eluted with 3.2 N HNO_3. The 3.2 N HNO_3 rinse purged the column adequately of matrix constituents to allow for stripping of Sr in a narrow band of 3 mL H_2O. Minor amounts of Al and Ba were detected in the recovered Sr and as much as 8 per cent of the total Pb was removed from the column with H_2O. However, Pb is relatively immobile in weak acidic media and was purged from the column with 4 ml 6.2 N HCl. Trace quantities of Al, Cr, Sr, Se, and Bi were detected in the recovered Pb, whereas V and As yielded ICP-MS counts similar to those of Pb. A drop of 0.2 N H_3PO_4 was added to each Sr and Pb concentrate

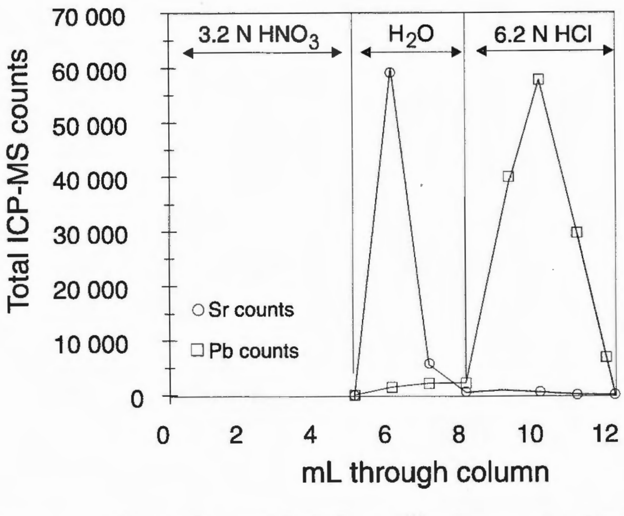

Figure 1. Elution for 250µL Sr-Resin™ columns with 3.2 N HNO_3, H_2O, and 6.2 N HCl, showing elution curves for Sr and Pb.

Table 1. Procedure for extracting Sr and Pb using 250 µL Sr-Resin™ columns.

Column preparation

Wash Sr-Resin™ with 6 N HCl, H_2O and 3 N HNO_3
Add 250 µL Sr-Resin ™ to columns
Wash twice with 3 mL 6N HCl, 3 mL H_2O
Equilibrate columns with 3 mL 3.2 N HNO_3

Sample loading, and Sr and Pb collection

Add sample as 1 mL 3.2 N HNO_3
Add 5 mL 3.2 N HNO_3
Insert Sr collection beakers
Collect Sr with 3 mL H_2O
Add 0.01 mL H_3PO_4 to Sr collection beakers
Insert Pb collection beakers
Collect Pb with 4 mL 6.2 n HCl
Add 0.01 mL HNO_3 to Pb collection beakers
Evaporate Sr and Pb concentrates to dryness

before evaporation to dryness. Three Sr chromatography procedure blanks were 39 pg, 42 pg, and 118 pg. Chromatography Pb blanks were 79 pg, 122 pg, 142 pg, and 183 pg. The entire column chemistry procedure, from packing the columns with Sr-Resin™ to final recovery of Pb, can be completed in six hours.

Column efficiency

A dolostone sample containing 349 ppm Sr was used for column efficiency tests. Aliquots of approximately 0.03 g of sample powder were weighed in 15 mL Savillex™ vials and dissolved in 3 mL 2.5 N HCl at room temperature. One aliquot was spiked with ^{84}Sr prior to column chemistry and two others were spiked after, thus allowing comparison of the amount of Sr added to the columns and the amount recovered. The two Sr concentrates spiked after recovery from the columns contained 82.9 per cent and 81.4 per cent respectively of the total Sr loaded on the columns.

Efficiency tests for Pb used an organic lake sediment sample containing 15 ppm Pb. Aliquots of approximately 0.004 g of lake sediment were weighed in 7 mL Savillex™ vials and dissolved by adding three times 1 mL 12 N HCl and 1 mL 16 M HNO_3 on a hot plate for two to three hours at approximately 100°C. Two aliquots of lake sediments were spiked with a ^{208}Pb tracer solution prior to loading on columns to determine the total amount of Pb loaded. Two additional aliquots were spiked with ^{208}Pb after Pb recovery to determine the total amount of Pb recovered from the columns. Efficiency tests for Pb recovery from two columns yielded similar recoveries of 68 per cent and 67.5 per cent of the total Pb load.

MASS SPECTROMETRY

Strontium and lead recovered from Sr-Resin™ columns were analyzed by thermal ionization on a MAT 261 solid-source mass spectrometer in static multicollector mode. Over 60 carbonate samples have been analyzed using this technique (M. Savard, unpubl. data, 1998). Strontium loads of 0.5 to 5 µg consistently yielded stable ^{88}Sr signals ranging from 2 to 4 V throughout analyses of 100 to150 eight-second scans. Mass fractionation, corrected to $^{88}Sr/^{86}Sr = 8.37521$, typically ranged from 0.3%/amu to 0.1%/amu over the course of an analysis. Evidence for Ca that typically impedes Sr ionization was not observed.

Lead loads of 50 ng to100 ng yielded ^{206}Pb signals of 2 to 4V over a temperature range of 1320 to 1450°C, throughout analyses of 60 eight-second scans. There was no evidence of the presence of interfering organic material, monitored at atomic mass 205 at filament temperatures of 1100–1200°C.

A significant problem for Pb analysis is the difficulty in removing Pb concentrates from collection beakers. The concentrates are in the form of an insoluble gel and are difficult to pipette from their collection beakers onto Re filaments, which results in loading less than the full amount of Pb recovered from the Sr-Resin™ columns and potentially higher Pb blanks. The addition of one drop of concentrated HNO_3 to the Pb concentrates prior to evaporation to dryness apparently reduced the viscosity of the dry concentrates, thus permitting easier loading on filaments for TIMS analysis. The cause of this problem remains unknown, but affects both Pb samples and blanks and thus seems to be related to the addition of 6.2 N HCl to Sr-Resin™ for the removal of Pb.

SUMMARY

Chromatographic separation and extraction of Sr and Pb using Sr-Resin™ offers several advantages over other, more established procedures involving cation or anion exchange chromatography. The entire column chemistry procedure can be completed within six hours, making it significantly less labour intensive than other procedures. Both Sr and Pb may be extracted sequentially from a sample in one procedural step. Ionization of Sr and Pb concentrates by TIMS yields stable signals that may be integrated over adequate time intervals for high-precision isotopic determinations. No evidence for interference from organic or inorganic sample matrix components was observed during TIMS analysis, making this chemical procedure applicable to the study of environmental and biological materials.

Certain aspects of the procedure remain problematic and require further investigation. The procedure yields moderate recoveries of approximately 80 per cent of total Sr and 70 per cent of total Pb. These recoveries may be of concern for low-concentration samples. Difficulties in loading the Pb concentrates on filaments for TIMS analysis can diminish the total amount of Pb available for analysis and may be related to elution of Sr-Resin™ with 6.2 N HCl used in Pb stripping.

Furthermore, Pb procedural blanks are variably elevated and further development of laboratory methods is required to assure consistently low Pb procedural blanks.

ACKNOWLEDGMENTS

Discussions with P. Outridge and his interest in developing methods for the isotopic analysis of environmental materials were primary motivations for this work. Kevin Telmer and Martine Savard are warmly thanked for supplying organic lake sediment and carbonate rock sample material. Jen Dougherty assisted with the initial column preparation and calibration of Sr and Pb elution. Vicki McNicoll is thanked for critically reading an earlier version of the manuscript.

REFERENCES

Horowitz, E.P., Dietz, M.L., and Fisher, D.E.
1991: Separation and preconcentration of strontium from biological and environmental samples by extraction chromatography using a crown ether; Analytical Chemistry, v. 63, p. 522.

Horowitz, E.P., Dietz, M.L., Rhoads, S., Felinto, C., Gale, N.H., and Houghtonn, J.
1994: A lead-selective extraction chromatographic resin and its application to the isolation of lead from geological samples; Analytica Chimica Acta, v. 292, p. 263–273.

Manhes, G., Allègre, C.J., and Provost, A.
1984: U-Th-Pb systematics of the eucrite 'Juvinas': precise age determination and evidence for exotic lead; Geochimica et Cosmochimica Acta, v. 48, p. 2247–2264.

Mattinson, J. M.
1972: Preparation of hydrofluoric, hydrochloric, and nitric acids at ultra-low lead levels; Analytical Chemistry, v. 44, p. 1715–1716.

Parrish, R.R., Roddick, J.C., Loveridge, W.A., and Sullivan, R.W.
1987: Uranium-lead analytical techniques at the geochronology laboratory, Geological Survey of Canada; *in* Radiogenic Age and Isotopic Studies: Report 1; Geological Survey of Canada, Paper 87-2, p. 3–7.

– 3 –

Characterization of the chemical composition and ^{40}Ar-^{39}Ar systematics of intralaboratory standard MAC-83 biotite

H.A. Sandeman[1,2], D.A. Archibald[2], J.W. Grant[2], M.E. Villeneuve[1],
and F.D. Ford[3,4]

Sandeman, H.A., Archibald, D.A., Grant, J.W., Villeneuve, M.E., and Ford, F.D., 1999: Characterization of the chemical composition and ^{40}Ar-^{39}Ar systematics of intralaboratory standard MAC-83 biotite; in *Radiogenic Age and Isotopic Studies: Report 12; Geological Survey of Canada, Current Research 1999-F, p.13–26.*

Abstract: The composition and Ar systematics of biotite (710–355 μm) from MAC-83, a glassy, rhyodacitic crystal-lapilli tuff, have been characterized by electron microprobe and laser ^{40}Ar-^{39}Ar analysis. Fifty electron microprobe analyses demonstrate that the biotites are homogeneous in composition. Twenty-six laser total-fusion, ^{40}Ar-^{39}Ar analyses of the biotite, calibrated against Taylor Creek Rhyolite sanidine (28.34 Ma) and Fish Canyon Tuff sanidine (28.02 Ma), yielded a weighted mean age (based on the respective errors) of 24.36 ± 0.17 Ma. Mass spectrometric determinations of Ca/K and Cl/K were reproducible yielding Cl/K = 0.050 ± 0.002, Ca/K = 0.025 ± 0.040 (errors at 2σ). Both conventional furnace and laser step-heating analysis of MAC-83 biotite reveals that it is characterized by minor excess argon, but that overall it yields a well-defined, internally concordant spectrum. These data indicate chemical homogeneity and 'regular', reproducible argon-release behaviour, implying suitability as a reference material for ^{40}Ar-^{39}Ar laser geochronology.

Résumé : Les analyses ^{40}Ar-^{39}Ar par microsonde électronique et par laser ont permis de déterminer avec précision la composition et la classification Ar de la biotite (710–355 μm) provenant d'un tuf à lapillis crystallin, rhyodacitique et vitreux (MAC-83). Les 50 analyses réalisées à la microsonde électronique montrent que la composition de la biotite est homogène. Les 26 analyses ^{40}Ar-^{39}Ar de la biotite, par fusion totale par laser, calibrées par rapport à la sanidine de la Rhyolite de Taylor Creek (28,34 Ma) et à la sanidine du Tuf de Fish Canyon (28,02 Ma), montrent un âge moyen pondéré (basé sur les erreurs respectives) de 24,36 ± 0.17 Ma. Les déterminations au spectromètre de masse de Ca/K et Cl/K étaient reproductibles et ont donné les valeurs suivantes : Cl/K = 0,050 ± 0,002, Ca/K = 0,025 ± 0,040 (erreurs à 2σ). Les analyses au four traditionnel et au laser par chauffage étagé de la biotite MAC-83 révèlent que cette dernière se caractérise par un léger excédent d'argon, mais qu'en général, elle montre un spectre interne concordant bien défini. Ces données indiquent que la composition chimique est homogène, que le comportement de libération de l'argon est reproductible et régulier et que l'on pourrait utiliser la biotite comme matériau de référence pour la géochronologie ^{40}Ar-^{39}Ar par laser.

---

[1] Geological Survey of Canada, 601 Booth Street, Ottawa, Ontario K1A 0E8
[2] Department of Geological Sciences, Queen's University, Kingston, Ontario K7L 3N6
[3] Ontario Ministry of Northern Development and Mines, Geoscience Laboratories, 933 Ramsey Lake Rd., Sudbury, Ontario P3E 6B5
[4] Current address: Inco Technical Services Ltd., 2060 Flavelle Boulevard, Mississauga, Ontario L5K 1Z9

INTRODUCTION

Volumetrically abundant ^{40}Ar-^{39}Ar geochronological standards that yield high quality, reproducible analytical results have proven difficult to obtain because of the inherent heterogeneity of many suitable mineral-dating standards and because many standards (e.g. Fish Canyon Tuff sanidine and biotite; Cebula et al., 1986) were not comprehensively documented in terms of their chemical homogeneity and ^{40}Ar-^{39}Ar release behavior prior to widespread use. This problem is exacerbated when these materials are used as low-mass laser ^{40}Ar-^{39}Ar geochronological standards, in particular if their homogeneity on <10 mg scale aliquots has not been demonstrated. Thus, historical reference materials such as LP-6 biotite (360–250 µm; Ingamells and Engels, 1976) and Mmhb-1 (Alexander et al., 1978) that were used for K-Ar and conventional ^{40}Ar-^{39}Ar step-heating analysis are now considered unsuitable reference materials for low-mass (≤5 mg) laser ^{40}Ar-^{39}Ar dating (Baksi et al., 1996).

Sample MAC-83, documented in Sandeman et al. (1997a), represents the basal exposure of an Oligocene pyroclastic sequence, the Cerro Huancahuancane Formation, exposed in the Cordillera de Carabaya of southeastern Peru (Fig. 1). The sample of rhyodacitic crystal-lapilli tuff (lat. 14°34′25"S, long. 69°50′25"W) is glassy and contains abundant subhedral to euhedral phenocrysts of plagioclase (20.63 volume %), biotite (12.76%), sanidine (7.82%) and quartz (7.67%) disposed in a vesicular, glass-rich matrix (43.74%) comprising variably flattened, phenocryst-poor, vesicular lapilli and ash. Microphenocrystic monazite, zircon, apatite, and ilmenite occur in the groundmass and as inclusions in all phenocryst phases. Lithic fragments constitute 7.38 volume % of the rock, but ubiquitously comprise mudstone (87%), fine-grained muscovite+biotite pelite (7%), and sandstone (6%). Figure 2 is a photomicrograph showing the fresh, glass-rich nature of MAC-83.

On the basis of its essentially internally concordant Ar-release pattern, its high $^{40}Ar^*$ content, its fresh character, as well as its high modal abundance, MAC-83 biotite (710–355 µm) has been used over the past few years by the ^{40}Ar-^{39}Ar geochronology laboratories at Queen's University and at the Geological Survey of Canada as an internal laboratory standard for conventional and laser analyses. The intent of this contribution is to present comprehensive electron microprobe analyses of MAC-83 biotite and the results of recent experiments wherein it was calibrated against international geochronological reference materials that are known to be homogeneous on a grain-to-grain scale and have been recommended as laser ^{40}Ar-^{39}Ar standards (Baksi et al., 1996; Renne et al., 1998). The results presented herein demonstrate that MAC-83 biotite is homogeneous in both major-element chemistry (K_2O in particular) and age with respect to low-mass (≤8 mg) aliquots and represents a well documented material suitable for use as an ^{40}Ar-^{39}Ar laser geochronological standard.

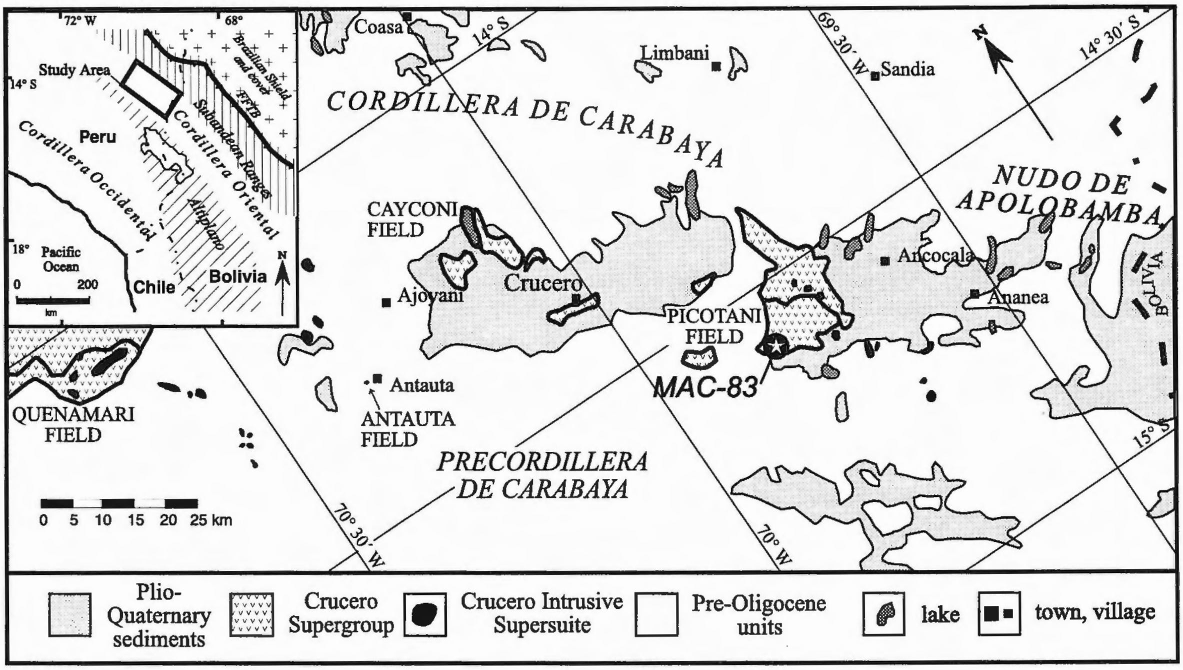

Figure 1. Map showing the location and geological setting of specimen MAC-83 in relationship to the major morphotectonic subdivisions of the Central Andes.

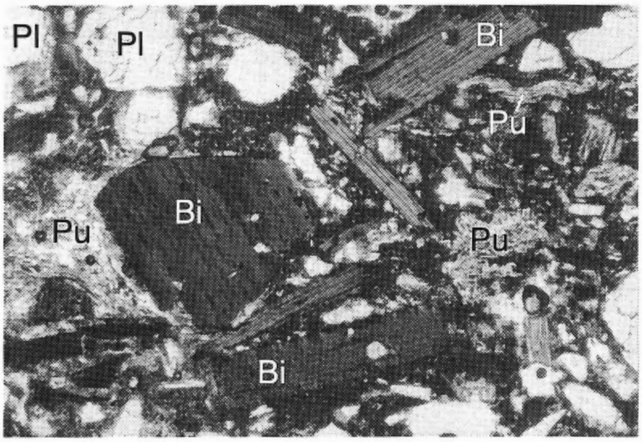

Figure 2. Photomicrograph (plane-polarized light) demonstrating the fresh character of sample MAC-83 with euhedral grains of biotite set in a vesicular, glass-rich matrix. The long dimension of the field of view is 3 mm. Bi = biotite; Pl = plagioclase; Pu = glassy pumice fragments.

ANALYTICAL METHODS

Mineral preparation

A ca. 4 kg specimen of fresh tuff was cleaned of all weathering surfaces and crushed to chips in a clean jaw crusher. Extraneous lithic fragments were removed by hand-picking prior to pulverization in a Braun rotary disc mill. The sample was sieved and the 1000–710, 710–355, and 355–250 µm fractions were extracted for further mineral separation. The respective grain size fractions were cleaned repeatedly in deionized water and dried at 50°C. The 710–355 µm fraction was processed through a Frantz^{TM} isodynamic magnetic separator operating at a current of 0.6 A, a side tilt of 15° and a back tilt of 12°. The biotite separate was gently rolled with a steel rolling pin to remove adhering matrix glass and then repeatedly ultrasonically washed in reagent-grade acetone. The biotite grains were separated from all remaining waste material using standard magnetic and heavy-liquid gravity separation techniques and hand picked under a binocular microscope to ensure high purity.

Electron microprobe analysis

Biotite compositions were determined at the Ontario Ministry of Northern Development and Mines (MNDM) Geoscience Laboratories using a JEOL 6400 scanning electron microscope equipped with an Oxford Instruments link analytical system. Operating conditions utilized a 20 KeV accelerating potential and a 2.5 nA current in the Faraday cage. Ten grains of the 710–355 µm fraction, mounted perpendicular to their c-axes in epoxy, were analyzed five times each in 'spot-mode' for a total of 50 analyses. These were supplemented with three analyses of MAC-83 biotite at the Electron Microprobe Laboratory at Queen's University, Kingston, Ontario. The analytical methods for these analyses are outlined in Sandeman et al. (1997b).

At the MNDM, single-element oxide standards were used for all elements except Mn and Ti ($MnTiO_3$), Ca (diopside), Na (beryllonite), K (microcline), and Cl (NaCl). To monitor precision, seven analyses of the United States National Museum reference material Kakanui Hornblende were obtained during the analytical runs. The per cent error in the analyses of the standard was significantly less than 5% for all elements except MnO, which yielded a ca. 15% error because of its very low concentration (near detection limit).

Irradiation

Aliquots comprising 18 to 24 grains of the biotite were wrapped in aluminum foil and sequentially stacked in two 11.5 cm long and 2.2 cm diameter aluminum irradiation cannisters. Geochronological reference materials or flux monitors included TCRsan (28.34 Ma; Renne et al., 1998) and FCTsan2 (28.02 Ma; Renne et al., 1998), both of which have been demonstrated to be sufficiently homogeneous for laser ^{40}Ar-^{39}Ar dating (Renne et al., 1994; Baksi et al., 1996; Renne et al., 1998). These were evenly spaced with the unknowns, to enable precise determination of the irradiation parameter 'J' throughout the cannister. The position of each of the foil packages relative to the base of the irradiation cannisters was carefully measured to determine the J-curve of the individual packages. The irradiation cannisters were sent to McMaster University Reactor, McMaster University, Hamilton, Ontario, and were irradiated with fast neutrons in position 5C for periods of 11.6 and 10 hours, respectively. The cannisters were centred in the region of highest flux in the reactor, ensuring a radiation dosage of ca. 4 x 10^{13} neutrons/cm^2/s. Subsequent to irradiation, the cannisters were allowed to cool radioactively for approximately 300 and 100 days, respectively, before analysis.

Mass spectrometry

The neutron flux monitors and aliquots of five to six grains (≤8 mg each) of MAC-83 biotite (for each irradiation cannister) were placed in 2 mm diameter pits drilled into an aluminum planchet sample holder. All unknowns and flux monitors were loaded into the planchet at the same time and were analyzed sequentially from top to bottom of the cannister. The holder was placed beneath the sapphire window of a stainless-steel chamber connected to an ultra-high-vacuum purification system. The extraction system was 'baked-out' for 15 hours at ca. 200°C to reduce the system argon blank. During analysis at Queen's University, samples were uniformly heated with a defocused 8 W Lexel 3500 continuous argon-ion laser. Complete fusion of each aliquot was achieved at ca. 6 W laser power and all glass beads were heated until complete volatilization was confirmed visually. The evolved gas was purified with an air-cooled SAES getter and admitted to an online MAP 216 mass spectrometer having a Bäur Signer source and an electron multiplier (total gain = 5 x 10^{12}). Reproducible extraction system blanks, made routinely at the start and completion of each analytical day, were subtracted from the sample gas fractions. Each analysis involved nine sets of measurements starting with the high-mass ^{40}Ar baseline position and alternating peak and baseline measurements to the low-mass ^{36}Ar baseline position. Both peak and baseline measurements consisted of ten 100 ms readings that were compared to identify and reject statistical outliers. The baseline readings for each measurement were averaged. Each individual reading on a peak was baseline corrected by interpolating the two nearest baseline measurements on both the high- and low-mass positions of the peak to the time of the reading. The high- and low-mass corrections were then interpolated by inverse mass and the result subtracted from the reading.

The baseline-corrected peak measurements were regressed to zero-time, following the method of Press et al. (1989, p. 558–565), and corrected for extraction system and mass spectrometer blank, atmospheric contamination, radioactive decay of ^{37}Ar and ^{39}Ar, and interference reactions from K, Ca, and Cl (isotope production ratios were $[^{40}Ar/^{39}Ar]_K = 3.02 \times 10^{-2}$, $[^{36}Ar/^{37}Ar]_{Ca} = 2.79 \times 10^{-4}$, and $[^{39}Ar/^{37}Ar]_{Ca} = 7.06 \times 10^{-4}$; Deckart, 1996). Correction for ^{36}Ar from chlorine was made following the method suggested by Roddick (1983). Dates and errors were calculated using the formulae given by Dalrymple et al. (1981) and constants recommended by Steiger and Jäger (1977). Errors shown for the ^{40}Ar-^{39}Ar ages represent the analytical precision at 2σ, including the error in the J-value, but excluding that of the age of the monitor.

RESULTS

Averaged electron microprobe data are presented in Table 1 and ^{40}Ar-^{39}Ar analytical data for the step-heating analyses of MAC-83 biotite are presented in Tables 2 and 3. The analytical data for the standards (TCRsan and FCTsan2) and the aliquots of MAC-83 biotite are presented in Tables 4 (cannister 1) and 5 (cannister 2). Standard TCRsan was used for both irradiation cannisters, applying an age of 28.34 Ma (Renne et al., 1998); calibration curves for the J-values versus position above base of can were fitted through interpolation using a third-order polynomial curve. J-curves for both cannisters are presented graphically in Figure 3. TCRsan was supplemented by four analyses of FCTsan2 in the second cannister. Although the age of FCTsan is a topic of significant debate (cf. Renne et al., 1994, and Lanphere and Baadsgaard, 1997), we used an age of 28.02 Ma (Renne et al., 1998). The addition of four analyses of this standard to the J-curve improves the Chi-squared value of the polynomial fit of the curve. These two standards were chosen because of their availability and because they have recently been demonstrated to be suitable laser ^{40}Ar-^{39}Ar geochronological standards (Baksi et al.,

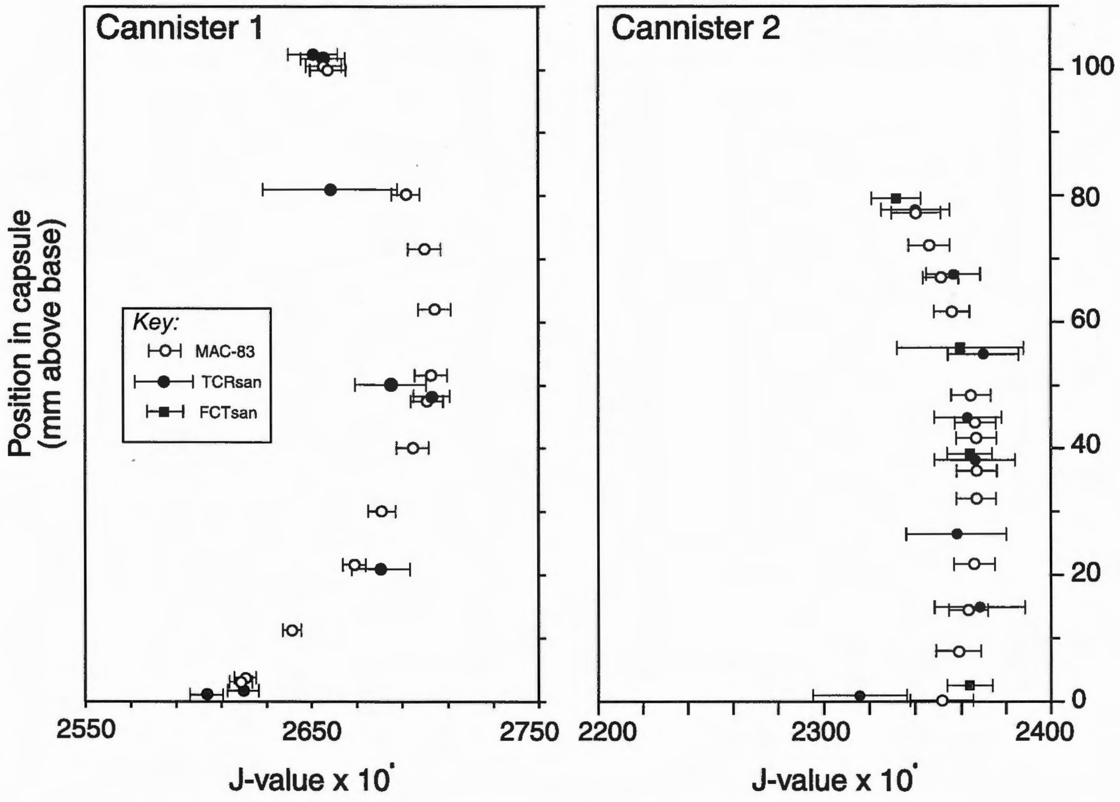

Figure 3. Diagram showing the J-value (with error) versus position for the monitors and aliquots of MAC-83 biotite in A) irradiation cannister 1 and B) irradiation cannister 2.

Table 1. Averaged (five analyses per grain) electron microprobe analyses of ten grains of the 710–355 µm size fraction of MAC-83 biotite and the average of three energy-dispersive electron microprobe analyses of the biotite obtained at Queen's University, Kingston, Ontario (fluorine was determined through wavelength dispersive analysis).

Element	grain 1 n=5	grain 2 n=5	grain 3 n=5	grain 4 n=5	grain 5 n=5	grain 6 n=5	grain 7 n=5	grain 8 n=5	grain 9 n=5	grain 10 n=5	Mean n=50	Std. Dev. 2σ	thin section n=3
SiO_2	35.84	35.05	35.80	35.76	35.76	35.62	35.55	35.70	35.27	35.38	35.58	0.64	35.59
TiO_2	4.29	5.14	4.03	4.05	4.10	4.13	4.03	4.05	4.06	4.14	4.19	0.65	4.03
Al_2O_3	15.54	15.44	15.66	15.62	15.43	15.95	16.05	15.73	15.99	16.09	15.77	0.59	14.96
Cr_2O_3	0.07	0.04	0.05	0.03	0.04	0.05	0.05	0.06	0.08	0.03	0.05	0.06	0.05
FeO	20.20	20.41	20.11	20.16	20.14	19.85	20.17	20.08	20.44	20.49	20.20	0.44	20.86
MnO	0.26	0.20	0.24	0.22	0.24	0.23	0.26	0.21	0.19	0.24	0.23	0.08	0.12
MgO	10.25	9.75	10.61	10.47	10.54	10.49	10.41	10.61	10.17	10.17	10.34	0.58	10.52
CaO	0.02	0.00	0.00	0.03	0.01	0.01	0.02	0.00	0.01	0.00	0.01	0.04	0.04
Na_2O	0.42	0.45	0.48	0.41	0.48	0.43	0.54	0.43	0.35	0.48	0.44	0.28	0.49
K_2O	9.27	8.99	9.39	9.35	9.25	9.26	9.43	9.34	9.39	9.51	9.32	0.30	9.04
BaO	0.51	1.32	0.07	0.33	0.48	0.25	0.17	0.32	0.11	0.05	0.34	0.74	nd
Cl	0.27	0.21	0.27	0.26	0.26	0.24	0.26	0.25	0.24	0.24	0.25	0.05	0.21
F	nd	nd	nd	nd	nd	nd	nd	nd	nd	nd	nd		1.14
O=Cl,F	0.06	0.05	0.06	0.06	0.06	0.06	0.06	0.06	0.05	0.05	0.05		0.56
Total	96.87	96.95	96.65	96.63	96.66	96.46	96.89	96.73	96.25	96.77	96.68		96.49
Cation proportions on the basis of 11 oxygens													
Si	2.722	2.681	2.716	2.719	2.721	2.706	2.696	2.711	2.694	2.689	2.706	0.034	2.938
Al^{vi}	1.278	1.319	1.284	1.281	1.279	1.294	1.304	1.289	1.306	1.311	1.294	0.034	1.062
Al^{iv}	0.112	0.073	0.117	0.120	0.105	0.135	0.131	0.118	0.133	0.130	0.119	0.042	0.394
Cr	0.004	0.003	0.003	0.002	0.002	0.003	0.003	0.004	0.005	0.002	0.003	0.004	0.003
Ti	0.245	0.295	0.230	0.232	0.234	0.236	0.230	0.231	0.233	0.237	0.240	0.038	0.250
Fe	1.283	1.305	1.276	1.282	1.282	1.261	1.279	1.275	1.305	1.302	1.285	0.032	1.440
Mn	0.017	0.013	0.016	0.014	0.016	0.015	0.016	0.013	0.012	0.015	0.015	0.005	0.019
Mg	1.161	1.111	1.200	1.187	1.196	1.188	1.176	1.201	1.158	1.153	1.172	0.060	1.294
Ca	0.002	0.000	0.000	0.002	0.001	0.001	0.002	0.000	0.001	0.000	0.001	0.003	0.004
Na	0.061	0.067	0.070	0.060	0.071	0.063	0.080	0.063	0.052	0.070	0.065	0.041	0.078
K	0.898	0.878	0.909	0.907	0.898	0.898	0.912	0.904	0.915	0.922	0.905	0.027	0.952
Ba	0.015	0.039	0.002	0.010	0.014	0.007	0.005	0.010	0.003	0.002	0.010	0.022	0.000
Cl	0.035	0.027	0.035	0.034	0.033	0.031	0.034	0.033	0.031	0.031	0.032	0.006	0.029
F													0.298
F/F+M	0.5249	0.5402	0.5154	0.5193	0.5174	0.5150	0.5209	0.5150	0.5298	0.5305	0.5230		0.5267
Ca/K	0.0019	0.0000	0.0000	0.0028	0.0009	0.0009	0.0018	0.0000	0.0009	0.0000	0.0009		0.0038
Cl/K	0.0351	0.0281	0.0346	0.0335	0.0339	0.0312	0.0332	0.0322	0.0308	0.0304	0.0323		0.0280

All grains mounted perpendicular to their c-axis.
F/F+M = Fe/Fe+Mg; nd = not determined.

1993; Dalrymple et al., 1993; Baksi et al., 1996; Renne et al., 1998). All statistical treatment of the data uses the equations and methods of Bevington (1969).

Electron microprobe analyses

Electron microprobe analyses of MAC-83 biotite reveal that it is homogeneous in major-element composition and yields reproducible results for ten different crystals oriented perpendicular to their c-axes on a grain mount. The biotite is characterized by approximately equal concentrations of iron and magnesium (Fe/Fe+Mg = 0.515-0.540), high Al_2O_3 (15.43–16.05 wt. %), and high TiO_2 (4.03–5.14 wt. %). Figure 4 presents a backscatter electron image of MAC-83 biotite demonstrating that it is homogeneous in composition and exhibits no low or high atomic number (Z) intergrowths. Furthermore, an X-ray diffraction analysis of powdered 250–350 µm biotite reveals no chlorite in the biotite structure.

The most common inclusion phase is apatite, although zircon and monazite occur rarely. The biotite has reproducible and consistent high potassium contents, averaging 9.32 ± 0.30 wt. % K_2O (n = 50), implying that it is not discernibly altered. It has appreciable quantities of halogens (ca. 1.14 wt % F and 0.25 ± 0.05 wt. % Cl). Chlorine in particular is very important because of interfering nuclear reactions during irradiation. Figures 5A and 5B are major- and trace-element plots of K_2O versus Fe/Fe+Mg and Cl versus K_2O for averaged analyses of MAC-83 biotite. They demonstrate the chemical homogeneity of the micas. In particular, Figure 5B emphasizes the homogeneity with respect to two elements, Cl and K_2O, that are of critical importance in ^{40}Ar-^{39}Ar mass spectrometry. Electron microprobe Cl/K ratios range from 0.00280 to 0.00351, whereas Ca/K ratios range from 0.0000 to 0.0038 (Table 1). The values for CaO should be treated with caution as calcium is near its detection limit as a major-element oxide.

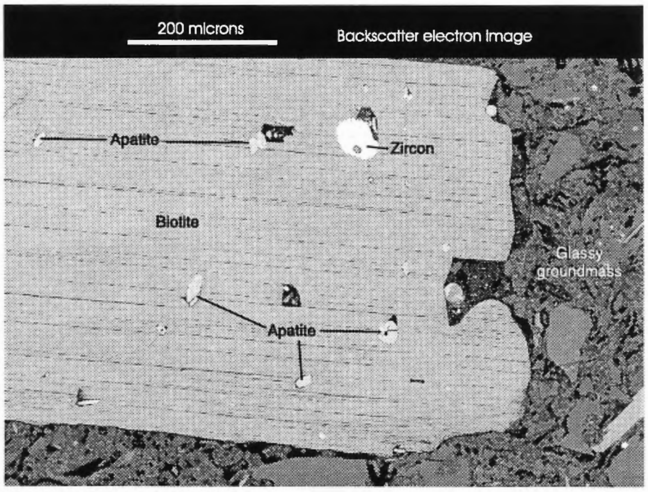

Figure 4. *Backscatter electron image of a biotite grain visually demonstrating its homogeneity. The grain shows an constant grey-scale intensity, implying backscatter of electrons from a crystal lattice having a constant bulk atomic number. Note the abundant apatite inclusions (confirmed through qualitative electron microprobe analysis) dispersed throughout the grain and the one zircon inclusion. Apatite grains are, however, typically heterogeneously distributed in the biotite grains.*

Step-heating analyses of MAC-83 biotite

The original, conventional ^{40}Ar-^{39}Ar step-heating analysis of the biotite (412 mg, Sandeman et al. [1997a], Queen's University) was calibrated against international reference

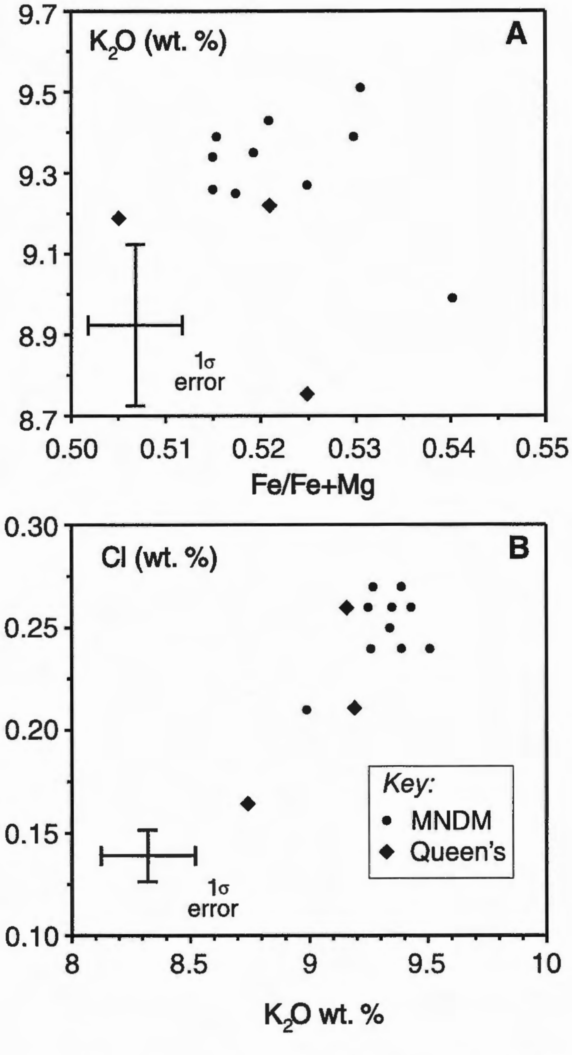

Figure 5. *Geochemical plots for the ten averaged electron microprobe analyses of MAC-83 biotite obtained at the Ministry of Northern Development and Mines (MNDM) (filled circles) and three analyses obtained using the energy-dispersive electron microprobe at Queen's University, Kingston, Ontario (diamonds).* ***A)*** *Plot of K_2O versus FeO/FeO+MgO and* ***B)*** *plot of Cl versus K_2O, demonstrating the compositional homogeneity of MAC-83 biotite in terms of these important elements. Error bars represent 2σ errors in the mean of the analytical measurements.*

material LP-6 biotite (360–250 µm, 128.5 Ma, Roddick [1983]) and yielded a concordant spectrum (Table 2; Fig. 6A) with a ten-step total-gas integrated age of 24.56 ± 0.22 Ma and a four-step plateau age of 24.27 ± 0.18 Ma representing 72.9% of the ^{39}Ar released (all errors herein quoted at 2σ). The argon released from the specimen comprised ca. 90% radiogenic argon and was characterized by low Ca/K ratios (ca. 0.03). An inverse isotope correlation plot, linking radiogenic with atmospheric argon, for the same four gas fractions (Fig. 6B) yielded a correlation age of 24.38 ± 0.13 Ma (mean square of weighted deviates [M.S.W.D.] = 1.55; initial ^{40}Ar/^{36}Ar = 269.7 ± 28.0). A subsequent seven-step laser analysis on two biotite grains of the 1000–710 µm grain-size fraction calibrated against ten aliquots of 710–355 µm MAC-83 (using a monitor age of 24.2 Ma) yielded a comparable spectrum characterized by excess argon in the low-power gas-release fractions, but a plateau for gas-release at higher laser powers (Fig. 7A). The sample yielded a total-gas, integrated age of 24.24 ± 0.25 Ma, identical to a three-step plateau that represented 92.7% of the total ^{39}Ar released. An inverse isotope correlation plot for the same three gas fractions (Fig. 7B) yielded an age of 23.94 ± 0.22 Ma (M.S.W.D. = 0.65; initial ^{40}Ar/^{36}Ar = 314.0 ± 30.5). The biotite yields reproducible (overlapping in error) results for both of these analyses; however, the argon isotope correlation analysis reveals minor excess argon in the low-temperature and low-power gas-release fractions. Nevertheless, the mica exhibits similar argon release patterns for both conventional step-heating and laser step-heating analyses. Complete data sets for these analyses are given in Table 2 for the conventional analyses and in Table 3 for the laser analyses.

^{40}Ar-^{39}Ar analyses cannister 1

The results from eight analyses of TCRsan and thirteen laser total-fusion analyses of aliquots of MAC-83 biotite are presented in Table 4. The analyses of TCRsan yielded reproducible ^{40}Ar*/^{39}Ar$_K$ values having a weighted mean (based on the errors) of 5.978 ± 0.083. The sanidine gave low Cl/K values (≤0.0001), indicating low Cl contents. Ca/K values ranged from 0.001 to 0.074, implying minor gas contribution from either a contaminating phase or minor Ca from the sanidine itself. The %^{40}Ar$_{ATM}$ ranged from a high of 18.15% to 0.20%, implying that the majority of the contained ^{40}Ar was radiogenic in origin.

For the aliquots of MAC-83 biotite, calculated Ca/K and Cl/K values (using isotope nuclear production factors for McMaster Reactor given in Table 4; Deckart, 1996) and the ^{38}Ar/^{39}Ar and ^{37}Ar/^{39}Ar ratios determined through mass spectrometry are highly reproducible, yielding values of 0.015 ± 0.018 and 0.050 ± 0.002, respectively. The amount of atmospheric contamination, as measured through the %^{40}Ar$_{ATM}$, was somewhat variable, ranging from 30.33% to 6.13%; however, the mean value of 9.17% was much more typical (*see* Table 4). The 13 analyses yielded an arithmetic mean total fusion age of 24.39 ± 0.16 Ma. Application of statistical analysis to these data produced a weighted mean age based on the volume of ^{39}Ar released from each aliquot of 24.34 ± 0.17 Ma and a weighted mean age based on the error in the calculated ages of 24.36 ± 0.17 Ma. Perhaps what is most remarkable is the reproducibility of the ^{40}Ar*/^{39}Ar$_K$ values, which for the aliquots of MAC-83 yielded a weighted mean of 5.093 ± 0.046, the 2σ uncertainty representing only a 0.91% error in the total.

Table 2. ^{40}Ar-^{39}Ar geochronological data for a conventional furnace step-heating analysis of a 412 mg aliquot of the 710–355 µm MAC-83 biotite, obtained at the Queen's University ^{40}Ar-^{39}Ar Geochronology Laboratory.

Conventional step-heating MAC-83 (710–355 µm): J = 0.003026 ± 0.000020							
Temp (°C)	**(^{40}Ar/^{39}Ar)**	**(^{36}Ar/^{39}Ar)**	**(^{37}Ar/^{39}Ar)**	**Vol^{39}Ar (x 10^{-8} cm^3)**	**f^{39}Ar**	**%^{40}Ar (Rad.)**	**Age (Ma) ± error (2σ)**
500	19.373	0.033	0.113	0.3757	0.006	49.20	51.36 ± 7.09
600	15.548	0.037	0.026	0.7213	0.011	29.05	24.50 ± 1.37
720	5.314	0.003	0.004	9.4194	0.147	85.34	24.59 ± 0.12
820	4.972	0.001	0.010	3.2464	0.051	91.89	24.77 ± 0.55
870	5.077	0.001	0.015	1.6961	0.027	91.08	25.08 ± 0.75
910	5.100	0.002	0.018	1.8950	0.030	89.56	24.77 ± 0.70
*965	4.888	0.001	0.012	4.3624	0.068	91.96	24.38 ± 0.19
*1010	4.738	0.001	0.006	11.7482	0.183	94.71	24.34 ± 0.16
*1060	4.680	0.001	0.007	24.0600	0.376	95.62	24.27 ± 0.10
*1200	5.179	0.002	0.135	6.5467	0.102	85.63	24.11 ± 0.17

Blank and decay-corrected isotope ratios
Integrated age = 24.54 ± 0.19 Ma
Plateau segment age (steps marked by asterisks) = 24.27 ± 0.18 Ma
Correlation age (steps marked by asterisks) = 24.38 ± 0.13 Ma; M.S.W.D. = 1.55; initial ^{40}Ar/^{36}Ar = 269.7 ± 28.0
Mass = 412 mg.

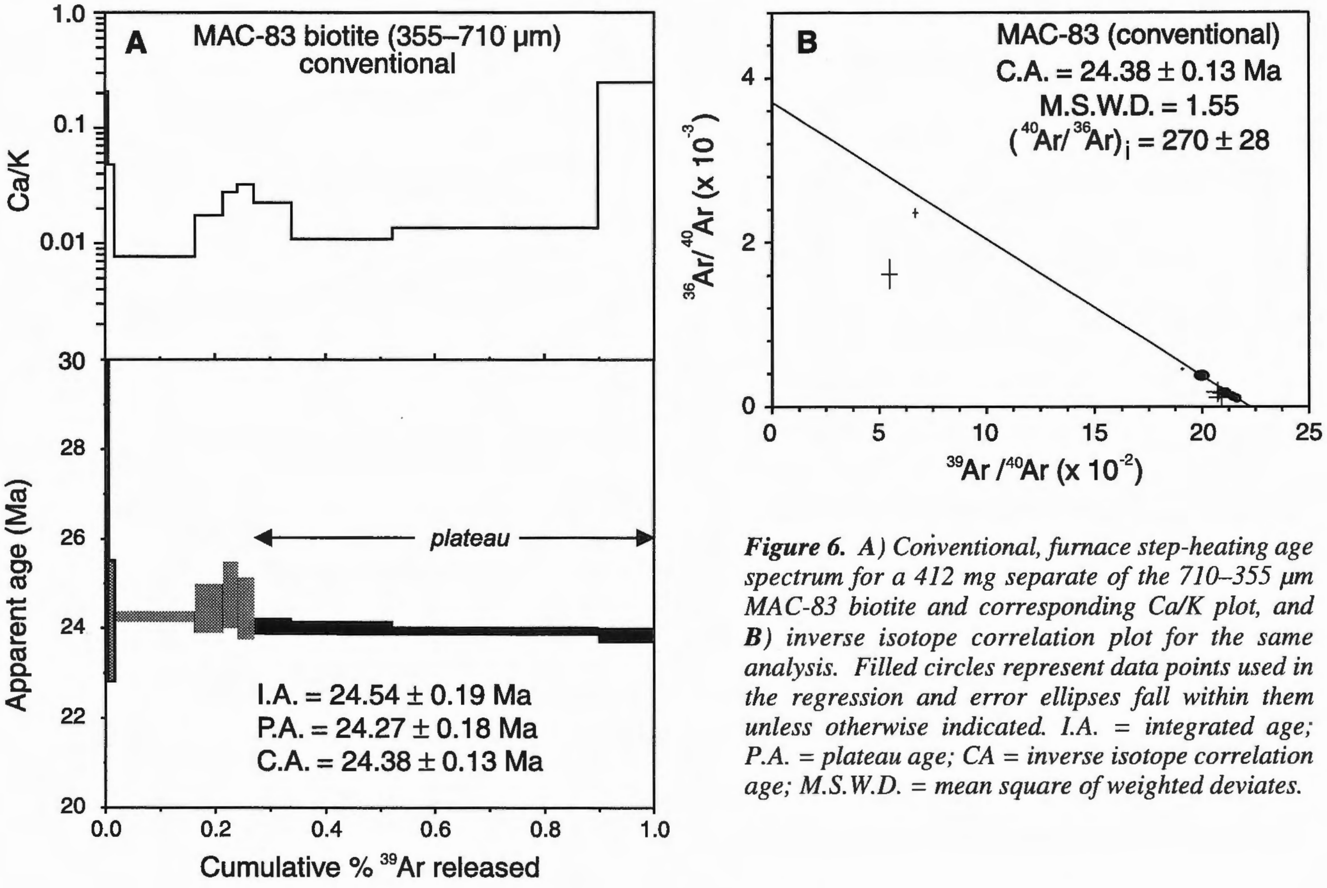

*Figure 6. A) Conventional, furnace step-heating age spectrum for a 412 mg separate of the 710–355 µm MAC-83 biotite and corresponding Ca/K plot, and **B**) inverse isotope correlation plot for the same analysis. Filled circles represent data points used in the regression and error ellipses fall within them unless otherwise indicated. I.A. = integrated age; P.A. = plateau age; CA = inverse isotope correlation age; M.S.W.D. = mean square of weighted deviates.*

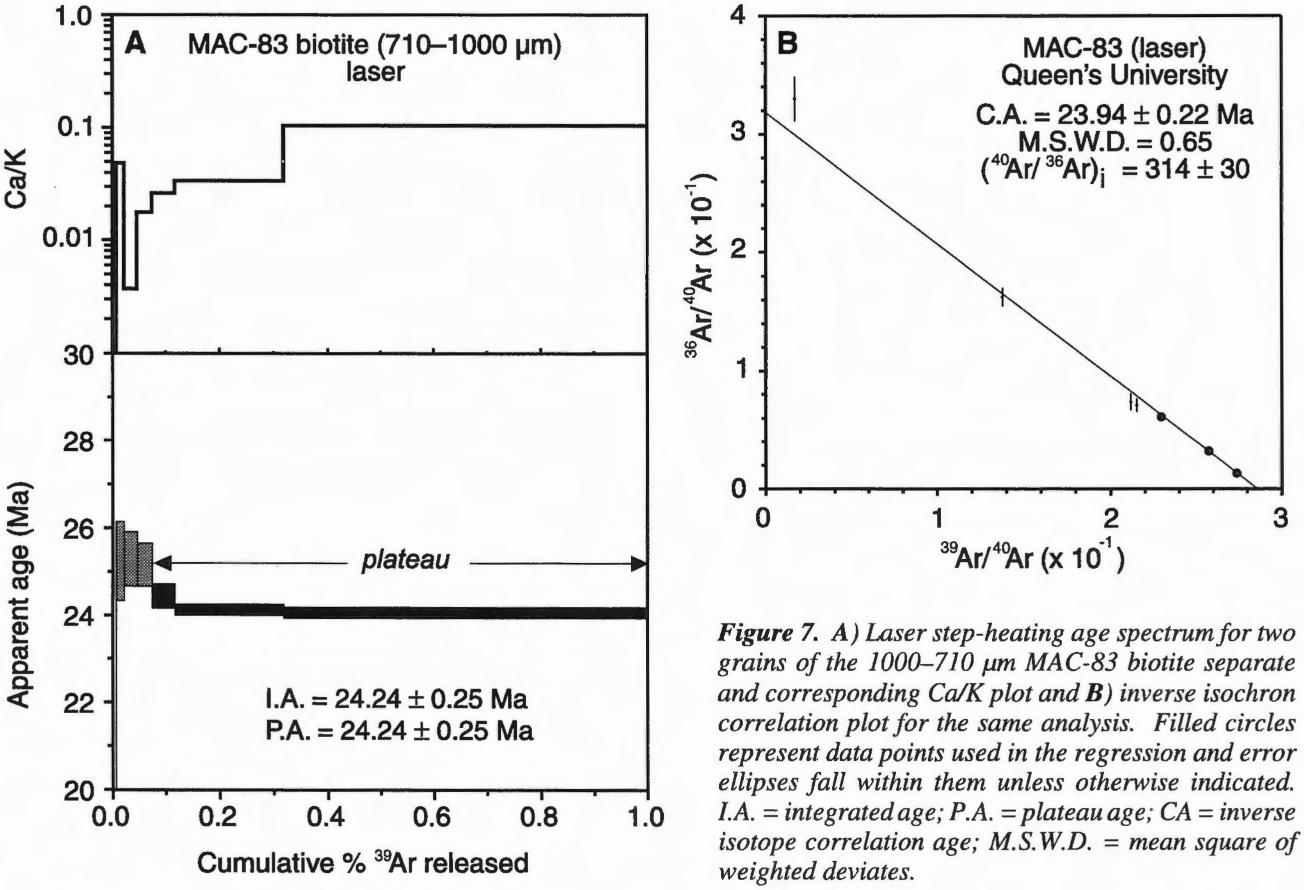

*Figure 7. A) Laser step-heating age spectrum for two grains of the 1000–710 µm MAC-83 biotite separate and corresponding Ca/K plot and **B**) inverse isochron correlation plot for the same analysis. Filled circles represent data points used in the regression and error ellipses fall within them unless otherwise indicated. I.A. = integrated age; P.A. = plateau age; CA = inverse isotope correlation age; M.S.W.D. = mean square of weighted deviates.*

Table 3. ^{40}Ar-^{39}Ar geochronological data for a laser step-heating analysis of two grains of the 1000–710 µm MAC-83 biotite separate obtained at the Queen's University ^{40}Ar-^{39}Ar Geochronology Laboratory.

Laser analysis MAC-83 (1000–710 µm): J = 0.003820 ± 0.000018

Power (W)	Volume ^{39}Ar (x 10^{-10} cm³)	^{40}Ar/^{39}Ar	^{38}Ar/^{39}Ar	Isotope ratios		Ca/K	Cl/K	%^{40}Ar ATM	f ^{39}Ar	^{40}Ar*/^{39}Ar$_K$	Age (Ma) ± 2σ
				^{37}Ar/^{39}Ar	^{36}Ar/^{39}Ar						
1.0	1.616 ± 0.008	58.5683 ± 0.0000	0.2077 ± 0.0110	0.0022 ± 1.4902	0.2026 ± 0.0084	0.000	0.036	97.36	0.66	1.530 ± 0.996	10.52 ± 6.82
1.5	3.638 ± 0.015	7.2638 ± 0.0021	0.2396 ± 0.0058	0.0014 ± 0.6638	0.0132 ± 0.0172	0.049	0.051	47.38	1.50	3.806 ± 0.136	26.04 ± 0.93
2.0	5.801 ± 0.023	4.7376 ± 0.0020	0.2350 ± 0.0050	0.0007 ± 0.7230	0.0043 ± 0.0368	0.004	0.050	21.06	2.39	3.722 ± 0.095	25.47 ± 0.65
2.5	6.797 ± 0.027	4.6600 ± 0.0020	0.2309 ± 0.0049	0.0007 ± 0.5684	0.0040 ± 0.0307	0.018	0.049	20.23	2.80	3.702 ± 0.075	25.33 ± 0.51
* 3.0	10.287 ± 0.041	4.3602 ± 0.0020	0.2309 ± 0.0046	0.0006 ± 0.5349	0.0031 ± 0.0209	0.026	0.049	17.30	4.23	3.594 ± 0.042	24.60 ± 0.28
* 4.0	48.648 ± 0.192	3.8852 ± 0.0020	0.2304 ± 0.0044	0.0003 ± 0.1365	0.0014 ± 0.0141	0.034	0.049	8.61	20.03	3.546 ± 0.019	24.28 ± 0.13
* 6.0	166.127 ± 0.655	3.6511 ± 0.0020	0.2401 ± 0.0044	0.0006 ± 0.0275	0.0005 ± 0.0393	0.105	0.051	3.06	68.39	3.537 ± 0.019	24.21 ± 0.13

Blank and decay-corrected isotope ratios
Integrated age = 24.24 ± 0.25 Ma
Plateau segment age (steps marked by asterisks) = 24.24 ± 0.25 Ma
Correlation age (steps marked by asterisks) = 23.94 ± 0.22 Ma; M.S.W.D. = 0.65; initial ^{40}Ar/^{36}Ar = 314.0 ± 30.5
f^{39}Ar = fraction of the total ^{39}Ar released
ATM = atmospheric component
^{40}Ar* = radiogenic argon component
^{39}Ar$_K$ = ^{39}Ar derived from ^{39}K during irradiation

^{40}Ar-^{39}Ar analyses cannister 2

The results from eight analyses of TCRsan and four of FCTsan2 along with thirteen laser total-fusion analyses of MAC-83 biotite are presented in Table 5. The analyses of TCRsan yielded reproducible ^{40}Ar*/^{39}Ar$_K$ values having a weighted mean (based on the errors) of 6.719 ± 0.041. The sanidine gave low Cl/K values (≤0.000), indicating low Cl contents. Values of Ca/K ranged from 0.035 to 0.042, implying minor gas contribution from either a contaminating phase or minor Ca from the sanidine itself. The %^{40}Ar$_{ATM}$ ranged from a high of 4.67% to 0.00%, implying that the majority of the contained ^{40}Ar was radiogenic in origin. The four analyses of FCTsan2 also yielded reproducible ^{40}Ar*/^{39}Ar$_K$ values having a weighted mean (based on the errors) of 6.676 ± 0.038. They gave low Cl/K values (≤0.000), Ca/K ranging from 0.010 to 0.052, and %^{40}Ar$_{ATM}$ values of 0.81% to 6.69%.

For MAC-83, the ^{38}Ar/^{39}Ar and ^{37}Ar/^{39}Ar and calculated Ca/K and Cl/K ratios determined through mass spectrometry are highly reproducible, yielding values of 0.035 ± 0.017 and 0.050 ± 0.001, respectively. The amount of atmospheric contamination, as measured through the %^{40}Ar$_{ATM}$, was somewhat variable, ranging from 4% to 12%; however, a mean value of 7.70% was much more typical (*see* Table 5). The 13 total-fusion analyses yielded an arithmetic mean age of 24.55 ± 0.52 Ma, a weighted mean age based on the volume of ^{39}Ar released from each aliquot of 24.50 ± 0.19 Ma, and a weighted mean age based on the error in the calculated ages of 24.44 ± 0.17 Ma. The reproducibility of the ^{40}Ar$_*$/^{39}Ar$_K$ values obtained for the aliquots of MAC-83 yielded were remarkable and yielded a weighted mean of 5.779 ± 0.045, the 2σ uncertainty representing only a 0.78% error in the total.

Analyses obtained at the ^{40}Ar-^{39}Ar laboratory at the Geological Survey of Canada

Aliquots of the 1000–710 µm fraction of MAC-83 biotite were analyzed by CO$_2$ laser ^{40}Ar-^{39}Ar methods at the Geological Survey of Canada Geochronology Laboratory. Samples were wrapped in cylindrical aluminum foil packets approximately 3 mm diameter and 4 to 7 mm long and arranged radially about a 40 mm by 19 mm aluminum can. Evenly interspersed with the samples were flux-monitor packets containing Fish Canyon Tuff sanidine with an assumed apparent age of 28.02 Ma (Renne et al., 1998). The can was sent to McMaster University Nuclear Reactor for an eight-hour irradiation in an approximate fast-neutron fluence of 3 x 10^{16} neutrons/cm². A more detailed explanation of procedures and methods is outlined in Villeneuve and MacIntyre (1997). Interpolation of J-factor between monitors yielded a J-value of 0.0018413 ± 0.5% (1s) for this analysis of MAC-83. The analytical data for these analyses are presented in Table 6.

Each of three single-grain aliquots was subjected to heating steps at two power settings of the laser, mimicking heating at medium and high temperature in a vacuum furnace, in

Table 4. ^{40}Ar-^{39}Ar laser total-fusion geochronological data for irradiation cannister 1, including eight monitors (TCRsan) and thirteen aliquots of the 710–355 µm size fraction of MAC-83 biotite. All errors are quoted at 2s level.

Position in can	J-value (x 10^6)	vol^{39}Ar (x 10^{-10} cm^3)	^{40}Ar/^{39}Ar	Isotope ratios[a]		^{36}Ar/^{39}Ar	Ca/K	Cl/K	%^{40}Ar$_{Atm}$	^{40}Ar*/^{39}Ar$_K$	Age (Ma)
				^{38}Ar/^{39}Ar	^{37}Ar/^{39}Ar						
TCR-san (28.34 Ma[b])											
11.0[c]	2604 ± 8	29.449 ± 0.116	7.4125 ± 0.0000	0.0132 ± 0.0099	0.0002 ± 0.4011	0.0048 ± 0.0085	0.074	0.000	18.15	6.080 ± 0.035	28.34
17.0	2620 ± 7	25.026 ± 0.099	6.1104 ± 0.0020	0.0125 ± 0.0122	0.0002 ± 0.4819	0.0004 ± 0.0918	0.051	0.000	1.28	6.044 ± 0.032	28.34
20.8	2681 ± 13	20.088 ± 0.079	5.9280 ± 0.0020	0.0125 ± 0.0148	0.0002 ± 0.8062	0.0002 ± 0.3670	0.036	0.000	0.56	5.905 ± 0.057	28.34
48.1	2703 ± 8	28.089 ± 0.111	5.9075 ± 0.0020	0.0127 ± 0.0107	0.0001 ± 0.2303	0.0003 ± 0.1458	0.001	0.000	1.02	5.858 ± 0.035	28.34
50.0	2686 ± 16	17.803 ± 0.070	5.9417 ± 0.0020	0.0126 ± 0.0165	0.0002 ± 1.2908	0.0003 ± 0.3391	0.023	0.000	0.95	5.894 ± 0.071	28.34
80.8	2659 ± 31	15.372 ± 0.061	5.9559 ± 0.0020	0.0127 ± 0.0183	0.0003 ± 0.9191	0.0002 ± 1.1928	0.047	0.000	0.20	5.954 ± 0.139	28.34
101.7	2656 ± 10	27.181 ± 0.107	5.9890 ± 0.0020	0.0127 ± 0.0111	0.0001 ± 0.8693	0.0002 ± 0.2957	0.015	0.000	0.66	5.961 ± 0.046	28.34
102.3	2652 ± 11	16.875 ± 0.067	5.9808 ± 0.0020	0.0127 ± 0.0169	0.0002 ± 0.6506	0.0002 ± 0.3637	0.027	0.000	0.32	5.971 ± 0.050	28.34
							0.034[d]	0.000[d]	2.89[d]	5.978 ± 0.083[e]	
MAC-83 bio (24.36 Ma)[f]											
2.90	2619 ± 5	12.894 ± 0.051	5.5638 ± 0.0000	0.2321 ± 0.0046	0.0002 ± 0.0485	0.0015 ± 0.0329	0.001	0.050	6.12	5.226 ± 0.037	24.53 ± 0.17
3.50	2621 ± 5	19.924 ± 0.079	5.5022 ± 0.0020	0.2418 ± 0.0045	0.0002 ± 0.6616	0.0015 ± 0.0195	0.044	0.052	6.42	5.154 ± 0.028	24.21 ± 0.13
11.1	2642 ± 4	38.223 ± 0.151	5.5901 ± 0.0020	0.2358 ± 0.0045	0.0001 ± 0.0450	0.0020 ± 0.0125	0.001	0.050	8.89	5.099 ± 0.026	24.14 ± 0.12
21.5	2667 ± 5	13.377 ± 0.054	5.5634 ± 0.0020	0.2498 ± 0.0049	0.0003 ± 0.7626	0.0021 ± 0.0378	0.003	0.054	8.83	5.075 ± 0.051	24.25 ± 0.24
30.0	2682 ± 6	22.370 ± 0.089	5.2860 ± 0.0020	0.2444 ± 0.0046	0.0002 ± 0.5973	0.0011 ± 0.0283	0.040	0.052	4.74	5.040 ± 0.028	24.22 ± 0.14
40.0	2695 ± 7	9.293 ± 0.038	7.2687 ± 0.0020	0.2335 ± 0.0054	0.0004 ± 0.0195	0.0081 ± 0.0103	0.001	0.050	30.33	5.066 ± 0.054	24.47 ± 0.26
47.5	2701 ± 7	20.203 ± 0.080	5.4928 ± 0.0020	0.2310 ± 0.0047	0.0002 ± 0.7936	0.0018 ± 0.0243	0.013	0.049	7.74	5.071 ± 0.033	24.54 ± 0.16
51.5	2703 ± 7	19.546 ± 0.078	5.4116 ± 0.0020	0.2315 ± 0.0047	0.0002 ± 0.8977	0.0015 ± 0.0238	0.014	0.049	6.42	5.068 ± 0.030	24.55 ± 0.14
62.0	2704 ± 7	15.009 ± 0.060	5.8512 ± 0.0020	0.2293 ± 0.0049	0.0002 ± 0.0278	0.0032 ± 0.0123	0.001	0.049	14.01	5.035 ± 0.032	24.39 ± 0.15
71.5	2700 ± 6	9.354 ± 0.038	5.7754 ± 0.0020	0.2251 ± 0.0055	0.0004 ± 0.1411	0.0028 ± 0.0207	0.001	0.048	11.65	5.104 ± 0.040	24.69 ± 0.19
80.1	2692 ± 6	13.621 ± 0.054	5.6764 ± 0.0020	0.2303 ± 0.0051	0.0003 ± 5.9844	0.0024 ± 0.0180	0.034	0.049	10.46	5.088 ± 0.033	24.54 ± 0.16
99.9	2658 ± 7	21.289 ± 0.084	5.4751 ± 0.0020	0.2345 ± 0.0047	0.0002 ± 0.4894	0.0016 ± 0.0216	0.041	0.050	7.28	5.083 ± 0.030	24.21 ± 0.14
100.5	2656 ± 7	20.080 ± 0.079	5.5110 ± 0.0020	0.2359 ± 0.0047	0.0002 ± 0.0152	0.0017 ± 0.0215	0.001	0.050	7.51	5.103 ± 0.030	24.29 ± 0.14
							0.015[d]	0.050[d]	9.17[d]	5.093 ± 0.046[e]	24.36 ± 0.17[e]

Isotope production ratios from Deckart (1996): $(^{40}Ar/^{39}Ar)_K = 0.0302$, $(^{37}Ar/^{39}Ar)_{Ca} = 1416.4306$, $(^{36}Ar/^{39}Ar)_{Ca} = 0.3952$, Ca/K = 1.83 x $(^{37}Ar_{Ca}/^{39}Ar_K)$.

[a] - blank and decay-corrected ratios

[b] - age of TCRsan (Renne et al., 1998)

[c] - height above base of irradiation cannister in millimetres

[d] - arithmetic mean

[e] - weighted mean (based on errors)

[f] - weighted mean age of MAC-83 for this cannister (based on errors)

Table 5. ^{40}Ar-^{39}Ar laser total-fusion geochronological data for irradiation cannister 2, including twelve monitors (eight TCRsan and four FCTsan) and thirteen aliquots of the 710–355 μm size fraction of MAC-83 biotite. All errors are quoted at 2σ level.

Position in can	J-value (x 10^6)	vol ^{39}Ar (x 10^{-10} cm³)	^{40}Ar/^{39}Ar	Isotope ratios[a]		^{36}Ar/^{39}Ar	Ca/K	Cl/K	%^{40}Ar$_{Atm}$	^{40}Ar*/^{39}Ar$_K$	Age (Ma)
				^{38}Ar/^{39}Ar	^{37}Ar/^{39}Ar						
TCR-san (28.34 Ma)[b]											
1.0[c]	2316 ± 21	11.703 ± 0.050	6.8367 ± 0.0021	0.0130 ± 0.0166	0.0077 ± 0.0196	0.0004 ± 0.5011	0.039	0.000	0.15	6.838 ± 0.128	28.34
15.0	2368 ± 20	13.791 ± 0.059	6.7014 ± 0.0021	0.0127 ± 0.0129	0.0023 ± 0.0506	0.0004 ± 0.5168	0.035	0.000	0.34	6.686 ± 0.115	28.34
26.5	2358 ± 22	16.554 ± 0.071	6.7120 ± 0.0021	0.0125 ± 0.0113	0.0022 ± 0.0461	0.0003 ± 0.8024	0.035	0.000	0.09	6.714 ± 0.128	28.34
38.2	2366 ± 18	15.582 ± 0.067	6.6788 ± 0.0021	0.0128 ± 0.0130	0.0077 ± 0.0155	0.0003 ± 0.6119	0.040	0.000	0.00	6.691 ± 0.105	28.34
44.9	2363 ± 15	16.808 ± 0.072	6.7346 ± 0.0021	0.0128 ± 0.0108	0.0025 ± 0.0359	0.0004 ± 0.3498	0.040	0.000	0.65	6.699 ± 0.085	28.34
55.0	2370 ± 16	14.055 ± 0.060	7.0009 ± 0.0021	0.0126 ± 0.0127	0.0025 ± 0.0425	0.0014 ± 0.1003	0.040	0.000	4.67	6.682 ± 0.089	28.34
67.5	2357 ± 12	20.214 ± 0.086	6.7445 ± 0.0021	0.0125 ± 0.0096	0.0025 ± 0.0298	0.0003 ± 0.3337	0.042	0.000	0.54	6.717 ± 0.071	28.34
77.8	2341 ± 15	18.566 ± 0.079	6.7598 ± 0.0021	0.0128 ± 0.0111	0.0073 ± 0.0139	0.0003 ± 0.5240	0.038	0.000	0.11	6.764 ± 0.089	28.34
							0.039[d]	0.000[d]	0.82[d]	6.719 ± 0.038[e]	
FCT-san (28.02 Ma)[f]											
2.6	2364 ± 10	31.362 ± 0.134	6.7439 ± 0.0021	0.0125 ± 0.0071	0.0031 ± 0.0165	0.0003 ± 0.2542	0.052	0.000	0.81	6.699 ± 0.056	28.02
39.2	2363 ± 10	23.837 ± 0.102	6.7674 ± 0.0021	0.0128 ± 0.0083	0.0011 ± 0.0536	0.0007 ± 0.1241	0.016	0.000	2.22	6.625 ± 0.058	28.02
55.9	2359 ± 28	17.084 ± 0.073	6.6367 ± 0.0021	0.0126 ± 0.0110	0.0009 ± 0.1026	0.0003 ± 1.0313	0.010	0.000	6.69	6.634 ± 0.164	28.02
79.5	2332 ± 11	30.772 ± 0.131	6.7983 ± 0.0021	0.0125 ± 0.0087	0.0027 ± 0.0241	0.0005 ± 0.1800	0.043	0.000	1.41	6.711 ± 0.062	28.02
							0.030[d]	0.000[d]	2.78[d]	6.676 ± 0.038[e]	
MAC-83 bio (24.44 Ma)[g]											
0.1	2352 ± 13	6.300 ± 0.027	6.1399 ± 0.0021	0.2404 ± 0.0050	0.0027 ± 0.1014	0.0015 ± 0.2492	0.009	0.052	3.73	5.913 ± 0.225	24.92 ± 0.94
8.5	2359 ± 10	14.901 ± 0.064	6.2472 ± 0.0021	0.2405 ± 0.0048	0.0033 ± 0.0328	0.0019 ± 0.0681	0.053	0.052	7.49	5.782 ± 0.083	24.44 ± 0.35
14.6	2363 ± 8	7.523 ± 0.032	6.3747 ± 0.0000	0.2330 ± 0.0049	0.0020 ± 0.0975	0.0024 ± 0.1091	0.023	0.050	8.52	5.833 ± 0.160	24.70 ± 0.67
21.0	2365 ± 9	11.787 ± 0.050	6.1901 ± 0.0021	0.2297 ± 0.0049	0.0043 ± 0.0349	0.0017 ± 0.1196	0.020	0.049	5.89	5.830 ± 0.122	24.71 ± 0.51
31.5	2367 ± 9	11.858 ± 0.051	6.3610 ± 0.0021	0.2330 ± 0.0048	0.0032 ± 0.0392	0.0024 ± 0.0659	0.051	0.050	9.39	5.766 ± 0.099	24.45 ± 0.42
37.6	2367 ± 9	12.571 ± 0.054	6.0287 ± 0.0021	0.2337 ± 0.0049	0.0067 ± 0.0237	0.0012 ± 0.1718	0.033	0.050	3.73	5.808 ± 0.127	24.63 ± 0.54
41.0	2367 ± 9	17.889 ± 0.076	6.1337 ± 0.0021	0.2303 ± 0.0048	0.0026 ± 0.0331	0.0017 ± 0.0683	0.042	0.049	6.61	5.731 ± 0.073	24.31 ± 0.31
44.4	2366 ± 9	10.133 ± 0.043	6.4171 ± 0.0021	0.2313 ± 0.0049	0.0013 ± 0.1112	0.0026 ± 0.0721	0.013	0.049	9.92	5.782 ± 0.116	24.51 ± 0.49
49.0	2364 ± 8	17.602 ± 0.075	6.4934 ± 0.0021	0.2344 ± 0.0048	0.0073 ± 0.0167	0.0029 ± 0.0535	0.037	0.050	11.32	5.763 ± 0.095	24.41 ± 0.40
61.5	2356 ± 7	18.375 ± 0.078	6.1558 ± 0.0021	0.2271 ± 0.0048	0.0027 ± 0.0287	0.0017 ± 0.0607	0.045	0.049	6.78	5.741 ± 0.067	24.24 ± 0.28
67.1	2351 ± 7	10.844 ± 0.046	6.4004 ± 0.0021	0.2333 ± 0.0048	0.0016 ± 0.0911	0.0024 ± 0.0795	0.021	0.050	8.81	5.839 ± 0.115	24.60 ± 0.48
72.0	2346 ± 8	9.873 ± 0.042	6.4501 ± 0.0021	0.2424 ± 0.0048	0.0043 ± 0.0351	0.0027 ± 0.0764	0.068	0.052	10.09	5.802 ± 0.126	24.39 ± 0.52
76.6	2341 ± 10	7.134 ± 0.031	6.2421 ± 0.0021	0.2336 ± 0.0050	0.0079 ± 0.0308	0.0018 ± 0.1865	0.038	0.050	5.03	5.931 ± 0.196	24.88 ± 0.82
							0.037[d]	0.050[d]	7.70[d]	5.779 ± 0.045[e]	24.44 ± 0.17[e]

Isotope production ratios from Deckart (1996): $(^{40}Ar/^{39}Ar)_K = 0.0302$, $(^{37}Ar/^{39}Ar)_{Ca} = 1416.4306$, $(^{36}Ar/^{39}Ar)_{Ca} = 0.3952$, Ca/K = 1.83 x $(^{37}Ar_{Ca}/^{39}Ar_K)$.

[a] - blank and decay-corrected isotopic ratios
[b] - age of TCRsan (Renne et al., 1998)
[c] - height above base of irradiation cannister in millimetres
[d] - arithmetic mean
[e] - weighted mean (based on errors)
[f] - age of FCT-san (Renne et al., 1998)
[g] - weighted mean age of MAC-83 for this cannister (based on errors)

an attempt to evenly split gas released from each grain. Sample geometry, size, and placement prevented exact replication of gas splitting, with only aliquot B giving roughly equal gas quantities. Because each aliquot was subject to the same J-factor, data are compared for reproducibility and then combined and treated as a single step-heating analysis, and J-factor uncertainty is applied to arrive at a final age and analytical error. Results (Table 6) are plotted as a 'stacked' gas-release spectrum (Fig. 8) in which the total ^{39}Ar released from all aliquots is normalized to 100% and the quantity of gas released from individual aliquots is plotted relative to this amount. Alternatively, data are plotted on a correlation plot (Fig. 9) and regressed using a modified York (1969) regression.

Three single-grain aliquots were analyzed and, although an even gas split was achieved only in aliquot B, the four subequal gas fractions give reproducible results, indicating a high degree of homogeneity between grains. When the data are combined and weighted for error and gas quantity, an age of 24.36 ± 0.32 Ma is obtained. A correlation plot (Fig. 9), excluding the two small gas fractions, but regressing through the atmospheric air value of 295.5, yielded an age of 24.39 ± 0.23 Ma (M.S.W.D = 1.27). Although not obvious from this data set, multigrain fractions analyzed by multistep heating give an indication of a minor excess-argon component with ^{40}Ar/^{36}Ar = 333 ± 10 (M. Villeneuve and A. Daze, unpubl. data, 1997), a value that is in allowable agreement with the regression of the three most radiogenic points on Figure 9 (^{40}Ar/^{36}Ar = 350 ± 110: M.S.W.D. = 0.02), which results in a slightly younger age of 24.27 ± 0.48 Ma.

Table 6. ^{40}Ar-^{39}Ar laser geochronological data for six analyses of the 1000–710 µm size fraction of MAC-83 biotite analyzed at the Geological Survey of Canada.

Power (W)	Volume ^{39}Ar (x 10^{-11} cm^3)	^{40}Ar/^{39}Ar	^{38}Ar/^{39}Ar	^{37}Ar/^{39}Ar	^{36}Ar/^{39}Ar	Ca/K	Cl/K	%^{40}Ar ATM	f^{39}Ar	^{40}Ar*/^{39}Ar	Apparent age (Ma)
Aliquot A											
20	4.2686	7.9368	0.2211	0.0278	0.0017	0.051	0.037	6.2	0.292	7.442 ± 1.079	24.56 ± 0.26
40	0.0053	106.4231	0.3774	5.8868	0.3019	10.729	0.064	81.8	0.000	19.232 ± 626.7	62.78 ± 386.60
Aliquot B											
15	4.0788	8.5984	0.2238	0.0266	0.0042	0.049	0.038	14.5	0.279	7.348 ± 0.916	24.25 ± 0.22
45	3.3188	7.5982	0.2296	0.0776	0.0007	0.142	0.039	2.8	0.227	7.389 ± 0.866	24.38 ± 0.21
Aliquot C											
15	2.8694	7.7799	0.2061	0.0229	0.0013	0.042	0.034	4.8	0.196	7.406 ± 2.369	24.43 ± 0.57
45	0.0969	13.6328	0.4654	1.9804	0.033	3.623	0.078	71.6	0.007	3.865 ± 46.94	12.80 ± 5.98
Integrated age = 24.32 ± 0.32 Ma (referenced to FCT-San = 28.02 Ma; Renne et al., 1994); J factor = 0.001841 ± 0.000018 (2σ)											

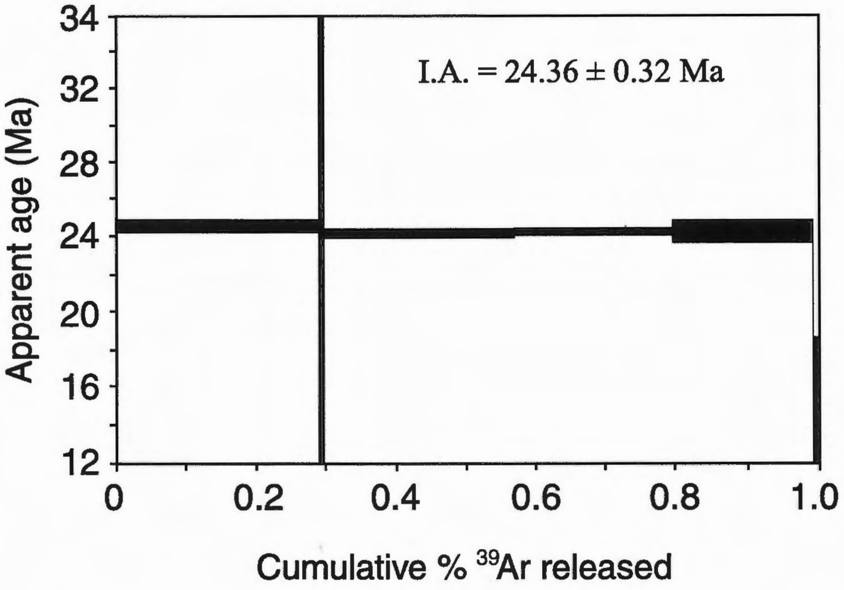

Figure 8.

Composite, laser step-heating age spectrum for three grains of the 1000–710 µm MAC-83 biotite separate calibrated against FCTsan (28.02 Ma; Renne et al., 1998), obtained at the Argon Laboratory of the Geological Survey of Canada. I.A. = total gas integrated age

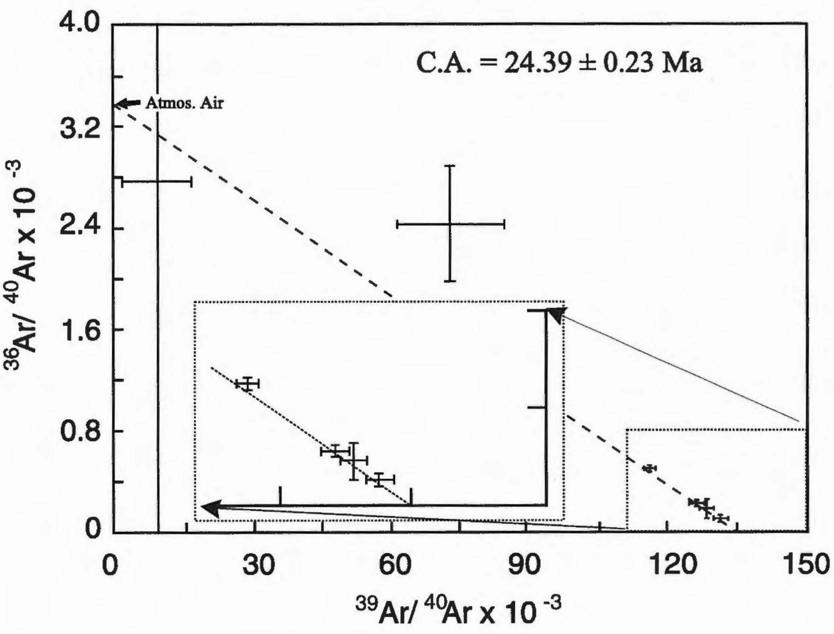

Figure 9.

Inverse isochron correlation plot for the six analyses of MAC-83 obtained at the Geological Survey of Canada. The inset shows the four most radiogenic aliquots that yield a correlation age of 24.39 ± 0.23 Ma when the Y-intercept is forced to an atmospheric value of 295.5. C.A. = correlation age.

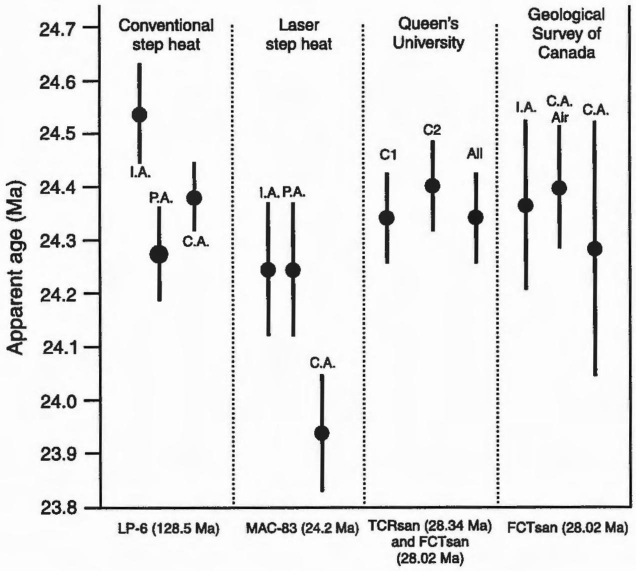

Figure 10. *Graph summarizing the geochronological data presented in the report for MAC-83 biotite. The monitors used in the calibrations are listed below each column. I.A. = integrated age; P.A. = plateau age; CA = inverse isotope correlation age. For the two columns on the right, C1 = weighted mean age for cannister 1; C2 = weighted mean age for cannister 2; All = weighted mean age (based on errors) of all 26 total-fusion analyses of MAC-83 biotite.*

DISCUSSION

MAC-83 is a specimen of fresh, glass-bearing, volcanic rock at the base of a well documented pyroclastic volcanic sequence exposed in the Cordillera Oriental of southeastern Peru. The fresh character of the rock and its abundant biotite (ca. 13 volume %) make for an excellent reference material for laser ^{40}Ar-^{39}Ar geochronology. The experimental results presented herein demonstrate that the biotite is chemically homogeneous (at least with respect to major elements) and yields consistent and reproducible ^{40}Ar-^{39}Ar results on the 710–355 μm fraction when calibrated against the international standards TCRsan and FCTsan2. For the two separate irradiation cannisters, the biotite yielded error-weighted mean ages of 24.36 ± 0.17 Ma and 24.44 ± 0.17 Ma respectively; however, statistical treatment of all 26 data yields an error-weighted mean age of 24.36 ± 0.17 Ma. We consider that, with respect to the two flux monitors TCRsan and FCTsan, this represents the best estimate of the true age of the biotite. The biotite yields highly reproducible ^{40}Ar*/^{39}Ar$_{K}$ ratios (for each respective irradiation), low, but variable, ^{40}Ar$_{ATM}$ (8.643 ± 9.952), and very consistent mass-spectrometry-estimated Ca/K (0.025 ± 0.040) and Cl/K (0.050 ± 0.002) ratios that are apparently higher than those derived from 50 electron microprobe analyses of 10 grains of the 710–355 μm size fraction. The difference in the Ca/K and Cl/K ratios as determined through mass spectrometry and electron microprobe analysis may reflect an erroneous choice of the nuclear production ratios (Deckart, 1996), but we consider that these differences most probably arise because of additional Ca and Cl derived from apatite inclusions in the biotite grains. Hence, the mass spectrometry measurements include argon from apatite inclusions during laser fusion of the biotite grains that were avoided with the electron microprobe. Because of its consistent Cl/K values as determined through mass spectrometry, MAC-83 may be a good Cl standard for ^{40}Ar-^{39}Ar geochronology. The presence of Cl, however, requires an appropriate correction for Ar-isotopes induced from chlorine during irradiation.

A graphical summary of all geochronological data obtained herein is presented in Figure 10. The values for the final, best estimate ages determined at Queen's University, including the step-heating and total-fusion analyses, and those determined at the Geological Survey of Canada overlap in error. This is the case for all values except the inverse correlation age determined for the laser step-heating age for the 710–1000 μm grains analyzed at Queen's University. We emphasize, however, that the monitors used to determine the J-value for this unknown comprised aliquots of the 354–710 μm fraction of MAC-83 and used an age of 24.2 Ma. Hence, the integrated, plateau, and correlation ages for the laser step-heating analysis are all somewhat lower than expected. Overall, the conventional step-heating and laser data show excellent agreement, representing results from two different laboratories. However, the presence of a component of excess ^{40}Ar in the biotite as shown by the inverse isotope correlation and age spectrum plots suggests that some caution is required when interpreting the accuracy of the determined age. The accuracy of this ^{40}Ar-^{39}Ar age will be evaluated through comparison with U-Pb and Th-Pb dating of monazite extracted from the same specimen.

ACKNOWLEDGMENTS

We wish to dedicate this contribution to Chris Roddick, as it formed part of the *Chris Roddick Symposium II: New Advances in the Understanding and Application of Ar Isotope Systematics* at the Geological Association of Canada — Mineralogical Association of Canada Joint Annual Meeting in Québec City, Canada (1998). Laboratory costs at Queen's University were graciously covered by Dr. Ed Farrar of Queen's University through a Natural Sciences and Engineering Research Council of Canada operating grant. This work would not have been possible without the laboratory assistance generously supplied by Anne Sasso, Karen Fallas, and Fred Quigg. This manuscript benefited from a review by Otto van Breemen.

REFERENCES

Alexander, E.C., Jr., Michelson, G.M., and Lanphere, M.A.
1978: MMHb-1: A new ^{40}Ar-^{39}Ar dating standard; *in* Short Papers of the Fourth International Conference, Geochronology, Cosmochronology and Isotope Geology, (ed.) R.E. Zartman; United States Geological Survey, Open File Report 78-701, p. 6–8.

Baksi, A.K., Archibald, D.A., and Farrar, E.
1996: Intercalibration of ^{40}Ar/^{39}Ar dating standards; Chemical Geology, v. 129, p. 307–324.

Baksi, A.K., Hoffman, K.A., and McWilliams, M.
1993: Testing the accuracy of the geomagnetic polarity time-scale (GPTS) at 2–5 Ma, utilizing ^{40}Ar/^{39}Ar incremental heating data on whole-rock basalts; Earth and Planetary Science Letters, v. 118, p. 135–144.

Bevington, P.R.
1969: Data Reduction and Error Analysis for the Physical Sciences; McGraw Hill Inc., 336 p.

Cebula, G.T., Kunk, M.J., Mehnert, H.H., Naeser, C.W., Obradovich, J.D., and Sutter, J.F.
1986: The Fish Canyon Tuff, a potential standard for the ^{40}Ar-^{39}Ar and fission-track dating methods; Terra Cognita, v. 6, p. 139–140 (abstract).

Dalrymple, G.B., Alexander, E.C., Lanphere, M.A., and Kraker, G.P.
1981: Irradiation of samples for ^{40}Ar/^{39}Ar using the Geological Survey TRIGA Reactor; United States Geological Survey, Professional Paper 1176, 55 p.

Dalrymple, G.B., Izett, G.A., Snee, L.W., and Obradovich, J.D.
1993: ^{40}Ar/^{39}Ar age spectra and total-fusion ages of tektites from Cretaceous–Tertiary boundary sedimentary rocks in the Beloc Formation, Haiti; United States Geological Survey Bulletin 2056, 20 p.

Deckart, K.
1996: Étude du magmatisme associé au rifting de l'Atlantique central et sud: géochronologie ^{40}Ar/^{39}Ar et géochimie sur les intrusions jurassiques de Guinée et Guyane française/Surinam et crétacées du Brésil; thèse de doctorat, Université de Nice/Sophia Antipolis; Géosciences Azur, 221 p.

Ingamells, C.O. and Engels, J.C.
1976: Preparation, analysis, and sampling constants for a biotite; United States National Bureau of Standards Special Publication, v. 422, p. 403-419.

Lanphere, M.A. and Baadsgaard, H.
1997: The Fish Canyon Tuff: a standard for geochronology; Transactions, Geological Society of America Annual Spring Meeting (abstract), p. S326.

Press, W.H., Flannery, B.P., Teukolsky, S.A., and Vetterling, W.T.
1989: Numerical Recipes in Pascal: The Art of Scientific Computing; Cambridge University Press, Cambridge, 759 p.

Renne, P.R., Deino, A.L., Walter, R.C., Turrin, B.D., Swisher, C.C., III, Becker, T.A., Curtis, G.H., Sharp, W.D., and Jaouni, A.
1994: Intercalibration of astronomical and radioisotopic time; Geology, v. 22, p. 783–786.

Renne, P.R., Swisher, C.C., III, Deino, A.L., Karner, D.B., Owens, T.L., and DePaolo, D.J.
1998: Intercalibration of standards, absolute ages and uncertainties in ^{40}Ar/^{39}Ar dating; Chemical Geology, v. 145, p. 117–152.

Roddick, J.C.
1983: High precision intercalibration of ^{40}Ar/^{39}Ar standards; Geochimica et Cosmochimica Acta, v. 47, p. 887–898.

Sandeman, H.A., Clark, A.H., Farrar, E., and Arroyo, G.
1997a: Lithostratigraphy, petrology, and ^{40}Ar-^{39}Ar geochronology of the Crucero Supergroup, Puno Department, SE Peru; Journal of South American Earth Sciences, v. 10, p. 223–245.

Sandeman, H.A., Clark, A.H., Styles, M.T., Scott, D.J., Malpas, J.G., and Farrar, E.
1997b: Geochemistry and U-Pb and ^{40}Ar-^{39}Ar geochronology of the Man of War Gneiss, Lizard Complex, SW England: pre-Hercynian arc-type crust with a Sudetan-Iberian connection; Journal of the Geological Society of London, v. 154, p. 403–417.

Steiger, R.H. and Jäger, E.
1977: Subcommision on geochronology: Convention on the use of decay constants in geo- and cosmochronology; Earth and Planetary Science Letters, v. 36, p. 359–362.

Villeneuve, M.E. and MacIntyre, D.M.
1997: Laser ^{40}Ar/^{39}Ar ages of the Babine Porphyries and Newman Volcanics, Fulton Lake map area (93L/16), west-central British Columbia; *in* Radiogenic Age and Isotopic Studies, Report 10; Geological Survey of Canada, Current Research 1997-F, p. 131–140.

York, D.
1969: Least squares fitting of a straight line with correlated errors; Earth and Planetary Science Letters, v. 5, p. 320–324.

– 4 –

Calibration of a Neogene magnetostratigraphy by ^{40}Ar-^{39}Ar geochronology: the foreland basin strata of northern Mendoza Province, Argentina

M.V. Irigoyen[1], M.E. Villeneuve[2], and F. Quigg[2]

Irigoyen, M.V., Villeneuve, M.E., and Quigg, F., 1999: Calibration of a Neogene magnetostratigraphy by ^{40}Ar-^{39}Ar geochronology: the foreland basin strata of northern Mendoza Province, Argentina; in *Radiogenic Age and Isotopic Studies: Report 12; Geological Survey of Canada, Current Research 1999-F, p. 27–41.*

Abstract: Neogene strata exposed in the southernmost part of the Precordillera fold-and-thrust belt, Mendoza Province, Argentina, record the eastward migration of the Andean deformation front since the middle Miocene. In order to link the sequence of deformational events occurring in the western thrust belts with the sedimentary record, the Neogene succession has been dated using magnetic polarity stratigraphy calibrated with ^{40}Ar-^{39}Ar isotopic dates. This paper reports on age determinations obtained by ^{40}Ar-^{39}Ar isotopic dating of six tuff beds interbedded in the Neogene sequence, which assist in tying the local magnetostratigraphy to the geomagnetic polarity time scale. In addition, the age results of two samples collected from air-fall tuff horizons interbedded in Quaternary deposits, which have been dated to provide temporal constraints on the age of the youngest Mogotes Formation and the timing of the formation of major structures in the region, are presented.

Résumé : Les couches du Néogène qui affleurent dans l'extrême sud de la zone de plissement et de chevauchement de la Précordillère de la Province de Mendoza, en Argentine, attestent la migration vers l'est du front de déformation des Andes à partir du Miocène moyen. Afin d'établir un lien entre la suite des déformations qui se sont produites dans les zones de chevauchement de l'ouest et les événements sédimentaires, on a déterminé l'âge de la séquence du Néogène en utilisant la magnétostratigraphie étalonnée sur des âges isotopiques ^{40}Ar-^{39}Ar. La présente étude expose les âges obtenus par datation isotopique ^{40}Ar-^{39}Ar de six couches de tuf interstratifiées dans la séquence du Néogène, qui contribuent à établir un lien entre la magnétostratigraphie locale et l'échelle chronologique de la polarité géomagnétique. Sont également présentés les résultats obtenus relativement à l'âge de deux échantillons prélevés dans les horizons de tuf retombé interstratifiés dans des dépôts du Quaternaire qui ont été datés afin d'imposer des contraintes temporelles à l'âge de la plus jeune formation, la Formation de Mogotes, et à la chronologie de la formation des structures majeures présentes dans la région.

---

[1] Servicio Geológico Minero Argentino (SEGEMAR), Julio A. Roca 651, Piso 10, (1322) Buenos Aires, Argentina

[2] Continental Geoscience Division, Geological Survey of Canada, 601 Booth Street, Ottawa, Ontario K1A 0E8

INTRODUCTION

The study area is located along the eastern flank of the Andes, in the southernmost portion of the Precordillera Mountains, where the thrust-and-fold belt dies out as a physiographic unit approximately at latitude 33°S (Fig. 1). The region of the Precordillera Mountains between latitude 28°S and latitude 33°S is characterized by Paleozoic strata that trend nearly north and are generally imbricated on east-verging thrust faults (e.g. Baldis and Chebli, 1969). At about latitude 33°S, the thrust belt is expressed at surface by an approximately 4000 m thick succession of deformed Tertiary strata. These synorogenic deposits record exhumation, deformation, and denudation of the thrust belts to the west, namely the Principal and Frontal cordilleras of the Andes.

The Principal Cordillera or Main Andes is composed primarily of a thick sequence of Jurassic and Cretaceous marine deposits, which interfinger with an Upper Jurassic–Lower Cretaceous andesitic volcanic complex (Yrigoyen, 1979). These deposits, which are unconformably overlain by the ~4000 m thick Miocene volcaniclastic succession of the Complejo Volcánico Aconcagua (Ramos et al., 1996), display a thin-skinned structure and form the Early to Late Miocene Aconcagua fold-and thrust belt (Ramos, 1988). The Frontal Cordillera comprises mainly late Paleozoic to early Mesozoic, andesitic to silicic magmatic rocks of the Choiyoi Group (Caminos, 1979). Just west of the study area, along the Cordón del Plata, the Frontal Cordillera exposes a thick sequence of Carboniferous strata and limited outcrops of Tertiary synorogenic sedimentary rocks. An imbricate structure developed in the late Pliocene to early (?)Pleistocene (Caminos, 1979) bounds the Frontal Cordillera to the east.

Rocks exposed in the study area range from early Paleozoic to late Cenozoic (Fig. 2). The oldest outcrop in and around the La Pilona anticline (Fig. 2a) and consist of Ordovician low-grade metasedimentary strata intruded by Silurian monzodiorite and monzogabbro (Varela et al. 1993). Permian–Triassic volcanic and plutonic rocks of the Choiyoi Group exposed in the Cacheuta peak are mainly andesites, rhyolites, and felsic granitic rocks. Middle to Upper Triassic nonmarine strata and subordinate volcanic rocks overlie the volcanic rocks of the Choiyoi Group. These Triassic deposits are the source rock of the oil-producing La Pilona structure. About 3500–4000 m of deformed Paleogene to Pliocene continental deposits disconformably overlie the Triassic strata (Rolleri and Fernández Garrasino, 1979).

The geochronological study of the Neogene succession was mainly carried out in the south-plunging La Pilona anticline, which exposes the most complete record of the Cenozoic succession. Exposures were also studied on the eastern flank of the Tupungato anticline, approximately 20–25 km south (Fig. 2b).

Six Tertiary formations outcrop in the La Pilona area (Fig. 2). All but the oldest Divisadero Largo Formation are Neogene. The oldest Neogene strata, the Mariño Formation, is subdivided into three members. The lowest member, 'Conglomerados violáceos' (purple conglomerates), reaches approximately 50 m in thickness and consists of purple conglomeratic beds alternating with greenish sandstone. The intermediate member, 'Areniscas entrecruzadas' (crossbedded sandstones), comprises mainly eolian crossbedded sandstone about 200 m thick. The upper member, 'Estratos de Mariño' (Mariño strata), is about 1000 m thick and consists of fluvial-alluvial sandstone interbedded with red mudstone and gray conglomerate.

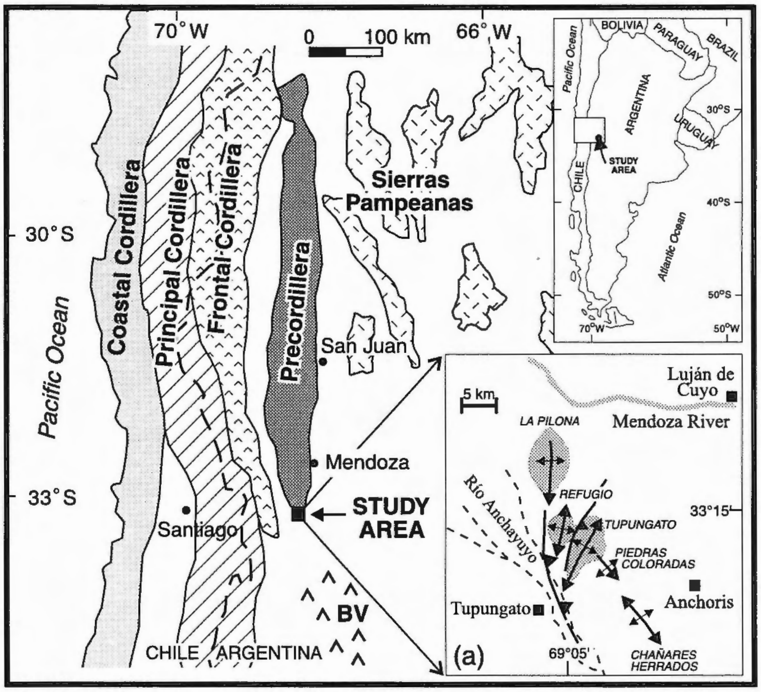

Figure 1.

*Map and location of the study area showing the major morphostructural units of the central Andes (after Ramos, 1988). BV = back-arc volcanic province. (**a**) Detail of the La Pilona and Tupungato anticlines, the two study localities.*

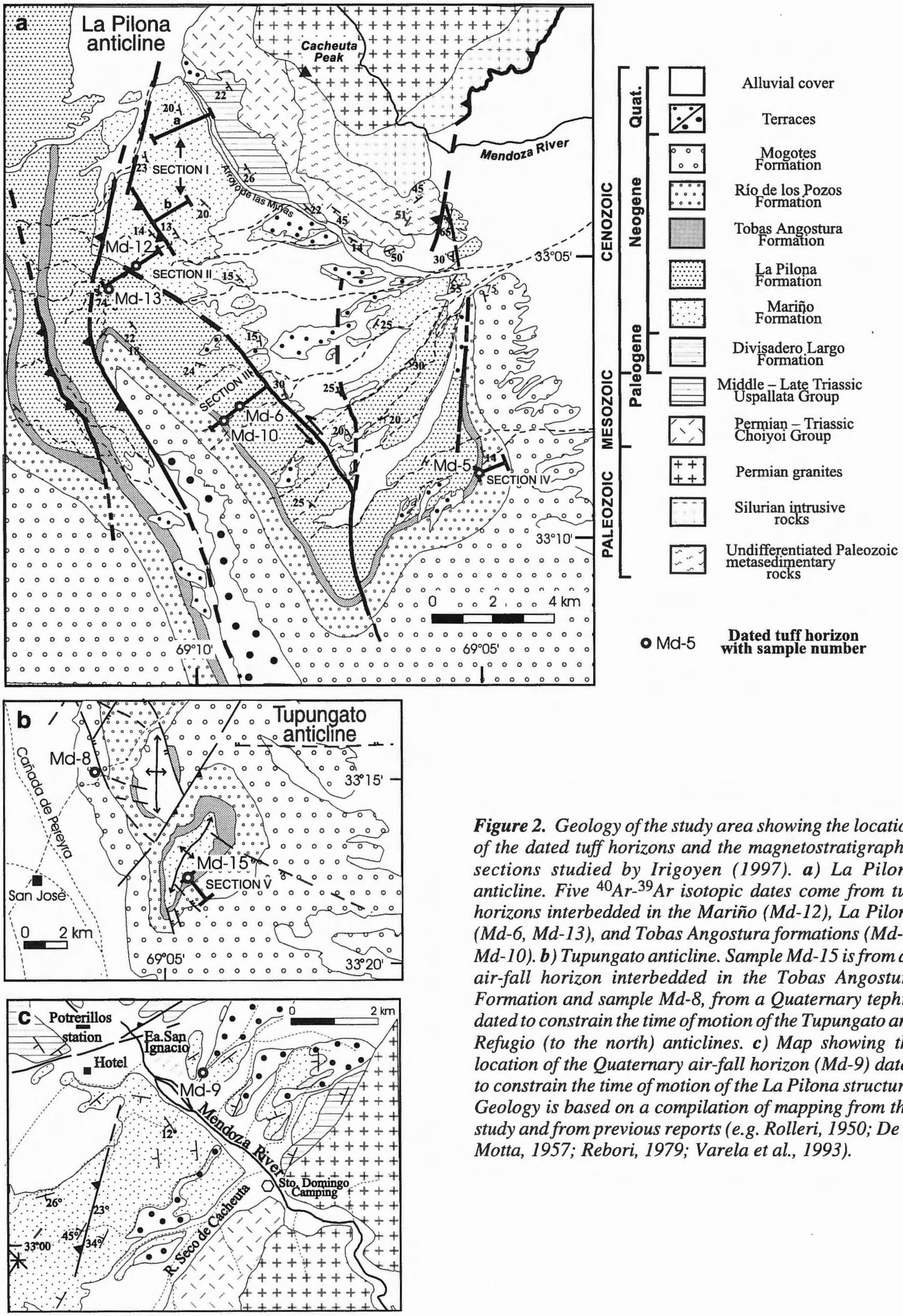

Figure 2. *Geology of the study area showing the location of the dated tuff horizons and the magnetostratigraphic sections studied by Irigoyen (1997).* ***a)*** *La Pilona anticline. Five* ^{40}*Ar-*^{39}*Ar isotopic dates come from tuff horizons interbedded in the Mariño (Md-12), La Pilona (Md-6, Md-13), and Tobas Angostura formations (Md-5, Md-10).* ***b)*** *Tupungato anticline. Sample Md-15 is from an air-fall horizon interbedded in the Tobas Angostura Formation and sample Md-8, from a Quaternary tephra dated to constrain the time of motion of the Tupungato and Refugio (to the north) anticlines.* ***c)*** *Map showing the location of the Quaternary air-fall horizon (Md-9) dated to constrain the time of motion of the La Pilona structure. Geology is based on a compilation of mapping from this study and from previous reports (e.g. Rolleri, 1950; De la Motta, 1957; Rebori, 1979; Varela et al., 1993).*

The La Pilona Formation, which includes strata previously mapped as 'Tobas Grises Inferiores' (lower gray tuffs; De la Motta, 1957), is up to about 800 m thick in the Cacheuta region. The lower third of this unit comprises gray sandstone and conglomerate overlain by a finer grained tuffaceous succession containing ash-fall horizons, one of which is the widely known 'Horizonte de Ceniza Blanca' (white ash horizon), which is laterally traceable for several hundred metres and has been dated in this study. The uppermost part of this unit consists of ~200 m thick conglomerate alternating with thin mudstone intervals.

The Tobas Angostura Formation, previously termed 'Tobas Grises Superiores' (upper gray tuffs; Truempy and Lhez, 1937), comprises volcanogenic deposits characterized by a distinctive gray colour and weathered appearance. It rests unconformably upon the La Pilona Formation and reaches a thickness of 100–120 m in the Tupungato area (Yrigoyen, 1993b). It comprises mainly reworked tuff, sandstone with varying amounts of pyroclastic material, air-fall horizons, and subordinate conglomerate horizons.

The Rio de los Pozos Formation, previously termed 'Serie Amarilla' (yellow sequence; Truempy and Lhez, 1937), is gradational from the Tobas Angostura unit. It comprises mudstone, tuffaceous mudstone, yellowish sandstone, and fine conglomerate. In the Tupungato area, its thickness varies from 230 to 400 m due to the unconformity separating it from the overlying Mogotes Formation.

The Mogotes Formation, which rests unconformably upon the Río de los Pozos Formation, is up to about 2000 m thick just west and south of the study area. It consists of boulder conglomerate interbedded with sandstone and mudstone, which probably represent proximal alluvial-fan facies, although a possible glacial origin has been suggested (Cortés, *in* Ramos, 1990). An erosional unconformity separates it from Quaternary strata consisting of widely developed pediments and several terraces, which contain intercalations of air-fall deposits (Polanski, 1963).

On the basis of on a magnetostratigraphic study carried out on the Neogene sequence, Irigoyen (1997) reported a detailed time stratigraphy based on comparison with the well established geomagnetic polarity time scale (G.P.T.S.; Baksi, 1993). This paper reports age determinations obtained by ^{40}Ar-^{39}Ar isotopic dating of six tuff beds interbedded in the Neogene sequence, which assist in tying the local magnetostratigraphy to the G.P.T.S. It also presents age results for two samples collected from air-fall horizons interbedded in Quaternary deposits, which have been dated to provide temporal constraints to the age of the youngest Mogotes Formation and to the timing of formation of the La Pilona and Tupungato structures. The location of the study samples is shown in Figure 2a-c.

METHODOLOGY

Mineral separates of visually unaltered glass, biotite and hornblende were dated using ^{40}Ar-^{39}Ar step-heating and laser fusion. A first set of mineral separates was analyzed in 1993–1994 using resistance furnace step-heating and laser total-fusion techniques at the Massachusetts Institute of Technology (MIT) facility.

About 3 kg of fresh material was collected in the study area from each of the eight tuff horizons. Mineral separations for all samples involved crushing as necessary, hand magnetic and Frantz separation, shaking water table, sieving, heavy-liquid techniques, and, lastly, handpicking to achieve >99% purity in all mineral separates. Hand-picked separates consisted of 100–300 μm, vesicle-free glass, 160–300 μm hornblende, and dark, inclusion-free biotite. Aliquots used for laser step-heating weighed approximately 10–100 μg, 100 to 500 times less than those used for furnace step-heating.

The separates were loaded into individual aluminium foil packets for neutron irradiation. Mineral irradiation was performed in the research reactor at McMaster University, Hamilton, Ontario. The first set of samples consisted of four separates arranged in an aluminium can 40 mm long by 19 mm in diameter. These were irradiated for 1.4 hours in the central peak flux position 5C. Fast neutron flux was monitored using Fish Canyon Tuff Biotite (FCT-3) assumed to be equivalent in age (M.E. Villeneuve, unpub. data, 1998) to the Fish Canyon Tuff Sanidine (FCT-SAN) at 28.03 Ma (Renne et al., 1994); the J factor was ca. 3.5×10^{-4}.

Argon extraction was accomplished by resistance furnace step-heating and laser fusion at the MIT laboratory. Furnace step-heating extractions were performed using a double-vacuum assembly built by Modifications Ltd. The furnace temperature was measured with a Re-W thermocouple and controlled by a programmable system. The duration of the extraction was 5 min for each step. A ca. 100 mg hornblende from sample Md-10 was step-heated at 950°C, 1275°C, 1350°C, and 1600°C.

Laser total fusion experiments were performed on three mineral separates using a Coherent 10 W argon-ion laser in multiline mode. Several aliquots of each sample were placed into milled wells in a copper planchet that was inserted into a windowed vacuum chamber. Each each aliquot was heated for about 10 minutes using a defocused laser beam at a power of 5–8 W, which produced uniform glass beads of all analyzed material. Biotite separates from samples Md-5, Md-6, and Md-10 were analyzed by total fusion (Table 1). Each mineral separate was split into nine (Md-5, Md-6) or five (Md-10) aliquots of approximately four to five crystals each. Each aliquot was fused and the gas evolved was purified and analyzed.

In both furnace step-heating and laser-fusion experiments, evolved gasses were purified using a SAES AP-10 Al-Zr getter operated at about 973 K and three SAES ST-172 Fe-Zr-V getters operated at varying temperatures. Gettering time was 15 minutes for furnace extractions and 5 minutes for laser experiments. The purified gasses were analyzed with an MAP 215-50 mass spectrometer using a Faraday collector for furnace argon extractions and an electron multiplier for laser samples. This instrument has a sensitivity at M/e 40 of 6.8×10^{-6} cm³ STP/V for a trap current of 200 μA and an accelerating voltage of 3 kV with the Faraday configuration and 8.4 x 10^{-10} cm³ STP/V for the electron multiplier configuration. Details on these procedures and instruments are provided in Hodges et al. (1994).

A second set of samples was prepared in an identical fashion and processed in 1995 by laser step-heating at the Geological Survey of Canada. These samples consisted of nine mineral separates, five hornblende (40 mg each separate), three biotite (2.5–5 mg), and one glass (10 mg) arranged with other, unrelated samples in the Al can and irradiated in central peak flux position 5C for two hours. Neutron flux was monitored with 10 aliquots (0.20 mg each) of FCT-SAN (28.03 Ma; Renne et al., 1994); the resulting J parameter was approximately 4.85 x 10^{-4}. These form the bulk of the analyses reported herein.

At the GSC facility, each sample was split into several aliquots that were loaded into separate, 1.5 mm diameter by 4 mm deep wells in a copper planchet, which was placed under vacuum in a chamber topped with a Zn-Se window. This window is transparent to the beam of a Weck CO_2, 45 W surgical laser and was attenuated by 20X and stepped incrementally from 2 to 45 W power. The beam had a diameter of approximately 150 μm with roughly constant power distribution and was manually panned for one minute around each hole in an attempt to ensure even heating of the sample. However, some aliquots were too thickly layered in holes and only the top surfaces reached total fusion. Some higher wattage (temperature) steps could be contaminated by low-temperature gas release as melted surface material heated the sample buried in each hole. Because low-temperature argon loss apparently did not occur in most samples, its effects are considered to be minimal on the final age, although the amount of gas released may not correlate with the temperature of heating.

Table 1. Argon laser fusion data, Massachusetts Institute of Technology.

TEMP. (°C)	^{36}Ar	^{37}Ar	^{38}Ar	^{39}Ar	^{40}Ar	% Atmos.	APPARENT AGE Ma ± 2σ		^{39}Ar (%)
	(x10^{-9} cm³ STP)								
BIOTITE M5 (5.2 mg) J = 0.0003445 ± 0.50% 1σ									
1400	1.574	0.404	0.879	4.847	538.51	86.4	9.38	2.79	9.2
1400	1.699	0.432	1.011	5.736	580.02	86.6	8.43	0.62	10.9
1400	1.970	0.521	1.347	7.314	682.22	85.3	8.49	0.56	13.8
1400	1.549	0.378	1.151	7.121	554.60	82.5	8.44	0.26	13.5
1400	1.110	0.322	0.802	4.626	401.85	81.6	9.89	0.82	8.8
1400	2.026	0.363	1.137	6.398	688.14	87.0	8.67	1.59	12.1
1400	2.082	0.429	1.177	6.590	703.19	87.5	8.27	0.30	12.5
1400	0.981	0.235	0.712	4.340	355.58	81.5	9.40	0.38	8.2
1400	1.331	0.257	1.020	5.876	482.22	81.5	9.39	0.66	11.1
Total c	0.14	0.03	0.09	0.53	4986.3	84.9	8.85	0.4	
Conc.(/g)	27.54	6.43	17.76	101.6	958900				
BIOTITE M10 (2.12 mg) J = 0.0003445 ± 0.50% 1σ									
1400	0.831	0.252	0.887	5.913	322.38	76.1	8.07	0.56	22.7
1400	1.156	0.296	1.146	7.161	438.57	77.9	8.40	0.15	27.5
1400	0.354	0.110	0.514	3.306	153.00	68.3	9.08	0.43	12.7
1400	0.800	0.209	0.869	5.499	312.77	75.6	8.60	0.24	21.1
1400	0.791	0.155	0.711	4.131	286.67	81.5	7.96	0.31	15.9
Total c	0.04	0.01	0.04	0.26	1513.4	76.8	8.39		0.2
Conc.(/g)	18.54	4.82	19.47	122.7	713900				
BIOTITE M6 (4.67 mg) J = .0003445 ± 0.50% 1σ									
1400	1.182	0.326	0.263	3.495	414.23	84.3	11.5	0.6	7.6
1400	1.365	0.256	0.247	3.779	475.84	84.8	11.9	1.0	8.2
1400	1.251	0.260	0.252	3.974	436.49	84.7	10.4	0.5	8.6
1400	2.137	0.544	0.485	6.822	753.43	83.8	11.1	0.7	14.8
1400	2.232	0.606	0.577	8.522	810.33	81.4	11.0	0.6	18.5
1400	1.835	0.476	0.383	5.721	639.51	84.8	10.5	0.8	12.4
1400	1.609	0.438	0.361	4.890	554.57	85.7	10.0	0.9	10.6
1400	2.022	0.371	0.369	5.593	690.78	86.5	10.3	0.9	12.1
1400	1.447	0.217	0.235	3.390	482.12	88.7	9.97	1.13	7.3
Total c	15.08	3.50	3.17	46.19	5257.3	84.8	10.8	0.3	
Conc.(/g)	3229	748.5	679.2	9890	1.126E+6				

Table 2. Laser step-heating data.

Power[a]	$^{36}Ar_{tr}$	$^{37}Ar_{Ca}$	$^{38}Ar_{Cl}$	$^{39}Ar_{K}$	^{40}Ar	%Atmos	Apparent Age	^{39}Ar
(W)	x10^{-11}cm^3 STP[b]					^{40}Ar	Ma±2s[c]	(%)
MD-12-HBLD. J = .000485								
Aliquot A								
5	0.02	0.071	0.002	0.009	6.74	88.5	75.4 ± 171.9	0
10	0.01	1.392	0.084	0.144	7.05	43.8	23.9 ± 0.9	0.5
15	0.008	5.998	0.527	0.653	12.4	18.6	13.5 ± 0.2	2.1
20	0.008	5.325	0.369	0.538	10.13	23.9	12.5 ± 0.6	1.7
25	0.019	4.845	0.371	0.531	13.34	42.4	12.6 ± 0.3	1.7
30	0.005	5.294	0.475	0.564	9.38	14.9	12.4 ± 0.4	1.8
35	0.007	4.485	0.302	0.445	8.31	23.5	12.5 ± 0.6	1.4
40	0.003	2.072	0.188	0.23	4.17	22.8	12.2 ± 0.3	0.7
45	0.003	3.117	0.256	0.315	5.17	16.3	12 ± 0.3	1
Aliquot B								
5	0.024	0.115	0.003	0.014	8.32	86	73.5 ± 65 .8	0
10	0.023	0.529	0.042	0.077	8.77	76.9	23 ± 4.7	0.2
15	0.063	7.356	0.545	0.776	30.98	60.5	13.7 ± 0.5	2.4
20	0.036	8.7	0.579	0.922	26.5	40	15 ± 0.3	2.9
25	0.017	7.258	0.569	0.777	16.98	28.8	13.5 ± 0.5	2.4
30	0.018	10.856	0.836	1.126	21.35	25.1	12.4 ± 0.4	3.5
35	0.009	5.721	0.392	0.6	11.34	24.4	12.5 ± 0.7	1.9
45	0.029	14.494	1.018	1.452	28.22	30.2	11.8 ± 0.3	4.6
Aliquot C								
5	0.028	0.128	0.006	0.013	9.15	89.7	63.7 ± 30.7	0
10	0.026	0.435	0.04	0.054	9.23	83.5	24.6 ± 15.2	0.2
15	0.104	5.367	0.456	0.61	41.93	73.5	15.8 ± 1.5	1.9
20	0.037	9.224	0.821	1.05	26.19	41.3	12.8 ± 0.3	3.3
25	0.022	7.528	0.692	0.86	20.43	31.3	14.2 ± 0.6	2.7
30	0.025	10.717	0.905	1.128	23.54	31	12.6 ± 0.6	3.5
35	0.023	8.643	0.705	0.913	20.02	33.6	12.7 ± 0.5	2.9
45	0.023	14.194	0.991	1.461	27.64	24.8	12.4 ± 0.3	4.6
Aliquot D								
5	0.027	0.073	0.01	0.031	8.85	91.6	20.9 ± 10.2	0.1
10	0.025	0.954	0.075	0.104	9.27	78.3	16.8 ± 2.4	0.3
15	0.057	11.644	0.997	1.287	37.34	45	13.9 ± 0.5	4
20	0.02	12.171	0.78	1.233	24.06	25.1	12.8 ± 0.3	3.9
25	0.013	9.509	0.669	1.002	18.59	21.2	12.7 ± 0.5	3.2
30	0.01	8.327	0.494	0.799	14.41	19.6	12.6 ± 0.3	2.5
35	0.022	17.002	1.181	1.821	32.09	20	12.3 ± 0.4	5.7
45	0.023	20.403	1.423	2.146	37.48	18.3	12.4 ± 0.2	6.7
Aliquot E								
5	0.046	0.148	0.002	0.023	14.06	96.2	19.9 ± 30.4	0.1
10	0.04	1.665	0.124	0.208	15.47	76.2	15.4 ± 1.7	0.7
15	0.056	10.582	0.725	1.173	35.59	46.4	14.2 ± 0.5	3.7
20	0.022	11.705	1.007	1.293	25.39	25.6	12.7 ± 0.4	4.1
25	0.015	11.923	0.767	1.296	23.64	19.1	12.9 ± 0.6	4.1
30	0.02	14.528	1.03	1.506	27.72	21	12.7 ± 0.4	4.7
35	0.016	7.925	0.568	0.803	15.94	29.8	12.1 ± 0.6	2.5
45	0.019	17.537	1.199	1.815	31.06	17.9	12.3 ± 0.2	5.7
Total[d]	**1.02**	**299.96**	**22.23**	**31.80**	**778.2**	**38.7**	**13.1 ± 0.2**	

[a] Nominal power as measured by laser, prior to 20x attenuation of beam

[b] Gas quantities corrected for decay and isotopes derived from interfering neutron reactions

[c] Errors are analytical only and do not include error in irradiation factor J

[d] Integrated age, uncertainty includes error in J (0.5% at 1 sigma)

Power[a]	$^{36}Ar_{tr}$	$^{37}Ar_{Ca}$	$^{38}Ar_{Cl}$	$^{39}Ar_{K}$	^{40}Ar	%Atmos	Apparent Age	^{39}Ar
(W)	x10^{-11}cm^3 STP[b]					^{40}Ar	Ma±2s[c]	(%)
MD-13-HBLD. J = .000485								
Aliquot A								
5	0.031	0.286	0.031	0.097	10.36	88.1	11.1 ± 1.3	0.2
10	0.029	3.013	0.301	0.421	13.51	63.3	10.3 ± 0.9	0.7
15	0.037	8.101	0.81	1.093	22.86	48.1	9.47 ± 0.21	1.8
20	0.031	7.014	0.687	0.899	19.29	47.9	9.75 ± 0.39	1.5
25	0.018	5.187	0.48	0.654	12.62	42.9	9.62 ± 0.38	1.1
30	0.013	4.806	0.439	0.571	10.39	37.5	9.93 ± 0.3	0.9
35	0.019	5.177	0.48	0.643	12.75	43.3	9.8 ± 0.2	1
40	0.012	7.895	0.807	1.031	15.19	23.3	9.86 ± 0.26	1.7
45	0.016	10.279	1.03	1.292	19.17	24.5	9.77 ± 0.35	2.1
Aliquot B								
5	0.054	0.119	0.005	0.007	16.23	98.9	21.6 ± 684.1	0
10	0.077	4.719	0.466	0.625	30.47	74.8	10.7 ± 0.6	1
15	0.084	18.157	1.776	2.405	51.7	47.9	9.76 ± 0.11	3.9
20	0.029	12.849	1.246	1.654	27.34	30.8	9.97 ± 0.19	2.7
25	0.031	9.709	0.937	1.245	23.08	39.6	9.77 ± 0.36	2
30	0.036	14.845	1.484	1.937	32.74	32.7	9.92 ± 0.22	3.1
35	0.022	10.642	1.065	1.399	22.05	29.4	9.7 ± 0.27	2.3
40	0.026	17.387	1.719	2.194	31.6	24.1	9.54 ± 0.28	3.5
45	0.021	11.916	1.227	1.476	21.62	28.9	9.09 ± 0.26	2.4
Aliquot C								
5	0.066	0.19	0.005	0.02	19.22	101.8	-14.78 ± 38.38	0
10	0.059	2.474	0.237	0.329	22.27	78.3	12.8 ± 0.9	0.5
15	0.097	17.697	1.666	2.258	55.2	51.9	10.3 ± 0.3	3.6
20	0.064	16.939	1.663	2.171	42.52	44.8	9.43 ± 0.28	3.5
25	0.047	17.076	1.697	2.189	38.41	35.9	9.82 ± 0.29	3.5
30	0.042	17.375	1.696	2.152	36.5	33.7	9.82 ± 0.26	3.5
35	0.025	14.933	1.502	1.88	28.08	26.8	9.53 ± 0.21	3
40	0.028	16.598	1.667	2.134	31.9	25.7	9.69 ± 0.18	3.4
45	0.019	7.304	0.761	0.901	15.18	36.9	9.28 ± 0.38	1.5
Aliquot D								
5	0.046	0.101	0.002	0.018	15.85	85.3	111.2 ± 23.7	0
10	0.057	3.585	0.334	0.447	22.65	73.9	11.5 ± 0.9	0.7
15	0.091	17.696	1.705	2.266	52.65	51.3	9.87 ± 0.16	3.7
20	0.056	14.455	1.388	1.814	37.01	44.5	9.88 ± 0.25	2.9
25	0.043	11.62	1.12	1.458	28.32	44.7	9.38 ± 0.13	2.4
30	0.045	14.105	1.413	1.827	33.37	39.7	9.61 ± 0.25	3
35	0.036	16.683	1.67	2.159	35.19	30.1	9.95 ± 0.19	3.5
40	0.026	19.887	1.956	2.497	36.21	21.4	9.94 ± 0.14	4
45	0.02	12.486	1.285	1.589	23.35	25.7	9.53 ± 0.16	2.6
Aliquot E								
5	0.064	0.237	0.01	0.032	20.01	94.7	28.5 ± 22.9	0.1
10	0.053	4.312	0.428	0.571	23.72	66.6	12.1 ± 0.7	0.9
15	0.1	20.347	1.982	2.603	59.6	49.8	10 ± 0.4	4.2
20	0.08	19.649	1.865	2.474	50.25	46.9	9.41 ± 0.4	4
25	0.056	13.474	1.302	1.688	34.65	47.7	9.37 ± 0.28	2.7
30	0.045	14.946	1.472	1.885	33.29	39.6	9.31 ± 0.21	3
35	0.028	13.053	1.304	1.651	26.11	31.2	9.49 ± 0.18	2.7
40	0.017	10.362	1.069	1.349	19.46	25.3	9.39 ± 0.24	2.2
45	0.02	15.725	1.571	1.924	26.99	21.4	9.62 ± 0.18	3.1
Total[d]	**0.02**	**4.85**	**0.48**	**0.62**	**1260.9**	**44.9**	**9.80 ± 0.1**	

Table 2. (cont.)

Power[a]	$^{36}Ar_{tr}$	$^{37}Ar_{Ca}$	$^{38}Ar_{Cl}$	$^{39}Ar_{K}$	^{40}Ar	%Atmos	Apparent Age	^{39}Ar
(W)	$x10^{-11}cm^3$ STP[b]					^{40}Ar	Ma±2s[c]	(%)
M6-HBLD. J = .000485								
Aliquot A								
5	0.03	0.111	0.006	0.018	8.78	100.8	-3.67 ± 28.97	0.1
10	0.013	4.086	0.203	0.367	7.91	46.9	9.99 ± 0.86	1.5
15	0.01	9.182	0.433	0.84	12.37	24.5	9.7 ± 0.36	3.4
20	0.007	4.586	0.213	0.429	6.72	31.9	9.3 ± 0.36	1.8
25	0.005	1.664	0.073	0.159	3.25	45	9.77 ± 1.51	0.7
30	0.005	1.237	0.056	0.094	2.56	58	9.92 ± 3.78	0.4
35	0.006	0.674	0.035	0.064	1.98	82.5	4.74 ± 2.91	0.3
45	0.005	1.117	0.056	0.098	2.4	60.5	8.41 ± 2.52	0.4
Aliquot B								
5	0.069	0.202	0.012	0.079	21.36	95	11.8 ± 6	0.3
10	0.076	5.47	0.27	0.506	28.91	77.8	11.1 ± 0.7	2.1
15	0.086	20.606	0.981	1.837	47.6	53.6	10.5 ± 0.2	7.5
20	0.036	17.241	0.821	1.523	28.39	37.9	10.1 ± 0.2	6.2
30	0.031	28.071	1.336	2.457	38.4	23.9	10.4 ± 0.3	10
45	0.028	34.148	1.621	3.003	42.65	19.2	10 ± 0.2	12.3
Aliquot C								
15	0.058	3.907	0.227	0.492	22.12	77	9.01 ± 0.79	2
20	0.037	4.723	0.229	0.442	16.09	67.9	10.2 ± 0.6	1.8
25	0.034	6.221	0.291	0.546	15.9	62.6	9.51 ± 0.48	2.2
30	0.042	8.236	0.396	0.724	22.23	55.6	11.9 ± 1	3
35	0.03	9.498	0.428	0.805	18.69	48	10.5 ± 0.4	3.3
45	0.027	15.29	0.724	1.357	23.51	33.7	10 ± 0.3	5.5
50	0.018	11.277	0.52	0.939	16.67	32.8	10.4 ± 0.3	3.8
55	0.016	14.112	0.663	1.229	20.49	23.8	11.1 ± 0.3	5
60	0.012	15.361	0.725	1.357	19.43	18.4	10.2 ± 0.1	5.5
Aliquot D								
20	0.023	4.515	0.217	0.432	12.35	55.2	11.2 ± 0.5	1.8
25	0.051	11.551	0.558	1.104	28.35	52.8	10.6 ± 0.4	4.5
30	0.026	12.361	0.547	1.124	21.51	36	10.7 ± 0.3	4.6
35	0.019	8.374	0.376	0.789	15.28	37.2	10.6 ± 0.4	3.2
40	0.018	10.883	0.507	1.011	17.17	31.1	10.2 ± 0.2	4.1
45	0.008	7.592	0.344	0.647	10.5	22.5	11 ± 0.1	2.6
Total[d]	**0.83**	**272.30**	**12.87**	**24.48**	**533.5**	**45.8**	**10.3 ± 0.1**	
MD-15-HBLD. J = .000485								
Aliquot A								
5	0.076	0.381	0.003	0.037	24.13	93.1	38.8 ± 20.8	0.1
10	0.058	2.712	0.347	0.353	21.74	78.4	11.6 ± 0.8	1.4
15	0.085	8.665	1.209	1.275	39.33	64.2	9.64 ± 0.36	4.9
20	0.038	4.596	0.529	0.625	18.41	61.1	10 ± 0.53	2.4
25	0.022	3.706	0.404	0.459	11.56	57.1	9.43 ± 0.72	1.8
30	0.009	3.529	0.457	0.417	7.39	37	9.74 ± 0.63	1.6
35	0.01	4.794	0.629	0.67	10.07	28	9.45 ± 0.27	2.6
45	0.011	6.991	0.941	0.929	13.6	24.6	9.64 ± 0.12	3.6
Aliquot B								
5	0.083	0.642	0.016	0.086	26.06	93.8	16.2 ± 17.7	0.3
10	0.035	1.807	0.269	0.299	14.68	71.1	12.3 ± 1	1.2
15	0.107	8.891	1.293	1.428	47.4	66.5	9.7 ± 0.77	5.5
20	0.054	4.38	0.578	0.688	23.67	66.8	9.96 ± 0.66	2.7
MD-15-HBLD. J = .000485 (cont.)								
Aliquot B								
30	0.03	6.906	0.92	1.031	20.07	43.6	9.59 ± 0.4	4
40	0.021	9.144	1.29	1.437	21.62	28.2	9.43 ± 0.26	5.5
45	0.012	6.582	0.959	0.955	13.98	25.8	9.47 ± 0.31	3.7
Aliquot C								
5	0.063	0.713	0.024	0.06	20.14	92.5	21.9 ± 18.8	0.2
10	0.045	2.661	0.293	0.308	16.98	78.7	10.2 ± 1.3	1.2
15	0.068	6.202	0.962	0.961	30.6	65.8	9.49 ± 0.49	3.7
20	0.042	4.744	0.641	0.589	18.82	66	9.47 ± 0.18	2.3
30	0.035	4.762	0.728	0.697	17.79	57.6	9.44 ± 0.67	2.7
40	0.038	9.35	1.423	1.391	25.99	42.7	9.34 ± 0.29	5.4
45	0.012	5.773	0.863	0.758	11.95	30.8	9.52 ± 0.37	2.9
Aliquot D								
5	0.079	0.747	0.016	0.038	24.23	95.8	23.3 ± 38.6	0.1
10	0.082	1.875	0.287	0.292	27.47	88.4	9.56 ± 1.6	1.1
15	0.06	7.481	1.148	1.092	29.67	59.6	9.57 ± 0.3	4.2
20	0.044	5.756	0.836	0.824	22.18	58.5	9.73 ± 0.47	3.2
30	0.046	7.585	1.094	1.051	25.04	54	9.57 ± 0.41	4
40	0.062	11.767	1.689	1.571	34.96	52.4	9.24 ± 0.22	6.1
45	0.06	5.828	0.875	0.856	26.98	65.9	9.37 ± 0.56	3.3
Aliquot E								
5	0.077	0.955	0.052	0.091	24.76	92.4	18 ± 3.9	0.3
10	0.052	3.547	0.4	0.418	19.8	77.8	9.15 ± 1.23	1.6
15	0.064	7.821	1.152	1.174	31.42	60.3	9.28 ± 0.34	4.5
20	0.029	3.922	0.506	0.519	14.26	60	9.58 ± 0.25	2
30	0.046	9.893	1.338	1.314	28.06	48.9	9.52 ± 0.42	5.1
40	0.035	7.384	1.129	1.047	22.29	46.8	9.88 ± 0.3	4
45	0.013	1.499	0.19	0.221	6.42	61.4	9.81 ± 0.99	0.8
Total[d]	**0.02**	**1.84**	**0.25**	**0.26**	**793.5**	**63.4**	**9.75 ± 0.2**	
MD-15-BIOT J = .000489								
Aliquot A								
3	0.118	0.032	0.08	0.569	38.19	91.3	5.12 ± 0.74	0.4
5	0.161	0.045	0.146	1.181	55.93	85.1	6.22 ± 0.42	0.7
10	0.321	0.062	0.409	3.458	125.11	75.8	7.7 ± 0.25	2.1
20	0.461	0.125	0.884	7.405	209.13	65.1	8.66 ± 0.14	4.6
45	0.221	0.268	1.676	13.65	194.89	33.5	8.35 ± 0.05	8.5
Aliquot B								
3	0.245	0.03	0.106	0.738	76.92	94.2	5.34 ± 1.82	0.5
5	0.198	0.054	0.176	1.352	70.54	83.1	7.75 ± 0.68	0.8
10	0.234	0.06	0.457	3.733	106.21	65.1	8.75 ± 0.24	2.3
20	0.306	0.18	0.944	7.637	166.52	54.3	8.76 ± 0.16	4.7
30	0.172	0.505	0.523	3.379	84.08	60.4	8.68 ± 0.25	2.1
45	0.09	0.324	0.185	0.676	33.63	79.3	9.07 ± 0.51	0.4
Aliquot C								
3	0.175	0.014	0.094	0.723	55.45	93.2	4.6 ± 1.3	0.4
5	0.215	0.06	0.191	1.607	75.55	84.1	6.6 ± 0.47	1
10	0.348	0.08	0.494	3.921	138.1	74.4	7.95 ± 0.33	2.4
20	0.486	0.142	0.915	7.362	220.66	65	9.22 ± 0.17	4.6
45	0.204	0.256	0.348	2.27	82.84	72.6	8.79 ± 0.29	1.4
Aliquot D								
3	0.214	0.055	0.117	0.84	65.64	96.2	2.65 ± 1.09	0.5
5	0.195	0.062	0.155	1.271	66.92	86.2	6.39 ± 0.46	0.8

[a] Nominal power as measured by laser, prior to 20x attenuation of beam
[b] Gas quantities corrected for decay and isotopes derived from interfering neutron reactions
[c] Errors are analytical only and do not include error in irradiation factor J
[d] Integrated age, uncertainty includes error in J (0.5% at 1 sigma)

Table 2. (cont.)

Power[a]	$^{36}Ar_{tr}$	$^{37}Ar_{Ca}$	$^{38}Ar_{Cl}$	$^{39}Ar_{K}$	^{40}Ar	%Atmos	Apparent Age	^{39}Ar
(W)	x10^{-11}cm^3 STP[b]					^{40}Ar	Ma±2s[c]	(%)
MD-15-BIOT J = .000489 (cont.)								
Aliquot D								
10	0.347	0.108	0.451	3.587	135.05	75.9	7.99 ± 0.14	2.2
20	0.699	0.333	1.419	10.362	312.17	66.1	8.98 ± 0.09	6.4
45	0.464	0.604	1.772	14.052	277.68	49.4	8.8 ± 0.09	8.7
Aliquot E								
3	0.259	0.057	0.129	0.912	82.09	93.4	5.25 ± 0.99	0.6
5	0.426	0.081	0.323	2.282	141.73	88.8	6.15 ± 0.95	1.4
10	0.382	0.051	0.395	2.99	140.78	80.2	8.19 ± 0.31	1.9
20	0.783	0.174	1.073	8.035	306.05	75.6	8.17 ± 0.19	5
45	1.42	0.418	2.639	20.278	620.1	67.7	8.71 ± 0.14	12.6
Aliquot F								
3	0.132	0.065	0.066	0.484	41.85	93	5.31 ± 0.26	0.3
5	0.192	0.061	0.168	1.339	66.6	85.1	6.54 ± 0.61	0.8
10	0.225	0.066	0.349	2.944	92.68	71.8	7.81 ± 0.31	1.8
20	0.471	0.142	1.074	8.891	227.03	61.3	8.7 ± 0.14	5.5
45	0.577	0.515	1.94	16.411	327.52	52	8.42 ± 0.11	10.2
Aliquot G								
3	0.14	0.054	0.09	0.766	47.16	87.4	6.8 ± 1.1	0.5
5	0.127	0.074	0.193	1.567	52.77	71.3	8.51 ± 0.29	1
10	0.127	0.062	0.252	2.139	58.21	64.4	8.51 ± 0.28	1.3
20	0.091	0.134	0.211	1.552	42.63	63.2	8.9 ± 0.54	1
45	0.04	0.137	0.092	0.548	16.94	68.9	8.46 ± 0.59	0.3
Total[d]	**0.11**	**0.05**	**0.21**	**1.61**	**4855.4**	**68.6**	**8.35 ± 0.1**	
MD5-HBLD. J = .000485								
Aliquot A								
5	0.023	0.32	0.004	0.003	7.21	94.2	136.2 ±1356.4	0
10	0.023	2.127	0.246	0.236	9.82	68.6	11.4 ± 1.3	0.8
15	0.022	7.822	1.245	1.141	17.87	36.7	8.65 ± 0.21	4.1
20	0.013	4.846	0.804	0.694	10.41	36	8.39 ± 0.17	2.5
25	0.008	4.065	0.562	0.54	7.48	31	8.34 ± 0.18	1.9
30	0.007	5.129	0.708	0.711	8.77	23.8	8.2 ± 0.16	2.5
35	0.009	4.8	0.669	0.615	8.36	32.1	8.06 ± 0.25	2.2
40	0.011	8.239	1.182	1.174	14.32	22.2	8.29 ± 0.08	4.2
45	0.011	8.689	1.108	1.143	14.49	22.5	8.58 ± 0.22	4.1
Aliquot B								
5	0.012	0.584	0.005	0.011	4.59	78.6	79 ± 106.3	0
10	0.021	2.35	0.269	0.258	8.97	68.3	9.62 ± 0.68	0.9
15	0.019	7.242	1.178	1.065	16.56	34.5	8.89 ± 0.31	3.8
25	0.014	6.955	1.104	0.986	14.55	29.4	9.09 ± 0.26	3.5
35	0.012	9.512	1.342	1.278	16.35	21.9	8.72 ± 0.25	4.6
40	0.012	7.361	0.999	0.983	13.31	27.3	8.59 ± 0.16	3.5
45	0.01	7.089	1.024	0.963	12.45	24	8.59 ± 0.21	3.4
Aliquot C								
5	0.024	0.692	0.007	0.029	6.91	101.8	-3.7 ± 20.63	0.1
10	0.018	1.784	0.237	0.24	8.62	62.7	11.7 ± 1.2	0.9
15	0.038	7.478	1.038	0.966	21.04	54	8.74 ± 0.6	3.5
25	0.027	7.368	1.033	1.05	18.4	43.2	8.69 ± 0.13	3.8
35	0.041	11.041	1.592	1.462	26.44	45.8	8.55 ± 0.13	5.2
40	0.014	9.25	1.352	1.256	17.16	24.6	8.99 ± 0.14	4.5
45	0.011	6.248	0.861	0.849	12.19	25.8	9.3 ± 0.36	3
MD5-HBLD. J = .000485 (cont.)								
Aliquot D								
5	0.019	0.792	0.013	0.021	6.6	86.4	37 ± 9.6	0.1
10	0.02	3.674	0.405	0.41	11.07	52.1	11.3 ± 0.4	1.5
15	0.025	9.268	1.172	1.219	20.86	35.5	9.63 ± 0.23	4.4
25	0.022	7.027	1.044	1.007	16.74	38.5	8.92 ± 0.28	3.6
35	0.016	6.795	0.973	0.935	14.46	32.2	9.16 ± 0.11	3.3
40	0.016	8.918	1.14	1.142	16.81	28.9	9.13 ± 0.31	4.1
45	0.011	7.888	1.142	1.135	15.11	22.3	9.04 ± 0.24	4.1
Aliquot E								
5	0.015	0.365	0.01	0.03	4.66	96.3	5.12 ± 10.83	0.1
10	0.016	1.979	0.2	0.199	6.88	68.8	9.42 ± 1.14	0.7
15	0.031	8.977	1.384	1.288	21.95	41.8	8.66 ± 0.16	4.6
20	0.015	4.351	0.518	0.489	9.45	47.7	8.82 ± 0.34	1.7
25	0.008	2.606	0.276	0.256	5.06	49.4	8.74 ± 0.44	0.9
35	0.014	5.303	0.751	0.78	11.67	36.6	8.27 ± 0.19	2.8
40	0.027	6.334	0.998	0.974	17.49	46.3	8.42 ± 0.33	3.5
45	0.012	3.567	0.476	0.445	7.66	45.2	8.23 ± 0.26	1.6
Total[c]	**0.01**	**2.09**	**0.29**	**0.28**	**482.7**	**41.0**	**8.89 ± 0.2**	
MD8-BIOT J = .0004885								
Aliquot A								
5	0.911	0.061	0.212	1.417	271.24	99.3	1.26 ± 1.19	5.1
20	0.45	0.197	0.584	4.648	134.04	99.2	0.21 ± 0.13	16.8
40	0.036	0.038	0.092	0.76	10.94	96.7	0.42 ± 0.41	2.7
Aliquot B								
5	1.109	0.07	0.19	1.269	329.26	99.5	1.15 ± 2.07	4.6
20	0.61	0.219	0.501	3.553	181.31	99.5	0.24 ± 0.27	12.8
40	0.102	0.082	0.137	0.906	30.44	99.1	0.27 ± 0.11	3.3
Aliquot C								
5	2.357	0.11	0.281	1.514	698.94	99.6	1.46 ± 3.66	5.5
40	0.224	0.102	0.2	1.335	67.29	98.2	0.81 ± 0.38	4.8
3	1.414	0.261	0.167	0.909	419.41	99.6	1.5 ± 6.79	3.3
Aliquot D								
5	0.745	0.449	0.244	1.432	221.78	99.3	0.94 ± 1.62	5.2
10	1.271	0.12	0.381	2.88	376.17	99.8	0.18 ± 1.32	10.4
20	0.713	0.134	0.444	3.286	212.29	99.3	0.41 ± 0.61	11.9
25	0.172	0.108	0.243	1.85	52.49	96.7	0.82 ± 0.61	6.7
35	0.107	0.054	0.17	1.256	31.85	99.1	0.19 ± 0.46	4.5
45	0.054	0.133	0.106	0.655	16.25	98.5	0.33 ± 0.81	2.4
Total[d]	**0.10**	**0.02**	**0.04**	**0.28**	**3053.7**	**99.4**	**0.56 ± 0.4**	
M9-GLASS J = .000485								
Aliquot A								
5	0.037	0.318	0.69	2.744	12.95	84.3	0.65 ± 0.09	2.5
7	0.055	0.516	1.535	5.88	18.82	85.8	0.4 ± 0.03	5.4
10	0.031	0.51	1.103	4.202	11.32	81	0.45 ± 0.02	3.8
15	0.025	0.355	0.841	3.239	8.76	83.8	0.38 ± 0.08	3
20	0.009	0.109	0.207	0.823	2.92	86.6	0.41 ± 0.1	0.8
45	0.005	0.187	0.065	0.28	1.72	88	0.65 ± 0.79	0.3
Aliquot B								
3	0.024	0.161	0.279	1.138	7.48	94.9	0.3 ± 0.12	1
4	0.049	0.407	1.048	4.183	15.98	91.4	0.29 ± 0.08	3.8
5	0.031	0.444	0.707	2.801	10.14	89.5	0.33 ± 0.06	2.6

[a] Nominal power as measured by laser, prior to 20x attenuation of beam
[b] Gas quantities corrected for decay and isotopes derived from interfering neutron reactions
[c] Errors are analytical only and do not include error in irradiation factor J
[d] Integrated age, uncertainty includes error in J (0.5% at 1 sigma)

Table 2. (cont.)

Power[a]	$^{36}Ar_{tr}$	$^{37}Ar_{Ca}$	$^{38}Ar_{Cl}$	$^{39}Ar_{K}$	^{40}Ar	%Atmos	Apparent Age	^{39}Ar
(W)	$x10^{-11}cm^3$ STP[b]					^{40}Ar	Ma±2s[c]	(%)
M9-GLASS J = .000485 (cont.)								
Aliquot B								
6	0.014	0.169	0.217	0.836	4.36	93.1	0.32 ± 0.43	0.8
8	0.014	0.225	0.238	0.948	4.55	92.4	0.32 ± 0.29	0.9
10	0.029	0.322	0.649	2.424	9.88	86.8	0.47 ± 0.16	2.2
15	0.043	0.328	1.332	5.115	14.49	86.8	0.33 ± 0.03	4.7
45	0.06	0.767	2.563	9.654	22.07	80.8	0.38 ± 0.03	8.8
Aliquot C								
2	0.003	0.045	0.003	0.015	0.88	86	7.25 ± 13.51	0
3	0.053	0.424	1.151	4.472	17.6	88.8	0.39 ± 0.04	4.1
4	0.051	0.302	0.741	2.851	16.37	91.5	0.43 ± 0.09	2.6
5	0.038	0.411	0.871	3.471	12.62	89.6	0.33 ± 0.07	3.2
6	0.017	0.129	0.276	1.05	5.48	91.8	0.38 ± 0.24	1
10	0.039	0.401	0.988	3.834	12.75	90.3	0.28 ± 0.04	3.5
15	0.034	0.452	1.156	4.373	12.16	82.2	0.43 ± 0.1	4
20	0.029	0.433	1.138	4.337	10.97	79.3	0.46 ± 0.1	4
45	0.016	0.26	0.552	2.104	6.02	79.2	0.52 ± 0.06	1.9
Aliquot D								
2	0.001	0.091	0.002	0.005	0.62	56.9	47.8 ± 55.3	0
3	0.014	0.176	0.135	0.55	4.14	96.9	0.2 ± 0.21	0.5
4	0.025	0.273	0.52	2.023	7.88	91.9	0.28 ± 0.06	1.8
5	0.035	0.304	0.685	2.668	11.09	93.5	0.24 ± 0.06	2.4
6	0.01	0.169	0.215	0.809	3.02	93.2	0.22 ± 0.05	0.7
10	0.046	0.246	0.476	1.894	14.59	92.8	0.49 ± 0.17	1.7
15	0.082	0.799	2.268	8.658	28.46	85	0.43 ± 0.03	7.9
20	0.019	0.26	0.581	2.232	6.76	82.1	0.47 ± 0.13	2
45	0.014	0.197	0.367	1.409	4.53	88.3	0.33 ± 0.06	1.3
Aliquot E								
2	0.002	0.123	0.004	0.012	0.69	88.5	5.75 ± 12.79	0
3	0.014	0.163	0.158	0.632	4.36	92.4	0.46 ± 0.49	0.6
4	0.017	0.176	0.261	1.039	5.32	92.3	0.35 ± 0.13	0.9
5	0.02	0.32	0.478	1.852	6.38	91.4	0.26 ± 0.06	1.7
6	0.009	0.162	0.19	0.719	2.86	96.3	0.13± 0.09	0.7
10	0.015	0.186	0.204	0.811	4.5	97.8	0.11 ± 0.14	0.7
15	0.037	0.348	0.92	3.541	12.63	86.9	0.41 ± 0.05	3.2
20	0.031	0.313	0.684	2.653	10.47	87.6	0.43 ± 0.06	2.4
45	0.063	0.643	1.934	7.324	22.46	83.5	0.44 ± 0.04	6.7
Total[d]	**0.01**	**0.13**	**0.28**	**1.1**	**391**	**87.4**	**0.39 ± 0**	
M9-BIOT. J = .000485								
Aliquot A								
3	0.17	0.02	0.295	1.009	51.17	98.4	0.69 ± 0.63	2.7
5	0.067	0.039	0.197	1.052	20.39	97.3	0.45 ± 0.31	2.8
10	0.101	0.069	0.311	2.01	30.85	96.8	0.43 ± 0.17	5.4
20	0.088	0.094	0.33	2.575	26.51	97.6	0.21 ± 0.1	6.9
30	0.011	0.014	0.032	0.232	3.56	89.2	1.45 ± 0.83	0.6
45	0.006	0.015	0.013	0.09	1.75	99.2	0.13 ± 1.12	0.2
Aliquot B								
3	0.303	0.088	0.394	0.958	89.61	99.9	0.1 ± 1.41	2.6
5	0.111	0.056	0.308	1.398	33.82	96.6	0.72 ± 0.31	3.7
10	0.084	0.076	0.233	1.45	25.16	98.4	0.24 ± 0.19	3.9
20	0.133	0.137	0.495	3.517	42.91	91.3	0.93 ± 0.26	9.4
45	0.039	0.063	0.146	1.177	12.02	96.8	0.28 ± 0.16	3.2
Aliquot C								
3	0.129	0.018	0.248	0.743	38.55	98.7	0.59 ± 0.59	2
5	0.034	0.037	0.102	0.629	9.95	99.6	0.05 ± 0.3	1.7
10	0.032	0.053	0.107	0.706	9.81	97.7	0.28 ± 0.28	1.9
20	0.049	0.046	0.128	0.841	14.73	97.5	0.39 ± 0.37	2.3
45	0.011	0.055	0.034	0.214	3.71	90.8	1.39 ± 1.12	0.6
Aliquot D								
3	0.372	0.082	0.428	1.736	110.9	99.2	0.43 ± 1.05	4.7
5	0.198	0.098	0.421	2.325	60.06	97.6	0.53 ± 0.31	6.2
10	0.25	0.159	0.657	3.709	74.9	98.8	0.21 ± 0.09	9.9
20	0.336	0.29	0.939	6.219	102.53	96.9	0.44 ± 0.19	16.7
30	0.153	0.166	0.574	3.984	47.05	96.4	0.37 ± 0.12	10.7
45	0.033	0.064	0.1	0.726	10.56	93.3	0.85 ± 0.3	1.9
Total[d]	**0.03**	**0.02**	**0.06**	**0.37**	**820.5**	**97.6**	**0.45 ± 0.1**	

[a] Nominal power as measured by laser, prior to 20x attenuation of beam
[b] Gas quantities corrected for decay and isotopes derived from interfering neutron reactions
[c] Errors are analytical only and do not include error in irradiation factor J
[d] Integrated age, uncertainty includes error in J (0.5% at 1 sigma)

The gas released was cleaned by passive equilibration of the gas with three SAES NP-10 getters of ST707 alloy at 400° C and a cold getter of SAES alloy 201 pellets for two to five minutes. Purified gasses were analyzed with a VG3600 mass spectrometer, a magnetic sector mass spectrometer with 60° extended geometry equipped with a Faraday collector and electron multiplier on which the signal was measured across a 1 x 10^9 ohm resistor with a resulting gain, relative to Faraday, of approximately 50. Although multiplier sensitivity is gain dependent, it was estimated at 1.900 x 10^{-9} cm^3 STP/V. Isotopic ratios were corrected by online computer for mass fractionation, mass-spectrometer sensitivity, blanks, interference reactions from K and Ca, and decay since irradiation.

The final age determination includes the error in J factor measurement (± 0.5%) as outlined in Roddick (1988). The error on the age of the monitor is not included in the final error analysis. This study presents the results of thirteen age determinations from eight samples. Analytical results from laser analysis are shown in Table 2. Data from ^{40}Ar-^{39}Ar step-heating analysis are shown in age spectrum diagrams or correlation plots (Fig. 3). Additional details on procedure are provided in Villeneuve and MacIntyre (1997).

AGE DETERMINATIONS

Data from step-heating analyses are displayed in age spectrum diagrams or correlation plots and show the best estimated age derived from analytical results. In the age spectrum diagram of the sample processed using furnace step-heating, the apparent ^{40}Ar-^{39}Ar age of each heating step is plotted against the fraction of ^{39}Ar released over the entire experiment. In age spectrum diagrams of samples analyzed by the laser ^{40}Ar-^{39}Ar technique, the apparent ^{40}Ar-^{39}Ar age of each heating step is plotted against the cumulative amount of ^{39}Ar released, thus defining an age spectrum for each sample. Each sequential shaded background in the diagram

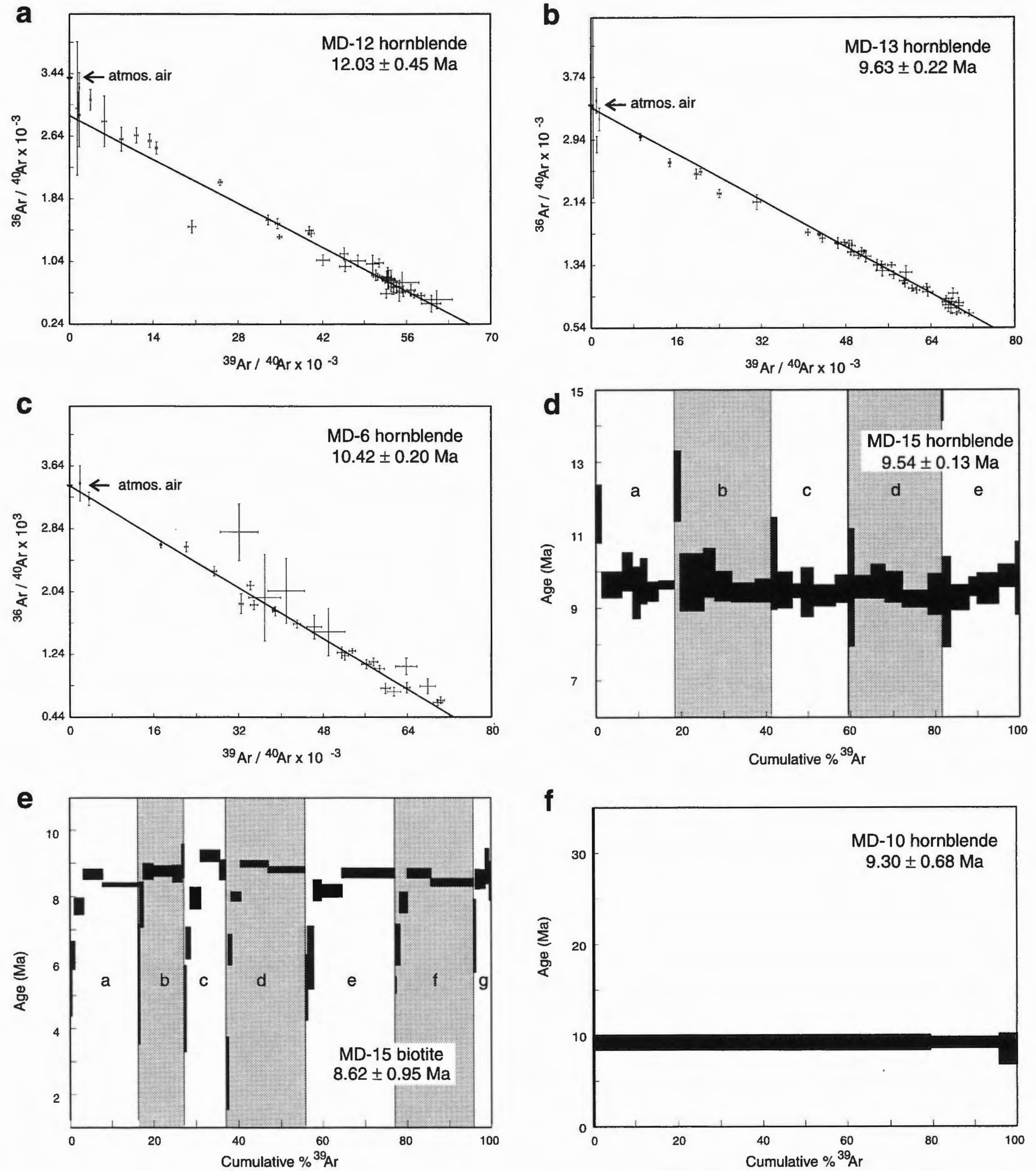

Figure 3. *Gas-release spectra and inverse isochrons for samples analyzed showing the best estimated age derived from analytical results. Alternating backgrounds in age-spectrum diagrams indicate different aliquots.*

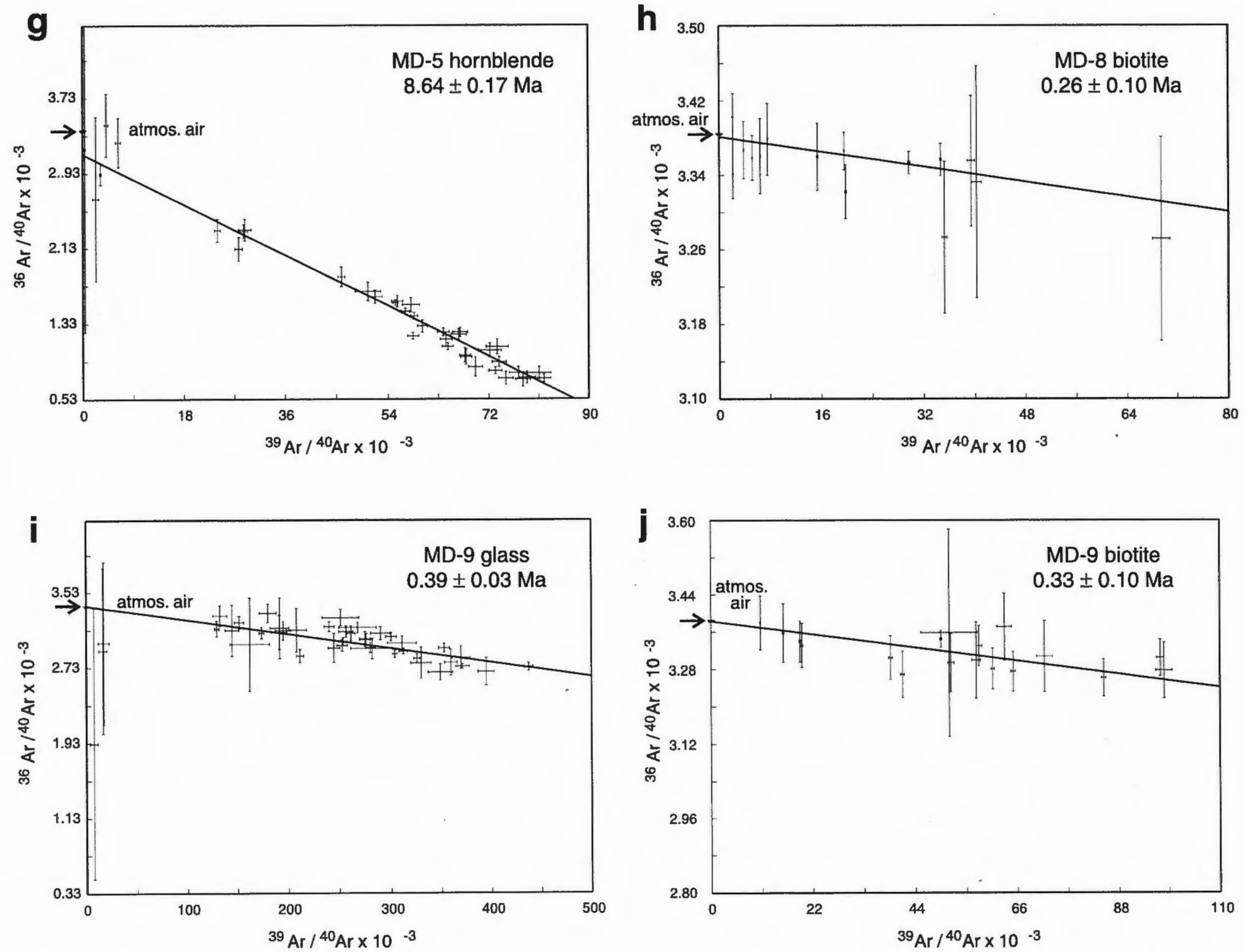

Figure 3. *(cont.)*

represents a single step-heated aliquot, normalized to the total volume of ^{39}Ar released for all aliquots. Plateau portions are combined, if acceptably reproducible, and treated as a single, step-heated analysis for data reduction. Alternatively, if there is no evidence of low-temperature argon loss, all data are plotted on an inverse isochron and age calculated by regression following York (1969).

Sample Md-12 was collected from a reworked tuff in the uppermost part of the Mariño Formation, Arroyo del Agua section (section II, Fig. 2a). In the study profile, the boundary between the Mariño and the overlying La Pilona formations was defined from field studies as the first appearance of a conglomerate bed whose characteristics are typical of the La Pilona Formation.

The age spectrum analysis of Md-12 hornblende displays a pattern of incremental release for each aliquot that defines a profile ascribable to the presence of excess ^{40}Ar. Laser ^{40}Ar/^{39}Ar analysis shown in the correlation plot (Fig. 3a) allows assessment of the composition of the trapped ^{40}Ar/^{36}Ar component. The regression line fitted through the 45 analyses defines an age of 12.03 ± 0.45 Ma from the intersection with the x-axis and a trapped ^{40}Ar/^{36}Ar value of 344.6 ± 18.0 from the intersection with the y-axis (mean standard weight of deviates [M.S.W.D.] = 22.5). The origin of the radiogenic trapped argon could be related to degassing of K-rich minerals and incorporation of excess ^{40}Ar in hornblendes under conditions of thermal disturbance of xenoliths or wall rocks of a magma chamber (*see* Harrison and McDougall, 1981).

Two samples collected from crystal-rich air-fall horizons near the middle part of the La Pilona Formation in the Arroyo del Agua Blanca (Md-13; section II, Fig. 2a) and La Higuerita (Md-6, White ash horizon; section III, Fig. 2a) sections yielded age constraints for this unit. The ^{40}Ar-^{39}Ar age spectrum of Md-13 hornblende displays a relatively flat profile for each aliquot with slight indications of excess ^{40}Ar in the small amounts of gas released in the first two steps on the correlation plot. Ignoring these steps and regressing through the most radiogenic steps (Fig. 3b) results in an atmospheric ^{40}Ar/^{36}Ar value of 298.0 ± 9.3 (M.S.W.D. = 6.2) and an age of 9.63 ± 0.22 Ma (~95% of the total gas). The good fit of the regression line and the essentially atmospheric intercept indicate that this portion of the gas has not been affected by excess ^{40}Ar. The first steps with anomalously high apparent ages probably reflect minor absorption of excess ^{40}Ar in less retentive sites of hornblende (*see* Harrison and McDougall, 1980).

The Md-6 hornblende was analyzed using laser step-heating (Fig. 3c). The correlation plot yields an age of 10.42 ± 0.20 Ma assuming a present-day atmospheric argon composition, with M.S.W.D. = 12.4. Data points with large errors (>1%) correspond to the small first aliquot containing the least amount of ^{39}Ar. Total fusion analyses performed on nine aliquots of Md-6 biotite yield an integrated age of 10.75 ± 0.29 Ma (Table 1). Hornblende and biotite ^{40}Ar-^{39}Ar ages are in agreement, yielding a weighted average age of 10.53 ± 0.16 Ma, which is considered to be the best age estimate for Md-6 tuff horizon.

Sample Md-15 was collected from a dark, crystal-rich air-fall horizon at the base of the Tobas Angostura unit in the Quebrada de la Angostura section (section V, Fig. 2b). The age spectrum for Md-15 hornblende (Fig. 3d) displays a well defined plateau for each aliquot, with each plateau defined by approximately six steps, which, when totaled, represent about 95% of the gas and yield an age of 9.54 ± 0.13 Ma. Age spectrum analysis of Md-15 biotite (Fig. 3e) shows a release pattern for each aliquot that defines a profile that can be ascribed to partial loss of radiogenic ^{40}Ar by thermal overprinting. The age spectrum of each aliquot is characterized by a low apparent age for the initial gas followed by a steep age gradient and then a flatter pattern, eventually producing a reasonably well defined plateau. In most cases, the first three lowest steps of each aliquot gave an apparent age younger than the flatter portion of the spectrum, which, when totalled, represent about 15–20% of the ^{39}Ar released. Only two aliquots (b, g) display well developed plateaus over four increments, whereas the rest exhibit flat release patterns only in the last two highest steps. Combining the 75–80% gas from the plateau portions of all aliquots yields a rather poorly defined age of 8.62 ± 0.95 Ma. Having evidence of loss of radiogenic ^{40}Ar in Md-15 biotite and thus a disturbed age spectrum, the hornblende age (9.54 ± 0.13 Ma) is interpreted to be the best

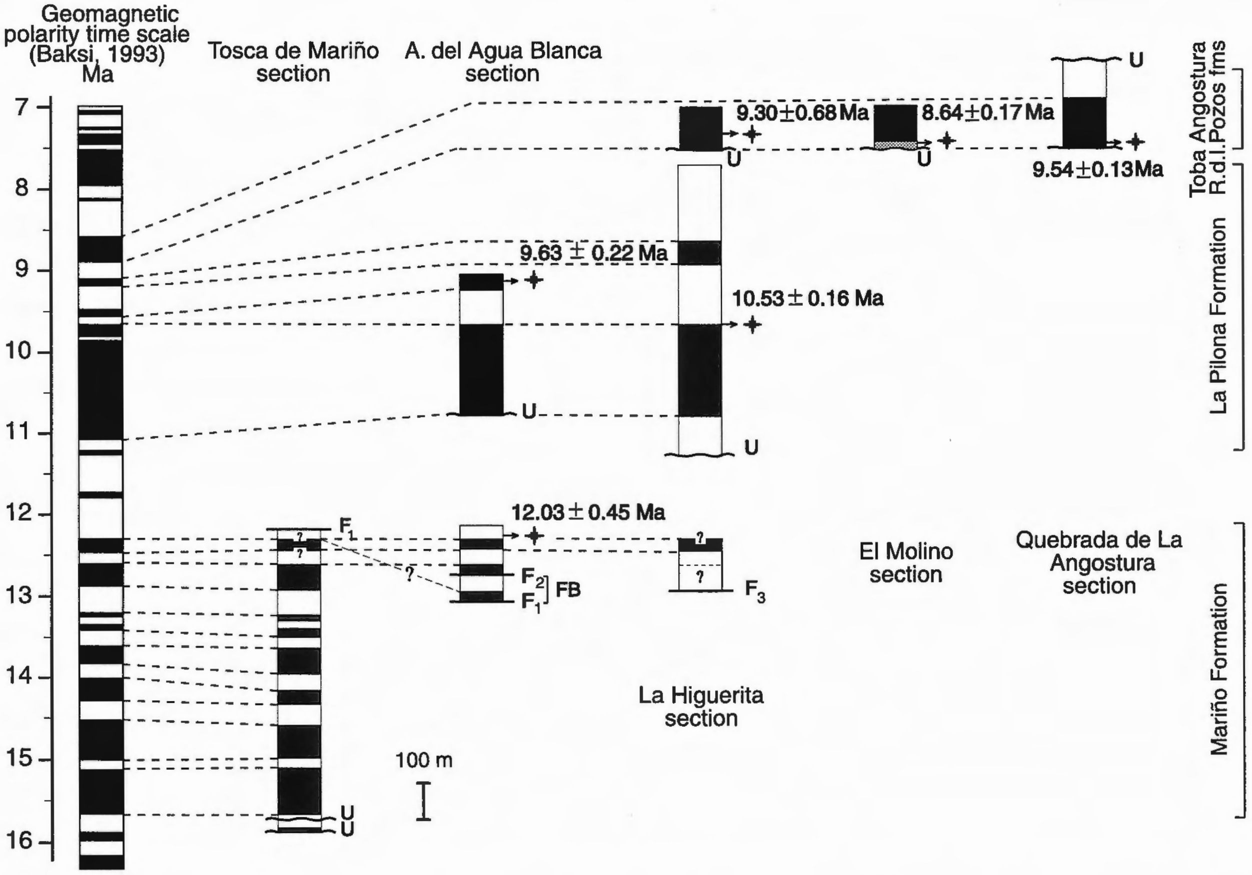

Figure 4. Magnetostratigraphic sections of the Mendoza Province Neogene strata showing the ^{40}Ar-^{39}Ar preferred age of interbedded tephras established by Irigoyen (1997) and this study, which assisted in tying the local magnetostratigraphy to the geomagnetic polarity time scale (Baksi, 1993) (after Irigoyen et al., in press). Black (white) zones represent normal (reversed) polarity. The lowest ~15 m of the Tobas Angostura unit in the El Molino section is covered and lacks paleomagnetic data (shaded portion). On the basis of lithostratigraphic correlations, strata from the fault block (FB) in the lower part of the Arroyodel Agua Blanca section may be placed at a stratigraphic level similar to that of strata above fault F_2.

estimate of the age of Md-15. The lowest biotite apparent age (2.63 ± 1.10 Ma) would indicate an upper estimate of a thermal disturbance, which is in agreement with regional evidence for postcrystallization tectonism in the study region.

Sample Md-10 was collected from an ash-bed near the base of the Tobas Angostura unit in the La Higuerita section (section III, Fig. 2a). Age spectrum analysis of Md-10 hornblende using furnace step-heating (Fig. 3f) gives a well developed plateau age of 9.30 ± 0.68 Ma. The plateau is defined by three steps containing over 99% of the total gas, with most of the gas (about 80%) evolved in the second step. Total-fusion analyses performed on five aliquots of Md-10 biotite yield an integrated age of 8.39 ± 0.18 Ma (Table 1). The biotite age is not in agreement with the hornblende age, but because only total fusion data are available for the biotite, this precludes an interpretation. However, because of susceptibility of biotite to resetting, as shown by Md-15, the hornblende age of 9.30 ± 0.68 Ma is interpreted to be the best estimate of the closure age of the Md-10 sample.

Sample Md-5 was collected from an air-fall horizon near the base of the Tobas Angostura unit in the El Molino section (section IV; Fig. 2a). The ^{40}Ar-^{39}Ar age spectrum of Md-5 hornblende displays a release pattern for each aliquot that conforms to a profile consistent with excess ^{40}Ar. The isochron treatment of the gas aliquots forming the plateau regions yields an age of 8.64 ± 0.17 Ma (M.S.W.D. = 20.9) assuming a present-day atmospheric composition. When the regression line is not fixed to the atmospheric composition, the resulting age is indistinguishable and the initial argon ratio does not deviate within the error from the expected value of 295.5, thus indicating that this portion of the gas has not been affected by excess ^{40}Ar. As in sample Md-13, the best evidence of an excess ^{40}Ar component is found in the first one or two steps of each aliquot. Total-fusion analyses performed on nine aliquots of Md-5 biotite yield an integrated age of 8.85 ± 0.37 Ma (Table 1). When biotite and hornblende age results are compared, they overlap at 8.64 ± 0.17 Ma (hornblende age), which is considered to be the best estimate for the closure age of the Md-5 sample.

Two samples (Md-8 and Md-9; Fig. 2b and c) were collected from air-fall horizons interbedded within Quaternary deposits. The correlation plot of Md-8 biotite (Fig. 3h) yields an age of 0.26 ± 0.10 Ma (M.S.W.D.= 1.2) assuming a present-day atmospheric argon composition. Therefore, it is considered that 0.26 ± 0.10 Ma records the closure age of Md-8 sample.

The correlation plot of sample Md-9 glass (Fig. 3i) yields an age of 0.39 ± 0.03 Ma (M.S.W.D. = 8.7) assuming a present-day atmospheric argon composition. Large errors in the apparent ages correspond to the lowest step of each aliquot and represent about 2.5% of the total gas. The correlation plot of Md-9 biotite (Fig. 3j) defines an age of 0.33 ± 0.10 Ma (M.S.W.D. = 3.6) assuming a present-day atmospheric argon composition. Four data points with large errors (>1%) are not shown in Figure 3j and are excluded from the calculation. When glass and biotite age results are compared, they overlap at the glass age. Therefore, the age 0.39 ± 0.03 Ma is considered to record the time of quenching of the Md-9 sample.

CONCLUSIONS

The ^{40}Ar-^{39}Ar geochronometric studies carried out on samples collected from air-fall deposits and reworked tuffs interbedded with Neogene nonmarine strata and from Quaternary deposits of the Mendoza Precordillera provides the following age constraints on the accumulation history of these strata.

1. The occurrence of a reworked tuff horizon in the uppermost part of the Mariño Formation indicates that the approximately 800 m thick sedimentary pile below the Md-12 horizon (section I, Fig. 2a) was deposited prior to 12.03 ± 0.45 Ma. The magnetostratigraphic study carried out on the Mariño Formation in section I indicates that this unit can be assigned to the interval 15.7–12.2 Ma (Irigoyen, 1997), on the basis of the comparison with the G.P.T.S. (Baksi, 1993; Fig. 4). Thus, the laser ^{40}Ar-^{39}Ar hornblende correlation plot age is in agreement with the established magnetostratigaphic correlation. Previous studies assigned the Mariño Formation to the Oligocene (De la Motta, 1957), to the Middle Miocene (Pascual and Odreman Rivas, 1973), and more recently to the Early Oligocene–Early Miocene in the 35.5–15.5 age interval (Yrigoyen, 1993a). According to Irigoyen (1997), deposition of the approximately 15.7–12.2 Ma Mariño Formation is linked with deformation in the Principal Cordillera (Fig. 1).
2. Sedimentation of the La Pilona Formation was, in part, coeval with explosive volcanic episodes as evidenced by the occurrence of air-fall tuff horizons dated at 9.63 ± 0.22 Ma (Md-13; section II, Fig. 2a) and 10.53 ± 0.16 Ma (Md-6; section III, Fig. 2a), which are found interbedded with nonmarine strata placed stratigraphically in the middle part of the unit.
3. The oldest strata of the La Pilona Formation must be younger than 12.03 ± 0.45 Ma (Mariño Formation) and not older than strata of the overlying Tobas Angostura Formation. On the basis of the magnetostratigraphic study and ^{40}Ar-^{39}Ar ages reported in this study, Irigoyen (1997) assigned the La Pilona Formation to the interval ~11.7-9.0 Ma (Fig. 4). Previous studies assigned the La Pilona Formation to the Late Miocene–Early Pliocene (e.g. Rolleri and Fernández Garrasino, 1979) and, more recently, to the Late Miocene, between 11.1 and 9.8 Ma on the basis of K-Ar data (Yrigoyen, 1993a, b). According to Irigoyen (1997), deposition of the ~11.7–9.0 Ma La Pilona Formation is associated with deformation in the Frontal Cordillera north of the study area (Fig. 1).

4. Deposition of the Tobas Angostura unit was, in part, coeval with eruptive episodes, as evidenced by tephra layers preserved in the lower part of the unit and dated at 9.30 ± 0.68 Ma (Md-10; section III, Fig. 2a) and 8.64 ± 0.17 Ma (Md-5; section IV, Fig. 2a) in both limbs of the La Pilona anticline. Approximately 20 to 25 km to the south, in the eastern flank of the Tupungato anticline, an air-fall tuff horizon from the basal part of the unit was dated at 9.54 ± 0.13 Ma (Md-15; section V, Fig. 2b). When dates of the Tobas Angostura unit in the La Pilona anticline are considered together, they indicate that accumulation of the lower part of this unit probably occurred between about 9.0 and 8.64 Ma (the older age limit constrained by the age of the youngest La Pilona strata as inferred from the magnetostratigraphic study of Irigoyen [1997]). On the basis of a ^{40}K-^{40}Ar hornblende age of 9.7 ± 1.1 Ma and a biotite age of 10.0 ± 0.5 Ma, Yrigoyen (1993a, b) assigned the Tobas Angostura Formation to the Late Miocene (about 9.8 Ma). On the basis of the magnetostratigraphic study and the isotopic dates reported herein, Irigoyen (1997) and Irigoyen et al. (in press) assigned the Tobas Angostura Formation to the interval 8.9–8.7 Ma and the normal polarity magnetozone encountered in the study sections was correlated with the 8.92–8.59 Ma normal chron of the G.P.T.S. (Baksi, 1993; Fig. 4). The beginning of this chron is placed at 8.92 Ma on the basis of interpolation between two calibration points at 1.78 and 9.67 ± 0.22 Ma (Baksi, 1993). This assignment is in disagreement with the ash horizon that records the base of the unit in the Quebrada de la Angostura locality, dated at 9.54 ± 0.13 Ma (Md-15; section V, Fig. 2a), which is approximately 0.6 Ma older than the isotopic age results from the other sections and the G.P.T.S. According to Irigoyen (1997), the consistent normal polarity of the Tobas Angostura unit in the three sections and the isotopic age results from the La Higuerita and El Molino localities favour the interpretation that the discrepancy between the ages of the G.P.T.S. and the Quebrada de la Angostura section may be largely accounted for by uncertainties in the isotopic age of sample Md-15 and in the isotopic ages of the G.P.T.S. tie-points (*see* Baksi, 1993). When totalled these account for an error of about 0.4 Ma. It is also possible that strata from the Quebrada de la Angostura section record somewhat older stratigraphic levels as this section is located about 20 km south. Irigoyen (1997) interprets the Tobas Angostura as a unit that records the latest and likely the largest eruptive episode in the Principal Cordillera.

5. Sedimentation of the oldest strata of the Río de los Pozos Formation that conformably overlie the upper portion of the Tobas Angostura Formation started at approximately 8.7 Ma. On the basis of the thickness of this unit in the Tupungato area and the rate at which these sediments accumulated, Irigoyen (1997) estimated that deposition of the Río de los Pozos Formation could have continued until about 7.2 Ma. If sedimentation rates slowed during deposition of the unit, as suggested by field evidence (i.e. abundant bioturbation, paleosol horizons), the youngest strata could be as young as about 6 Ma.

6. The age of the youngest Mogotes Formation strata in the La Pilona area is constrained by the 0.39 ± 0.03 Ma age determination for an ash-tuff layer unconformably overlying this unit (Md-9, Fig. 2c). In the Tupungato anticline, deposition of the youngest strata is constrained by an air-fall tuff horizon dated at 0.24 ± 0.05 Ma (Md-8, Fig. 2b). The age of the basal part of the Mogotes Formation is constrained by ash-tuff layers collected from the correlative Bajada Grande Formation and dated at 2.6 ± 0.1 Ma and 2.4 ± 0.3 Ma (*see* Marshall et al., 1986; Yrigoyen, 1993a, b). These age constraints indicate that deposition of the Mogotes Formation at the study site probably started at about 3 Ma and ended no later than about 1 Ma. Therefore, the Mogotes Formation is Late Pliocene, about 3–4 Ma younger than the Rio de los Pozos Formation. Deposition of the Mogotes Formation likely resulted from deformation in the flanking Frontal Cordillera, west of the study area (Irigoyen, 1997).

7. Motion of the La Pilona and Tupungato structures started after the beginning of accumulation of the Mogotes Formation at about 3.0 Ma and ceased prior to about 0.4 Ma. The occurrence of growth geometries in strata of the Mogotes Formation (Chiaramonte, 1996) suggests that deformation was in part synchronous with deposition of this unit.

ACKNOWLEDGMENTS

We thank R. Parrish and C. Roddick for their supervision and discussion of data during the early stage of this project. We thank Ken L. Buchan for the many discussions that helped clarify different aspects of this study and his insightful review of an earlier version of the manuscript. Hamish Sandeman is also thanked for a thorough review. We also thank Richard L. Brown for his comprehensive supervision of this project, discussions, and assistance during field work. This research was supported by a Natural Sciences and Engineering Research Council grant to Richard L. Brown. The Geological and Mining Survey of Argentina contributed substantially to the success of this project and provided logistic support during field work. Kip Hodges is thanked for use of the MIT laboratory.

REFERENCES

Baksi, A.K.
1993: A geomagnetic polarity time scale for the period 0–17 Ma, based on ^{40}Ar/^{39}Ar plateau ages for selected field reversals; Geophysical Research Letters, v. 20, no. 15, p. 1607–1610.

Baldis, B.A. and Chebli, G.
1969: Estructura profunda del área central de la Precordillera Sanjuanina; IV Jornadas Geólogicas Argentinas (Mendoza), Actas I, p. 47–66.

Caminos, R.
1979: Cordillera Frontal; *in* Geología Regional Argentina, (ed.) J.C.M. Turner; Academia Nacional de Ciencias, Córdoba, v. 1, p. 397–454.

Chiaramonte, L.
1996: Estructura y sismotectónica del anticlinal Barrancas, provincia de Mendoza; Licenciatura thesis, University of Buenos Aires, Argentina, 112 p.

De la Motta, H.
1957: Acerca del levantamiento geológico efectuado por la comision n° 5 al norte de la localidad de San José, provincia de Mendoza; Dirección General de Yacimientos Petrolíferos Fiscales, informe inédito, n° 504.

Harrison, T.M. and McDougall, I.
1980: Investigations of an intrusive contact, northwest Nelson, New Zealand II. Diffusion of radiogenic and excess ^{40}Ar in hornblende revealed by ^{40}Ar/^{39}Ar age spectrum analysis; Geochimica et Cosmochimica Acta, v. 44, p. 2005–2020.
1981: Excess ^{40}Ar in metamorphic rocks from Broken Hill, New South Wales: implications for ^{40}Ar/^{39}Ar age spectra and the thermal history of the region; Earth and Planetary Science Letters, v. 55, p. 123–149.

Hodges, K.V., Hames, W.E., Olszewski, W., Burchfiel, B.C., Royden, L.H., and Chen, Z.
1994: Thermobarometric and ^{40}Ar/^{39}Ar geochronologic constraints on Eohimalayan metamorphism in the Dinggyê area, southern Tibet; Contributions to Mineralogy and Petrology, v. 117, p. 151–163.

Irigoyen, M.V.
1997: Magnetic polarity stratigraphy and geochronological constraints on the sequence of thrusting in the Principal and Frontal cordilleras and the Precordillera of the Argentine Central Andes (33°S latitude); Ph.D. thesis, Carleton University, Ottawa, Ontario, 392 p.

Marshall, L.G., Drake, R.E., and Curtiss, G.H.
1986: ^{40}K-^{40}Ar age calibration of Late Miocene–Pliocene mammal-bearing Huayquerías and Tunuyán formations, Mendoza Province, Argentina; Journal of Paleontology, v. 60, p. 448–457.

Pascual, R. and Odreman Rivas, O.
1973: Las unidades estratigráficas del Terciario portadoras de mamíferos. Su distribución y sus relaciones con los acontecimientos diastróficos; V Congreso Geológico Argentino, Actas 3, p. 293–338.

Polanski, J.
1963: Estratigrafía, neotectónica y geomorfología del Pleistoceno pedemontano entre los ríos Diamante y Mendoza; Asociación Geológica Argentina Revista, no. XVII, v. 3-4 (1962), p. 127–349.

Ramos, V.A.
1988: The tectonics of the Central Andes, 30° to 33°S latitude; *in* Processes in Continental Lithospheric Deformation, (ed.) S. Clark and D. Burchfiel; Geological Society of America, Special Paper 218, p. 31–54.
1990: Field guide to geology of the Central Andes (31-33 SL); Central Andes Field Seminar, Buenos Aires, 69 p.

Ramos, V.A., Kay, S.M., and Pérez, D.J.
1996: El volcanismo de la región de Aconcagua: *in* Geología de la Región del Aconcagua; Provincias de San Juan y Mendoza; Dirección Nacional del Servicio Geológico, Subsecretaría de Minería de la Nación, Buenos Aires, Anales 24, Capítulo 10, p. 297–316.

Rebori, L.
1979: Contribución al conocimiento geológico del extremo sur de la Precordillera mendocina. Zona Cacheuta; Licenciatura thesis, University of San Juan, Argentina, 60 p.

Renne, P.R., Deino, A.L, Walter, R.C., Turrin, B.D., Swisher, C.C., III, Becker, T.A., Curtis, G.H., Sharp, W.D., and Jaouni, A-R.
1994: Intercalibration of astronomical and radioisotopic time; Geology, v. 22, p. 783–786.

Roddick, J.C.
1988: The assessment of errors in ^{40}Ar/^{39}Ar dating; *in* Radiogenic Age and Isotopic Studies: Report 2; Geological Survey of Canada, Paper 88-2, p. 3–8.

Rolleri, E.O.
1950: Informe geológico de la Hoja 23c, Mendoza; Dirección General de Yacimientos Petrolíferos Fiscales, informe inédito, no. 146.

Rolleri, E.O. and Fernández Garrasino, C.A.
1979: Comarca Septentrional de Mendoza; *in* Geología Regional Argentina, (ed.) J.C.M. Turner; Academia Nacional de Ciencias, Córdoba, v. 1, p. 771–809.

Truempy, E. and Lhez, R.
1937: División estratigráfica de los terrenos aflorantes en la region comprendida entre Luján de Cuyo, Potrerillos y Tupungato: Boletín de Informaciones Petroleras, Buenos Aires, no. XIV (152), p. 39–56.

Varela, R., Cingolani, C., Dalla Salda, L., Aragón, E., and Teixeira, W.
1993: Las monzodioritas y monzogabros de Cacheuta, Mendoza: edad, petrología e implicancias tectónicas: XII Congreso Geológico Argentino Y II Congreso de Exploración de Hidrocarburos, Actas, Tomo IV, p. 75–80.

Villeneuve, M.E. and MacIntyre, D.G.
1997: Laser ^{40}Ar/^{39}Ar ages of the Babine porphyries and Newman Volcanics, Fulton Lake map area, west-central Bristish Columbia; *in* Radiogenic Age and Isotopic Studies: Report 10, Geological Survey of Canada, Current Research 1997-F, p. 131–139.

York, D.
1969: Least squares fitting of a straight line with correlated errors; Earth and Planetary Science Letters, v. 5, p. 320–324.

Yrigoyen, M.R.
1979: Cordillera Principal; *in* Segundo Simposio de Geología Regional Argentina, (ed.) J.C.M. Turner; Academia Nacional de Ciencias, Córdoba, v. 1, p. 651–694.
1993a: Los depósitos sinorogénicos terciarios; *in* Geología y Recursos Naturales de la Provincia de Mendoza, (ed.) V.A. Ramos; XII Congreso Geológico Argentino y II Congreso de Exploración de Hidrocarburos, Relatorio, Capítulo I-11, p. 123–148.
1993b: Revisión estratigráfica del Neogeno de la region Cacheuta-La Pilona-Tupungato, Mendoza Septentrional, Argentina; XII Congreso Geológico Argentino Y II Congreso de Exploración de Hidrocarburos, Actas, Tomo II, p. 187–199.

– 5 –

Preliminary geochemical and Nd isotopic investigations of Archean volcanic and volcaniclastic rocks of the Yathkyed greenstone belt, Kivalliq region, Northwest Territories[1]

H.A. Sandeman[2], K. MacLachlan[2], and C. Relf[3]

Sandeman, H.A., MacLachlan, K., and Relf, C., 1999: Preliminary geochemical and Nd isotopic investigations of Archean volcanic and volcaniclastic rocks of the Yathkyed greenstone belt, Kivalliq region, Northwest Territories; in *Radiogenic Age and Isotopic Studies: Report 12; Geological Survey of Canada, Current Research 1999-F, p. 43–52.*

Abstract: Geochemical and Nd isotopic data for nine mafic supracrustal rocks from the upper and lower tectonostratigraphic units of the Yathkyed greenstone belt are presented. All are tholeiitic except one calc-alkaline andesite from the upper unit. Incompatible-element plots demonstrate that seven samples have flat, parallel patterns comparable to modern MORB, but exhibit increased light-rare-earth-element enrichment and variable development of minor Nb and Ti troughs with decreasing Mg number. The remaining three rocks are light-rare-earth-element enriched and have variably developed Nb and Ti troughs. Two sedimentary rocks from the lower unit have flat rare-earth-element patterns similar to those of the basalts. Nd isotopic data indicate that most samples are isotopically juvenile, having ε_{Nd} values ranging from +3.4 to +0.5, only slightly lower than depleted mantle. Two samples, one each from the upper and lower units, may have been contaminated by older crustal material.

Résumé : Les données géochimiques et isotopiques Nd portant sur neufs roches supracrustales mafiques prélevées dans les unités tectonostratigraphiques supérieure et inférieure de la ceinture de roches vertes de Yathkyed révèlent que ces roches sont toutes tholéiitiques à l'exception d'une andésite calco-alcaline de l'unité supérieure. Les courbes des éléments incompatibles montrent que les tracés graphiques de sept échantillons sont plats et parallèles, donc comparables à ceux obtenus pour les basaltes de la dorsale médio-océanique actuelle; cependant, ces échantillons présentent un enrichissement plus important en éléments de terres rares légers et un développement varié de creux mineurs de Nb et de Ti avec réduction du nombre Mg. Les trois autres roches sont enrichies en éléments de terres rares légers et leurs tracés montrent des creux de Nb et de Ti diversement développés. Deux roches sédimentaires de l'unité inférieure montrent des tracés plats pour les éléments de terres rares, semblables à ceux des basaltes. Les données isotopiques Nd indiquent que la plupart des échantillons sont peu évolués d'un point de vue isotopique et que leurs valeurs ε_{Nd} vont de +3,4 à +0,5, donc légèrement inférieures à celles du manteau appauvri. Il se peut que deux échantillons, respectivement des unités supérieure et inférieure, aient été contaminés par des matériaux crustaux plus anciens.

---

[1] Contribution to the Western Churchill NATMAP

[2] Geological Survey of Canada, 601 Booth Street, Ottawa, Ontario K1A 0E8

[3] Indian and Northern Affairs Canada, Box 1500, Yellowknife, Northwest Territories X1A 2L9

INTRODUCTION

A joint field project initiated in 1997 by the Government of the Northwest Territories and Indian and Northern Affairs Canada as part of the Western Churchill NATMAP Program was undertaken to improve the geological database of the Neoarchean Yathkyed greenstone belt. Whole-rock geochemical and Nd isotopic studies of the volcanic rocks of the belt have been carried out by the Geological Survey of Canada to help constrain the tectonomagmatic evolution of the Yathkyed greenstone belt and to provide a high-quality geochemical database for future comparative investigations of the diverse greenstone belts of the western Churchill Province. This paper outlines whole-rock geochemical and Nd isotopic investigations of a suite of nine mafic volcanic rocks and two volcaniclastic sedimentary rocks obtained from the 1997 map area.

GEOLOGICAL SETTING

The Yathkyed greenstone belt forms part of a series of Neoarchean volcano-plutonic packages in the western Churchill Province, formerly grouped as the Rankin-Ennadai belt (Eade, 1986). The Yathkyed greenstone belt forms a northeast-trending package of volcanic and metasedimentary rocks and associated granitoid rocks that occur (Fig. 1) immediately south and southeast of the Snowbird Tectonic Zone (Hoffman, 1988). The greenstone belt forms a northwest-dipping, southeast-younging panel bounded along its southeastern margin by the Tyrrell shear zone. The shear zone records an early episode of oblique (sinistral) northwest-side-up displacement suggesting that it may be a thrust nappe (Relf et al., 1998). The volcanic and metasedimentary rocks comprise a ca. 7 km thick sequence that ranges from greenschist facies in the structurally lowermost sections to amphibolite facies in the uppermost parts. On the basis of 1998 mapping in the northeastern part of the belt, two tectonostratigraphic units, separated by a second mylonitic shear zone, have been distinguished (Relf et al., 1999). The lower tectonostratigraphic unit comprises a package of mafic volcanic rocks that range from amphibolite facies in the northeast to greenschist facies, pillowed volcanic rocks in the southwest. These are intruded by biotite monzogranite near the structural top of the package. The upper tectonostratigraphic unit is composed of amphibolite facies mafic volcanic rocks at the base that grade upward into mixed mafic to felsic volcanic rocks and psammite and pelite at the structural top; all are intruded by foliation-parallel sheets of tonalite. Because of

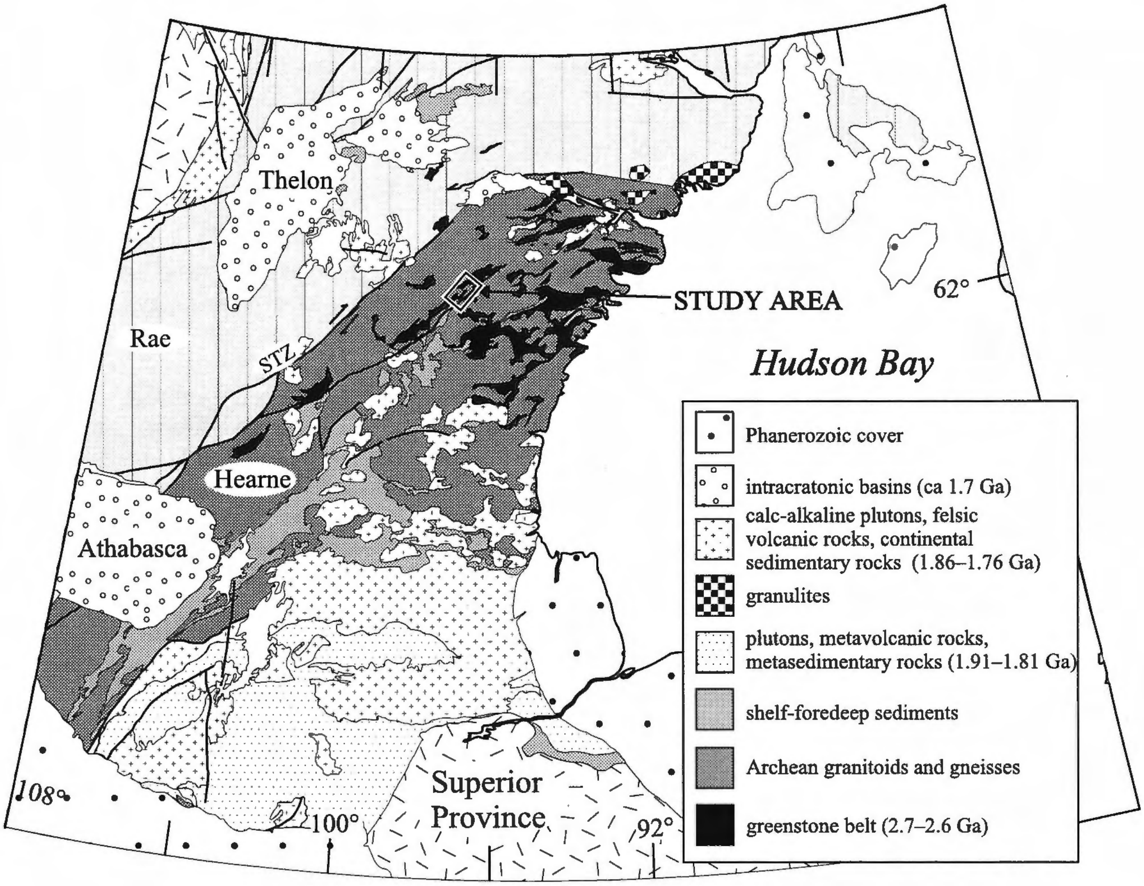

Figure 1. Location map of the study area and its position relative to the major lithotectonic domains of the northwestern Canadian Shield (modified from Hoffman, 1988). STZ = Snowbird tectonic zone

poor exposure, the location of the contact between the upper and lower tectonostratigraphic units is not clearly defined in the 1997 mapping area, but its trace has been approximated in Figure 2. The significance of the boundary between the upper and lower tectonostratigraphic units in terms of the bulk compositions of mafic supracrustal rocks will only be clarified on the basis of geochemical results from samples collected during the 1998 field season.

GEOCHEMISTRY

Analytical methods

Nine whole-rock specimens of chloritic, pillowed, mafic volcanic rocks and foliated hornblende ± garnet amphibolite and two samples of fine-grained, volcaniclastic sedimentary rocks were collected from the upper and lower tectonostratigraphic packages in the southern part of the belt. The majority of the samples (n = 6) are from the lower package along a section orthogonal to the strike of the belt (Fig. 2). Approximately 1.5 kg of each rock sample was crushed to chips in a Braun jaw crusher and a 50 g split of each was pulverized to a fine powder in an agate ring mill. All analyses were obtained at the Analytical Chemistry Laboratories of the Geological Survey of Canada except for the trace elements Sr and Zr, which were obtained through X-ray fluorescence (XRF) analysis of pressed powder discs at the Department of Earth and Planetary Sciences, McGill University. The major elements were determined by XRF analysis on fused discs and FeO was obtained by titration. The trace elements Ba, Be, Co, Cr, Cu, Ni, Sc, V, and Zn were analysed by ICP-ES, whereas all other trace elements including Cs, Ga, Pb, Rb, Hf, Th, U, Ta, Nb, Y, and the rare-earth elements (REE) were determined through ICP-MS. Analytical errors for the data, as based on analyses of unknown duplicates and analyses of reference materials, are quoted at less than 5% for the major elements, less than 10% for those trace elements determined by XRF, 10% for ICP-ES analyses, and less than 5% for ICP-MS analyses. Complete whole-rock geochemical data are presented in Table 1.

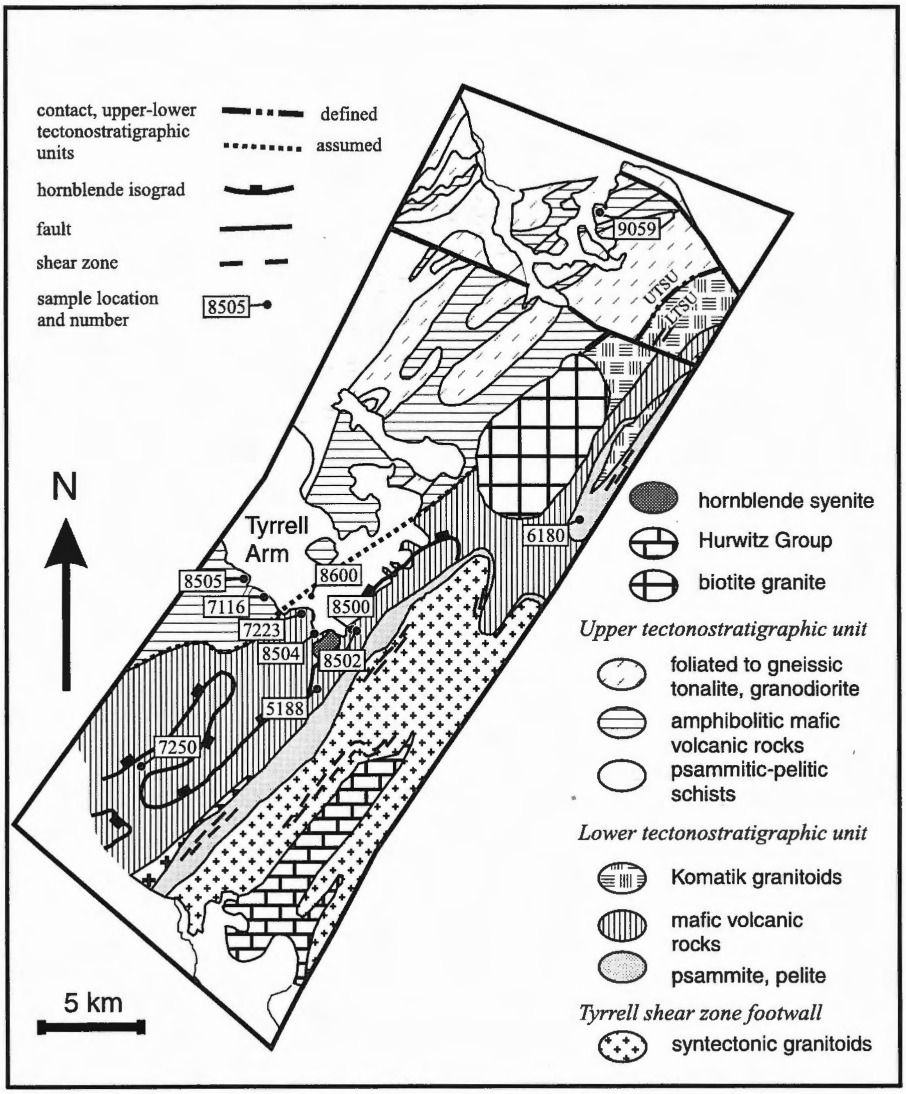

Figure 2.

Simplified geological map of the south-central part of the Yathkyed greenstone belt and the locations of specimens discussed in the text (modified from Relf et al., 1998).

Table 1. Whole-rock geochemical data for nine mafic volcanic and two volcanogenic sedimentary rocks of the Yathkyed greenstone belt. Major oxides are in weight % and trace elements, in ppm. UTU = upper tectonostratigraphic unit; LTU = lower tectonostratigraphic unit; PB = pillowed basalt; AMP = amphibolitic metabasite; VS = volcanogenic sedimentary rock; bd = below detection; na = not analyzed

Sample	**Y-5188**	**Y-7233**	**Y-7250**	**Y-8500**	**Y-8502**	**Y-8504**	**Y-7116A**	**Y-8505A**	**Y-9059**	**Y-8600**	**Y-6180**
Unit	**LTU**	**LTU**	**LTU**	**LTU**	**LTU**	**LTU**	**UTU**	**UTU**	**UTU**	**LTU**	**LTU**
Rock type	**PB**	**AMP**	**PB**	**PB**	**PB**	**PB**	**AMP**	**AMP**	**AMP**	**VS**	**VS**
Easting	**581500**	**580375**	**569925**	**584475**	**585025**	**582275**	**578225**	**576675**	**600900**	**581050**	**599775**
Northing	**6916125**	**6921650**	**6909000**	**6920800**	**6920650**	**6920500**	**6922425**	**6924100**	**6949500**	**6922700**	**6928500**
Zone	**14V**	**14V**	**14V**	**14V**	**14V**	**14V**	**14V**	**14V**	**14V**	**14V**	**14V**
SiO_2	46.9	49.0	48.8	48.7	47.3	48.7	48.8	59.3	48.5	56.0	64.0
TiO_2	0.88	0.88	0.79	1.03	0.93	0.85	1.11	0.95	1.80	1.59	1.49
Al_2O_3	15.3	14.8	14.6	14.3	15.0	14.8	14.8	14.9	14.3	20.4	18.9
FeO^T	11.88	11.52	11.07	11.79	11.88	12.69	12.78	6.84	15.03	7.83	3.15
Fe_2O_3	3.10	3.30	2.40	3.10	3.30	4.20	3.4	1.70	3.10	1.40	0.80
FeO	9.1	8.6	8.9	9.0	8.9	8.9	9.7	5.3	12.2	6.6	2.4
MnO	0.20	0.22	0.20	0.20	0.20	0.27	0.22	0.12	0.39	0.18	0.10
MgO	7.50	6.81	8.67	6.28	8.37	6.78	7.22	4.72	5.19	1.02	0.48
CaO	10.82	12.84	10.09	11.85	10.42	11.83	10.49	5.46	10.61	4.51	4.27
Na_2O	2.00	2.00	1.90	1.80	1.70	1.40	2.00	3.60	0.80	5.50	4.50
K_2O	0.10	0.38	0.05	0.13	0.10	0.85	0.44	1.86	1.26	0.70	1.79
P_2O_5	0.07	0.07	0.06	0.09	0.07	0.07	0.09	0.24	0.19	0.12	0.12
LOI	2.9	0.8	2.7	2.9	2.8	1.4	0.9	0.8	1.4	1.4	1.1
Mg number	52.9	51.2	58.3	48.7	55.7	48.8	50.2	55.2	38.2	18.8	21.5
Cr	330	320	340	310	280	350	210	160	50	340	310
Ni	140	130	150	120	160	130	110	120	63	150	180
Co	52	51	50	47	49	44	55	31	48	59	95
Sc	40.0	39.0	35.0	36.0	38.0	40.0	39.0	16.0	28.0	58.0	47.0
V	280	270	240	250	270	270	290	140	310	450	410
Pb	2	bd	bd	16	3	6	bd	4	3	50	16
Zn	79	75	73	82	79	110	90	120	110	170	75
Rb	1.5	14.0	0.5	1.6	1.9	50.0	15.0	62.0	54.0	26.0	57.0
Cs	0.06	1.70	0.05	0.06	0.08	0.97	0.40	1.90	22.00	4.20	4.30
Ba	54	110	80	65	42	130	100	310	250	260	410
Sr	110	300	130	140	210	100	130	310	100	600	460
Ga	17	16	15	16	17	14	18	20	21	23	21
Ta	0.16	0.21	0.13	0.29	0.14	0.17	0.24	0.44	0.59	na	na
Nb	2.2	3.5	2.0	3.9	2.1	2.3	3.2	7.8	8.7	4.4	4.0
Hf	1.1	1.2	0.9	1.5	0.9	1.3	1.8	3.6	3.6	2.1	2.3
Zr	38	36	29	53	28	44	66	160	140	77	80
Y	22.0	22.0	18.0	27.0	20.0	20.0	25.0	19.0	40.0	25.0	20.0
Th	0.25	0.38	0.21	0.57	0.21	0.28	0.32	3.40	1.40	0.42	0.38
U	0.10	0.16	0.09	0.15	0.07	0.14	0.10	0.65	0.38	0.11	0.12
La	2.7	9.1	2.4	5.2	2.6	3.0	3.9	20.0	11.0	4.8	4.2
Ce	7.6	19.0	6.6	14.0	7.3	8.1	11.0	46.0	30.0	14.0	12.0
Pr	1.20	2.40	1.00	2.00	1.10	1.20	1.60	5.70	4.30	2.00	1.80
Nd	6.3	11.0	5.4	10.0	6.1	6.3	8.3	24.0	20.0	11.0	9.0
Sm	2.00	2.70	1.80	3.20	2.00	2.10	2.60	4.60	5.80	3.20	2.70
Eu	0.80	0.89	0.69	1.00	0.78	0.82	0.95	1.30	1.80	1.70	0.98
Gd	3.00	3.20	2.60	4.00	2.90	2.90	3.60	4.10	6.60	4.20	3.30
Tb	0.55	0.56	0.46	0.72	0.52	0.52	0.65	0.61	1.10	0.70	0.59
Dy	3.50	3.40	2.80	4.40	3.30	3.20	4.00	3.30	6.80	4.30	3.50
Ho	0.75	0.77	0.63	0.95	0.74	0.71	0.88	0.63	1.50	0.93	0.72
Er	2.20	2.20	1.80	2.70	2.10	2.10	2.60	1.70	4.20	2.70	2.10
Tm	0.32	0.30	0.26	0.38	0.30	0.29	0.39	0.26	0.58	0.38	0.29
Yb	2.20	2.20	1.70	2.70	2.10	2.10	2.80	1.70	4.10	2.70	1.90
Lu	0.32	0.33	0.24	0.39	0.28	0.29	0.38	0.24	0.58	0.38	0.26

Table 2. Nd isotopic data for volcanic and volcanogenic sedimentary rocks of the Yathkyed greenstone belt. The various parameters included herein are discussed in the text.

sample	Sm (ppm)	Nd (ppm)	$^{147}Sm/^{144}Nd$ measured	$^{143}Nd/^{144}Nd(m)$ measured	$^{143}Nd/^{144}Nd$ at t = 2.68 Ga	ε_{Nd}
Y-7233	3.36	12.86	0.1577	0.512122	0.509333	3.40
Y-8502	2.00	5.89	0.2056	0.512962	0.509327	3.28
Y-7250	1.69	5.04	0.2033	0.512898	0.509302	2.80
Y-5188	2.02	5.97	0.2044	0.512925	0.509311	2.96
Y-8500	3.05	9.61	0.1919	0.512581	0.509187	0.54
Y-8504	1.99	6.14	0.1963	0.512732	0.509260	1.97
Y-7116A	2.46	7.66	0.1940	0.512722	0.509291	2.58
Y-8505	4.46	22.37	0.1204	0.511346	0.509217	1.13
Y-8505*	4.36	21.91	0.1204	0.511332	0.509204	0.86
Y-9059	5.41	19.23	0.1699	0.512295	0.509291	2.57
Y-6180	2.54	8.21	0.1869	0.512624	0.509320	3.15
Y-8600	3.07	9.67	0.1921	0.512701	0.509305	2.84

* designates a duplicate analysis

Analytical procedures for Sm-Nd analyses are a variant of those employed by Richard et al. (1976). Whole-rock powders (ca. 0.2 g) were spiked with a ^{148}Nd-^{149}Sm mixed solution and dissolved in teflon bombs in a warm HF-HNO_3 solution. Once dissolution was complete, the bombs were inserted into steel jackets and placed in a furnace at 170°C for five days. The bombs were removed and the solutions were dried down on a hot plate. The rare-earth elements were converted to chloride complexes through addition of 6 N HCl to each bomb, all of which were returned to the steel jackets and placed in the furnace (T = 170°C) for 12 hours.

Nd and Sm were separated using wet chemical chromatographic methods, ultra-pure acids, and conventional cation-specific separation resins. Isotopic ratios were determined by thermal ion mass spectrometry using a Finnigan Mat 261 mass spectrometer run in the static mode. Neodymium isotopic compositions were normalized to $^{146}Nd/^{144}Nd = 0.7219$ and corrected to La Jolla $^{143}Nd/^{144}Nd = 0.511860$. External reproducibility, based on repeated analyses of an internal laboratory Nd AMES metal solution, yielded $^{143}Nd/^{144}Nd = 0.512154 \pm 0.000012$ (2σ: n = 15). Values of ε_{Nd} were calculated using a present-day chondritic uniform reservoir (CHUR) composition of $^{143}Nd/^{144}Nd = 0.512638$ and $^{147}Sm/^{144}Nd = 0.1967$. The 2σ reproducibility of the ε_{Nd} values are calculated to be ca. ± 0.5 ε units. The Nd isotopic data for the 11 samples are presented in Table 2.

Major-element and compatible trace-element variations

Mafic volcanic rocks of the Yathkyed belt are classified as basalts in the total alkalis versus SiO_2 diagram (Fig. 3A) of LeBas et al. (1986) except for specimen Y-8505, which is an andesite. The samples (excluding Y-8505) exhibit FeO^T (total iron as FeO) and TiO_2 enrichment trends (Fig. 3B) with increasing fractionation, features that are characteristic of tholeiitic basalts (Irvine and Barager, 1971; Miyashiro, 1974). Magnesium numbers (Mg numbers = molecular $MgO/MgO+FeO^T$) and Cr and Ni contents are variable, ranging from 38.2 to 65.0 ppm, 51 to 356 ppm, and 64 to 344 ppm, respectively. These values are considered too low for rocks representing magmas formed in equilibrium with a modern peridotitic mantle (Mg numbers >70, Cr >1000, Ni > 400; Roeder and Emslie, 1970), probably implying that these basalts have undergone crystal fractionation.

Incompatible trace elements

Although the data set is small, we examine the compositional variation of the mafic rocks on binary, incompatible-element variation diagrams using Zr as the abscissa, because this element is typically considered to be highly incompatible during fractionation of basaltic melts (e.g. Pearce and Norry, 1979). All samples exhibit positive linear trends on plots of log Nb and Y versus log Zr (Fig. 4A, B), implying that some combination of olivine+clinopyroxene±plagioclase was removed from the melt (Pearce and Norry, 1979). On a plot of log Zr/Y versus log Zr (Fig. 5), there is evidence to suggest the possibility of heterogeneity in the source of these rocks. It is clear that the samples from the lower unit, with the possible exception of Y-8500, exhibit similar variations in Zr/Y relative to Zr, but rocks of the upper unit have higher Zr/Y ratios indicating a more enriched alkalic component. This interpretation is supported by the plot of Th/Yb versus Ta/Yb (Fig. 6) on which the samples plot parallel to the modern-day mantle array, suggesting variably depleted and enriched mantle sources (Pearce, 1982). However, most samples plot above the modern-day mantle array. The relative enrichment in Th/Yb suggests an additional source component involved in the petrochemical evolution of these rocks, probably related to subduction.

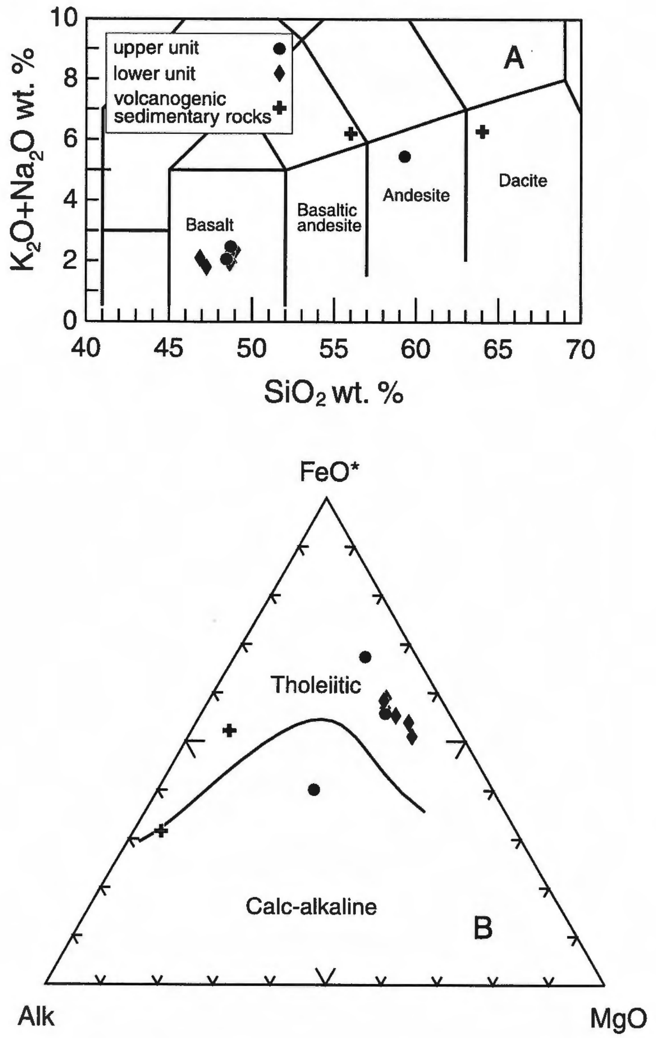

***Figure 3.** A) Total alkalies versus SiO_2 (LeBas et al., 1986) for volcanic and volcanogenic sedimentary rocks of the Yathkyed greenstone belt. **B)** AFM diagram (Irvine and Barager, 1971) for volcanic and volcanogenic sedimentary rocks of the Yathkyed greenstone belt demonstrating that all mafic rocks are tholeiitic except for Y-8505, which is calc-alkaline.*

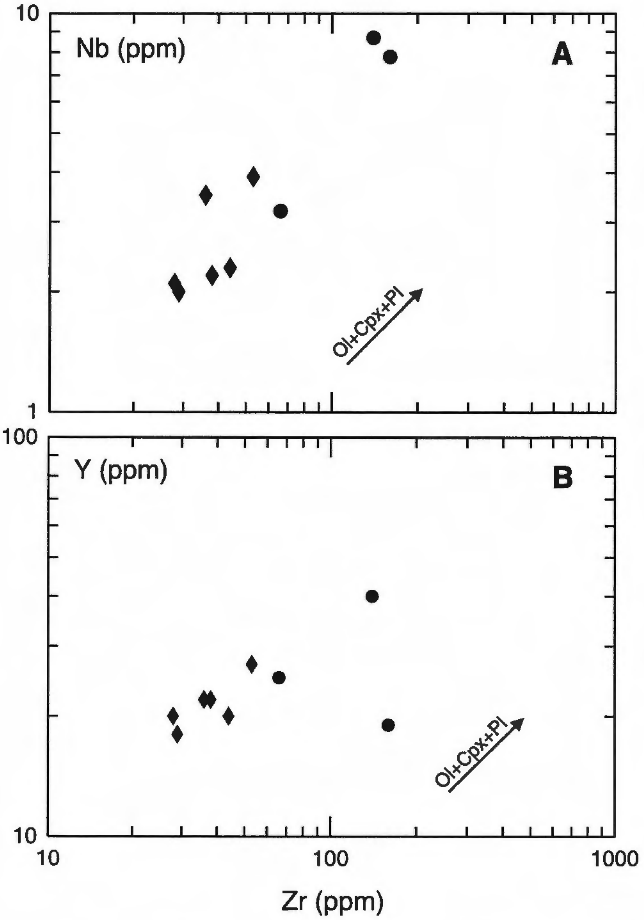

***Figure 4.** A) Log Nb versus log Zr diagram for mafic volcanic rocks of the Yathkyed belt. Note the positive trend of the data, which approximately parallels a vector corresponding to model fractional crystallization of the assemblage olivine+clinopyroxene+plagioclase (Pearce and Norry, 1979). **B)** Log Y versus log Zr diagram for mafic volcanic rocks of the Yathkyed belt demonstrating relationships comparable to those described in A). Fractionation of intermediate composition clinopyroxene or possibly amphibole may explain why one specimen (Y-8505) plots well below the trend line of the remainder of the specimens.*

Figure 5.

A diagram showing variations in log Zr/Y versus log Zr space and indicating that the samples from the upper tectonostratigraphic unit have more alkaline compositions than those from the lower unit. The heavy line on which C3 chondrite is plotted represents the inferred variations in mantle source compositions. The line labelled PM reflects the variation in Zr/Y and Zr resulting from a high degree (ca. 30%) of batch partial melting of moderately depleted mantle whereas that labelled CSF reflects the variation in Zr/Y and Zr resulting from closed system fractionation (Pearce and Norry, 1979). It is unlikely that the specimens from the lower and upper units are related through partial melting of a similar mantle source or through closed-system fractionation of a common parental magma.

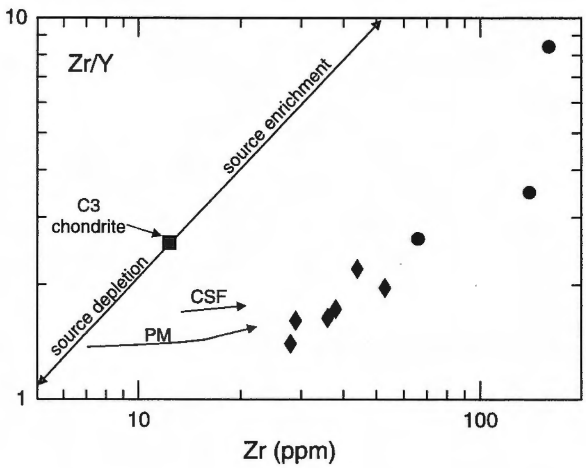

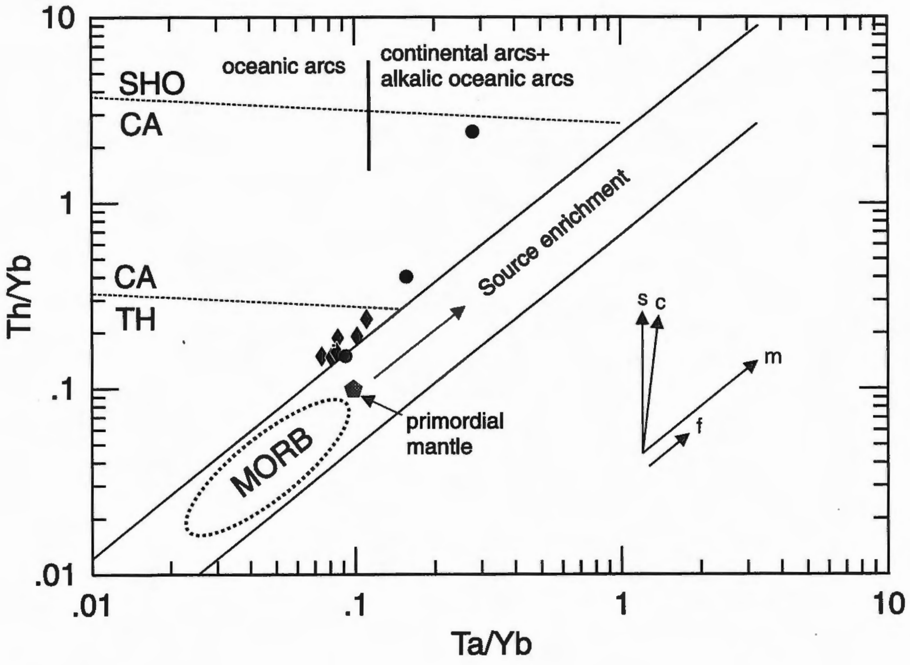

Figure 6. *Plot of Th/Yb versus Ta/Yb (Pearce, 1982) for mafic rocks demonstrating their mild enrichment in Th/Yb relative to the mantle array. Also note the enrichment of Ta/Yb in rocks from the upper tectonostratigraphic unit. SHO = shoshonitic; CA = calc-alkaline; TH = tholeiitic. The vectors shown on the right hand side schematically represent the effects of: s – subduction zone enrichment; c – crustal contamination; m – variation in the mantle source and; f – about 50 per cent fractional crystallization. Symbols as in Figure 3.*

On a chondrite-normalized rare-earth-element (REE) diagram (Sun and McDonough, 1989), basalts from the lower tectonostratigraphic package are characterized by flat to slightly light-REE depleted ($La_N/Yb_N = 0.95–1.50$), mutually parallel, rare-earth-element patterns, having overall abundances 10 to 20 times that of chondrites (Fig. 7A). The only exception is specimen Y-7233, which is characterized by a mildly light-REE-enriched pattern with $La_N/Yb_N = 2.20$. Two (Y-8505 and Y-9059) of the three specimens from the upper package are characterized by more fractionated, light-REE-enriched patterns having $La_N/Yb_N = 2.20–8.73$, whereas Y-7116a has $La_N/Yb_N = 1.04$ (Fig. 7B). Rocks from both tectonostratigraphic packages (samples Y-8500, Y-8501, Y-7116A and Y-8505, Y-9059) exhibit minor negative Eu anomalies. Because Eu^{+2} is readily substituted in the plagioclase structure in place of Ca^{+2} (Kay and Hubbard, 1978), the negative Eu anomalies exhibited by these samples indicate some fractionation of plagioclase.

Extended incompatible-element plots

All specimens are plotted on extended incompatible-element diagrams (Fig. 8A, B) and normalized to primitive mantle (*after* Sun and McDonough, 1989). Three (Y-5188, Y-7250, and Y-8502) of the six basalts of the lower unit are characterized by flat, extended trace-element patterns (at ca. three to five times primitive mantle) and two others (Y-8500 and Y-8504) exhibit minor troughs at Nb and Ti (Fig. 8A), features compatible with volcanic-arc or back-arc-basin basalts. One specimen (Y-7233) exhibits light-REE enrichment, high La/Nb, and a Ti anomaly, but has low Th/Nb. It appears chemically similar to back-arc-basin or volcanic-arc basalts, but is depleted in Th, a feature not readily explained at this time. The three specimens from the upper unit exhibit distinct patterns (Fig. 8B). Although two (Y-9059 and Y-8505) of the three are enriched in Th and the light-REE elements and are characterized by negative Nb and Ti anomalies typical of arc-related magmas, they have very different abundances of the middle and heavy rare-earth elements. The third sample (Y-7116a) from the upper unit has a flat, extended trace-element pattern comparable in shape and elemental abundances to those of the lower tectonostratigraphic unit.

Nd isotopic data

Although the age of the rocks of the Yathkyed belt is not precisely constrained, Loveridge et al. (1988) presented a number of imprecise U-Pb zircon (bulk separate) ages for Archean rocks of the Yathkyed–Angikuni Lake segment of the greenstone belt that range from 2680 to 2650 Ma. These ages are similar to those for rocks of the Kaminak greenstone belt, for which precise zircon U-Pb ages have been obtained (*see* Davis et al., 1998). Herein we recalculate ^{144}Nd/^{143}Nd and ε_{Nd} values to t = 2680 Ma in light of this geochronological data. The uncertainty in the age of these rocks might greatly affect their calculated ε_{Nd} values. Application of an age of 2700 Ma results in a negligible change of ≤0.2 units for the calculated ε_{Nd} values. If the age of the rocks is 20 Ma younger than assumed, however, then the ε_{Nd} values, in particular for the LREE-enriched samples, may change by up to 0.8 units.

All the mafic volcanic rocks, from both the upper and lower tectonostratigraphic units, yield present-day ^{144}Nd/^{143}Nd ratios ranging from 0.512962 to 0.511332, corresponding to $\varepsilon_{Nd(t\,=\,2680)}$ values of +0.5 to +3.4 (Table 2, Fig. 9). The values for the basalts of the lower tectonostratigraphic unit form a tight cluster on the ε_{Nd} versus time plot where all specimens, with the exception of Y-8500, overlap in error and exhibit values comparable to those estimated for Neoarchean depleted mantle (Machado et al., 1986). The ε_{Nd} value for Y-8500 (+0.5) is significantly outside the range for the remainder of the basalts of the lower tectonostratigraphic unit, implying interaction with older LREE-enriched material through either fluid fluxing at a subduction zone or assimilation of crustal material during ascent.

The ε_{Nd} values obtained for the three basalts of the upper tectonostratigraphic unit overlap with those for the basalts of the lower tectonic package. Two of them are similar to values estimated for Neoarchean depleted mantle and indicate that the rocks represent juvenile melts derived from an isotopically depleted mantle reservoir. The third specimen (Y-8505), however, yielded an ε_{Nd} value of +1.13, significantly lower than those of the other two samples. This value suggests interaction with older LREE-enriched material through either fluid fluxing at a subduction zone or assimilation of crustal material during ascent.

These results are similar to those reported by Thériault and Tella (1997) for basaltic rocks of the Rankin Inlet greenstone belt and the Tavani segment of the Kaminak greenstone

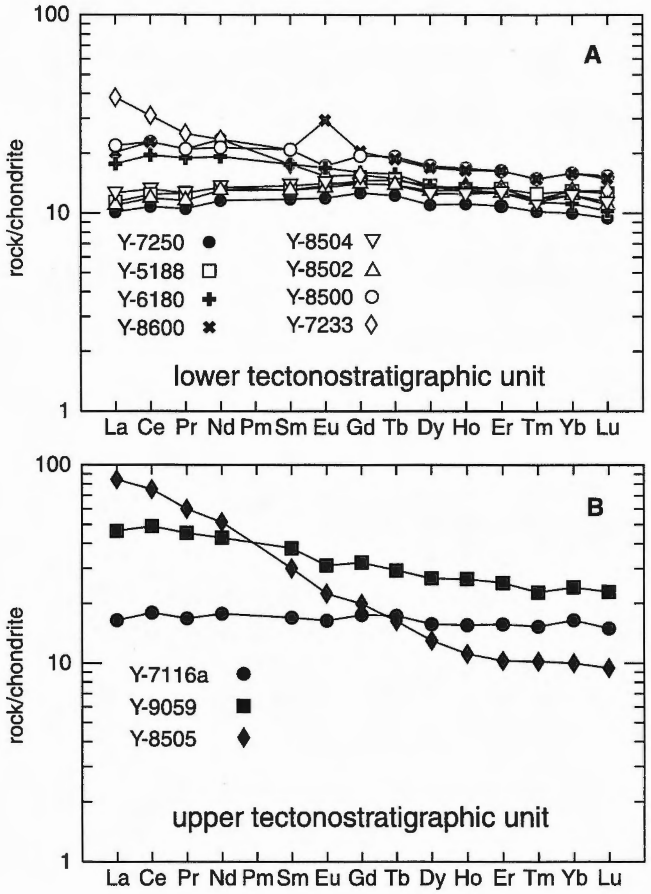

***Figure 7.** Chondrite-normalized rare-earth-element plots for samples from **A)** the lower tectonostratigraphic unit and **B)** the upper tectonostratigraphic unit. Normalizing values are from Sun and McDonough, 1989.*

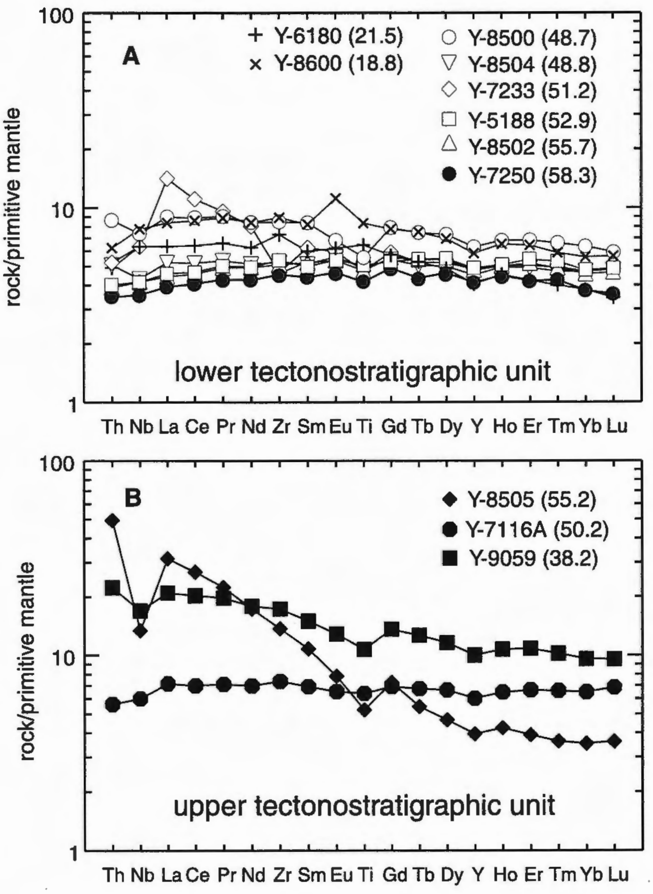

***Figure 8.** Primitive-mantle normalized extended trace-element diagram for samples from **A)** the lower tectonostratigraphic unit and **B)** the upper tectonostratigraphic unit. Numbers in parentheses are calculated Mg numbers for each sample. Normalizing values are from Sun and McDonough, 1989.*

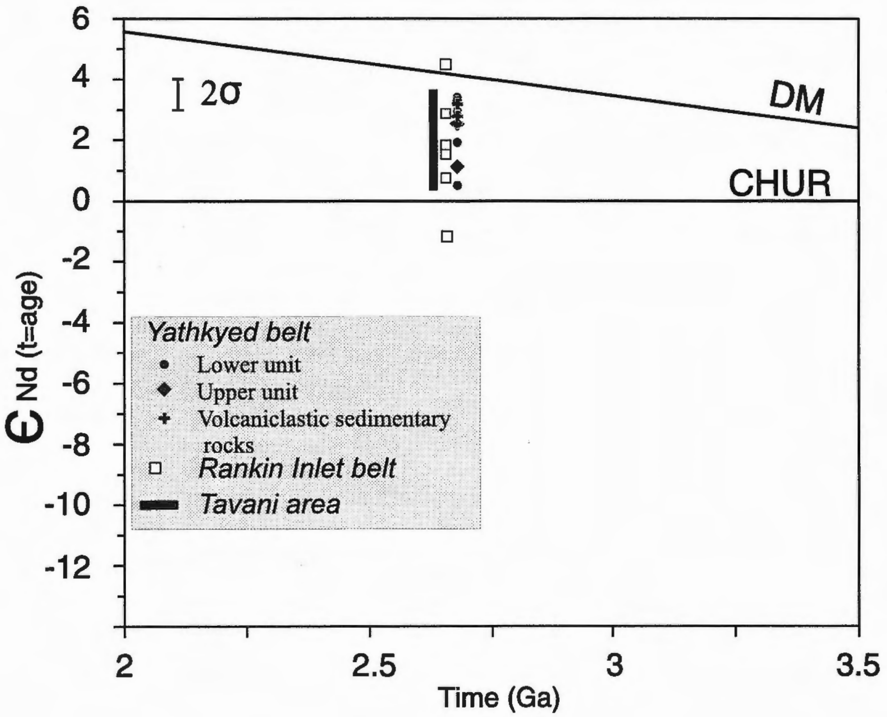

Figure 9.

$\varepsilon_{Nd(T\ =\ 2680\ Ma)}$ versus time for the 11 specimens from the Yathkyed greenstone belt, compared with those from the Rankin Inlet belt and Tavani segment of the Kaminak greenstone belt (Thériault and Tella, 1997). The ε_{Nd} results are calculated at 2.68 Ga. The parameters for the ε_{Nd} calculations include: $^{143}Nd/^{144}Nd_0(CHUR) = 0.512638$; $^{147}Sm/^{144}Nd(CHUR) = 0.1967$ (Jacobsen and Wasserburg, 1980). The depleted mantle curve was calculated according to the parameters of Goldstein et al. (1984). Data from the Rankin Inlet belt and the Tavani segment of the Kaminak greenstone belt are from Thériault and Tella (1997). CHUR = chondritic uniform reservoir; DM = depleted mantle

belt, wherein those authors observed a large variation in the ε_{Nd} data ranging from values of +4.5 to -1.1. The higher values were interpreted to represent suitable values for magmas extracted from Neoarchean mantle, but two of the analyses, one from the lower volcanic cycle of the Rankin Inlet belt (ε_{Nd} = -1.1, 85TXA-399A) and the other from the Tavani region (ε_{Nd} = +0.6, 89TX-072), seem to indicate contamination from older crustal material (Thériault and Tella, 1997).

The two volcanogenic sedimentary rocks from the study area also yield juvenile Nd isotopic compositions. Their $^{143}Nd/^{144}Nd$ ratios (0.512624 and 0.512701) and corresponding $\varepsilon_{Nd(t\ =\ 2680)}$ values (+3.15 and +2.84) are comparable to those of the basaltic rocks, in particular those of the lower tectonostratigraphic unit. These data, in conjunction with whole-rock geochemical evidence demonstrating that the rocks are similar in composition to the basalts of the lower tectonostratigraphic unit, indicate that the detritus in these sedimentary rocks was locally derived and contained no old, recycled crustal material.

DISCUSSION

The mafic volcanic rocks collected for this study are, with one exception, tholeiitic basalts which exhibit FeO^T and TiO_2 enrichment trends, but have compatible-element compositions inconsistent with their being in equilibrium with modern peridotitic mantle. Such data are commonly interpreted to indicate that the rocks have probably undergone crystal fractionation in subcrustal or crustal magma chamber(s) after segregation from their source. Both the incompatible-element and REE abundances and variations indicate fractionation of a mineral assemblage including olivine+clinopyroxene±plagioclase, whereas negative Eu anomalies in chondrite-normalized REE plots clearly imply minor plagioclase fractionation.

Extended incompatible-element plots normalized to primitive mantle (Sun and McDonough, 1989) outline some differences and similarities between mafic rocks of the lower and upper tectonostratigraphic units. Three of six samples from the lower unit exhibit generally flat patterns, similar to modern N-MORB, whereas two are characterized by minor Nb troughs relative to Th and La. One specimen exhibits significant LREE enrichment compared to the remainder, but has no Nb trough. All mafic volcanic rocks from the lower unit have minor negative Ti anomalies relative to Eu and Gd, a feature characteristic of volcanic arc magmas, but also apparent in MORB-like rocks from the Yathkyed belt. The petrochemical significance of this feature is, however, not clear at the present time. The two volcanogenic sedimentary rocks from the lower unit have extended trace-element patterns similar to the N-MORB basalts, but are characterized by somewhat elevated light-REE abundances.

Two of the three samples from the upper unit exhibit negative Nb and Ti anomalies whereas the third specimen has a flat, N-MORB-like pattern. The presence of negative Nb and Ti anomalies in basaltic rocks is typically equated with those rocks having formed in or adjacent to subduction complexes. The close association of rocks having MORB-like compositions, rocks with minor negative Nb and Ti anomalies, and light-REE-enriched calc-alkaline basaltic andesites is similar to that described by Wood et al. (1981) for rocks recovered from deep-sea drilling in the Mariana back-arc trough. We suggest, therefore, that basaltic rocks of the

Yathkyed greenstone belt, including those from both the upper and lower tectonostratigraphic units, may represent oceanic crust generated in an ensimatic back-arc basin.

Nd isotopic analyses imply that all the mafic volcanic rocks were generated from melting of isotopically juvenile mantle sources, comparable to, or slightly less depleted than, the hypothetical depleted mantle of the time. However, two samples in particular, one each from the upper and lower tectonostratigraphic units, exhibit lower ε_{Nd} values than the remainder of the rocks. These data suggest that some older crust may have been involved in their petrogenesis. This possibility will be examined in more detail with further whole-rock and Nd isotopic analyses of rocks collected during the 1998 field season. The juvenile character of the volcanogenic sedimentary rocks indicates that they were probably derived from local detritus comparable in composition to the basalts with which they are intercalated and that a significantly older crustal component was not present.

ACKNOWLEDGMENTS

We are indebted to the analytical staff of the Analytical Chemistry and Geochronological laboratories of the Geological Survey of Canada. Reg Thériault and Bill Davis were instrumental in the chemical separation of Nd isotopes and mass spectrometry. Bill Davis and Jim Ryan kindly reviewed the manuscript.

REFERENCES

Davis, W.J., Hanmer, S., Peterson, T.D., Rainbird, R., Ryan, J.J., and Sandeman, H.A.I.
1998: Preliminary U-Pb geochronology of volcanic rocks in the Kaminak belt, Western Churchill Province, Kivalliq region, Northwest Territories; 26th Yellowknife Geoscience Forum, Program and Abstracts of Talks and Posters, 25–27 November, 1998, p. 30.

Eade, K.E.
1986: Precambrian geology of the Tulemalu Lake–Yathkyed Lake area, District of Keewatin; Geological Survey of Canada, Paper 84-11, 31 p.

Goldstein, S.L., O'Nions, R.K., and Hamilton, P.J.
1984: Sm-Nd isotopic study of atmospheric dusts and particulates from major river systems; Earth and Planetary Science Letters, v. 32, p. 178–196.

Hoffman, P.F.
1988: United Plates of America, the birth of a craton: Early Proterozoic assembly and growth of Laurentia; Annual Review of Earth and Planetary Sciences, v. 16, p. 543–603.

Irvine, T.N. and Barager, W.R.A.
1971: A guide to the chemical classification of the common volcanic rocks; Canadian Journal of Earth Sciences, v. 8, p. 523–548.

Jacobsen, S.B. and Wasserburg, G.J.
1980: Sm-Nd isotopic evolution of chondrites; Earth and Planetary Science Letters, v. 50, p. 139–155.

Kay, R.W. and Hubbard, N.J.
1978: Trace elements in ocean ridge basalts; Earth and Planetary Science Letters, v. 38, p. 95–116.

LeBas, M.J., LeMaitre, R.W., Streckeisen, A., and Zanettin, B.
1986: A chemical classification of volcanic rocks based on the total alkali silica diagram; Journal of Petrology, v. 27, p. 745–750.

Loveridge, W.D., Eade, K.E., and Sullivan, R.W.
1988: Geochronological studies of Precambrian rocks from the southern District of Keewatin; Geological Survey of Canada, Paper 88-18, 36 p.

Machado, N., Brooks, C., and Hart, S.R.
1986: Determination of initial ^{87}Sr/^{86}Sr and ^{143}Nd/^{144}Nd in primary minerals from mafic and ultramafic rocks: experimental procedure and implications for the isotopic characteristics of the Archean mantle under the Abitibi greenstone belt, Canada; Geochimica et Cosmochimica Acta, v. 50, p. 2335–2348.

Miyashiro, A.
1974: Volcanic rock series in island arcs and active continental margins; American Journal of Science, v. 274, p. 321–355.

Pearce, J.A.
1982: Trace element characteristics of lavas from destructive plate boundaries; *in* Andesites, (ed.) R.S. Thorpe; John Wiley and Sons, p. 525–548.

Pearce, J.A. and Norry, M.J.
1979: Petrogenetic implications of Ti, Zr, Y, and Nb variations in volcanic rocks; Contributions to Mineralogy and Petrology, v. 69, p. 33–47.

Relf, C., Irwin, D., MacLachlan, K., and Mills, A.
1998: New insights into the geology of the Yathkyed greenstone belt, western Churchill Province, Northwest Territories; *in* Current Research 1998-C; Geological Survey of Canada, p. 67–75.

Relf, C., MacLachlan, K., and Irwin, D.
1999: Tectonic assembly and Proterozoic reworking of the northern Yathkyed greenstone belt, Northwest Territories (Nunavut); *in* Current Research 1999-C; Geological Survey of Canada, p. 139–146.

Richard, P., Shimuzu, N., and Allègre, C.J.
1976: ^{143}Nd/^{146}Nd, a natural tracer: an application to oceanic basalts; Earth and Planetary Science Letters, v. 31, p. 269–278.

Roeder, P.L. and Emslie, R.F.
1970: Olivine-liquid equilibrium; Contributions to Mineralogy and Petrology, v. 29, p. 275–289.

Sun, S.S. and McDonough, W.F.
1989: Chemical and isotopic systematics of oceanic basalts: implications for mantle composition and processes; *in* Magmatism in the Ocean Basins, (ed.) A.D. Saunders and M.J. Norry; Geological Society Special Publication no. 42, p. 313–345.

Thériault, R.J. and Tella, S.
1997: Sm-Nd isotopic study on mafic volcanic rocks from the Rankin Inlet and Tavani regions, District of Keewatin, Northwest Territories; *in* Radiogenic and Isotopic Studies, Report 10; Geological Survey of Canada, Current Research 1997-F, p. 61–66.

Wood, D.A., Marsh, N.G., Tarney, J., Joron, J.L., Fryer, P., and Treuil, M.
1981: Geochemistry of igneous rocks recovered from a transect across the Mariana Trough, Arc, Fore-arc, and Trench, sites 453 through 461, Deep Sea Drilling Project Leg 60; *in* Initial Report of the Deep Sea Drilling Project, (ed.) D.M. Hussong, S. Uyeda, R. Blanchet, U. Bleil, C.H. Ellis, T.J.G. Francis, P. Fryer, K. Horai, S. Kling, A. Meijer, K. Nakamura, J.H. Natland, G.H. Packham, and A. Sharaskin, v. 60, p. 611–645; United States Government Printing Office, Washington, D.C.

– 6 –

Geochemical and Sm-Nd isotopic study of Paleoproterozoic basaltic and gabbroic rocks of the Hurwitz Group, Kaminak Lake area, Kivalliq region, Northwest Territories[1]

C.J. Hemmingway[2] and H.A. Sandeman[3]

Hemmingway, C.J. and Sandeman, H.A., 1999: Geochemical and Sm-Nd isotopic study of Paleoproterozoic basaltic and gabbroic rocks of the Hurwitz Group, Kaminak Lake area, Kivalliq region, Northwest Territories; in *Radiogenic and Isotope Studies: Report 12; Geological Survey of Canada, Current Research 1999-F, p. 53–62.*

Abstract: Basaltic and gabbroic rocks of the Ameto Formation comprise part of the Paleoproterozoic Hurwitz Group and are considered to be 2111 Ma, based on their correlation with Hurwitz Group gabbros southwest of the study area. Volcanic rocks are locally pillowed and are interlayered with mudstone, siltstone, and diamictite, all cut by gabbroic sills. Igneous rocks preserve variably developed foliations and a low-grade metamorphic mineral assemblage implying deformation and metamorphism at greenschist facies. Major-, trace-, and rare-earth-element geochemical data demonstrate a homogeneous suite of tholeiitic basalts with affinities to both continental and volcanic-arc tholeiites. The gabbroic rocks are intrusive equivalents of the basalts. Values of $\varepsilon_{Nd(2.111\ Ga)}$ range from -0.54 to +0.25 and yield T_{DM} ages of 2598 to 2508 Ma. The combined data suggest that parental magmas were at least in part derived from a metasomatically enriched mantle source and that metasomatism occurred immediately after accretion of the Neoarchean Kaminak greenstone belt.

Résumé : Les roches basaltiques et gabbroïques de la Formation d'Ameto contiennent une partie du groupe paléoprotérozoïque de Hurwitz. En se basant sur leur corrélation avec les gabbros du Groupe de Hurwitz situés au sud-ouest de la région étudiée, leur âge serait de 2 111 Ma. Par endroits, les roches volcaniques ont une structure en coussins et sont interstratifiées avec des mudstones, des siltstones et de la diamictite, le tout étant entrecoupé par des filons-couches gabbroïques. Les roches ignées ont conservé des foliations diversement développées et un assemblage de minéraux de faible métamorphisme, laissant supposer qu'elles ont été déformées et métamorphisées dans le faciès des schistes verts. Des données géochimiques sur les éléments majeurs, les éléments traces et les éléments de terres rares indiquent un cortège homogène de basaltes tholéiitiques montrant des affinités avec les tholéiites continentales et d'arc volcanique. Les roches gabbroïques sont les équivalentes intrusives des basaltes. Les valeurs de $\varepsilon_{Nd(2,111\ Ga)}$ s'échelonnent de -0,54 à +0,25 et indiquent des âges T_{DM} de 2 598 à 2 508 Ma. Les données regroupées laissent supposer que les magmas parentaux sont dérivés, du moins en partie, d'une source mantellique enrichie par la métasomatose qui s'est produite immédiatement après l'accrétion de la ceinture de roches vertes néo-archéennes de Kaminak.

---

[1] Contribution to the Western Churchill NATMAP Project

[2] 1–206, boulevard du Plateau, Hull, Quebec J9A 3G2

[3] Geological Survey of Canada, 601 Booth Street, Ottawa, Ontario K1A 0E8

INTRODUCTION

The Paleoproterozoic Hurwitz Group of the western Churchill Province comprises a thick sequence of clastic and chemical sedimentary and rare mafic volcanic rocks that were deposited in a large, shallow, intracratonic basin (Aspler and Chiarenzelli, 1997). Geochemical and isotopic analysis of contained mafic volcanic members and spatially related gabbroic sills can further elucidate the tectonic setting and evolution of this basin.

The mafic volcanic rocks of the Ameto Formation, formally designated the Happotiyik Member (Bell, 1970), constitute a lithostratigraphic unit forming the deep-water facies of the predominantly shallow marine, Paleoproterozoic Hurwitz Group. The type section through the Ameto Formation, approximately 45 km southwest of Carr Lake, comprises a 244 m thick package dominated by mudstone and siltstone with the Happotiyik Member representing only a ca. 26 m thick unit (Bell, 1970). West of the type section, the Happotiyik Member does not outcrop and is presumed to pinch out. In the Kaminak Lake area (NTS 55L) to the northeast, however, the Ameto Formation is up to 518 m thick with the Happotiyik Member making up as much as 305 m.

This study originated in 1997 as part of the Western Churchill NATMAP Project and was designed to examine field, petrographic, and geochemical characteristics of the mafic volcanic rocks and gabbroic sills of the Hurwitz Group. This paper reports the first comprehensive, whole-rock geochemical and Nd isotopic data for the mafic volcanic rocks of the Happotiyik Member and associated gabbroic sills. These data will help in the examination of the origin and tectonomagmatic significance of these rocks in the greater western Churchill Province.

GEOLOGICAL SETTING

The study area, proximal to Kaminak and Quartzite lakes, is in the northeastern part of the Ennadai-Rankin greenstone belt (Fig. 1) of the Hearne Province (Hoffman, 1988). The Hurwitz Group in the study area (Fig. 2) overlies greenschist-grade Archean supracrustal and granitoid rocks of the Kaminak Group (Davidson, 1970). Archean rocks of the Kaminak Group mainly comprise mafic to felsic volcanic rocks, although local to regional occurrences of banded iron-formation, siliciclastic sedimentary rocks, and voluminous debris flows associated with felsic volcanic centres are common (Hanmer et al., 1998). Intruding the Kaminak Group are

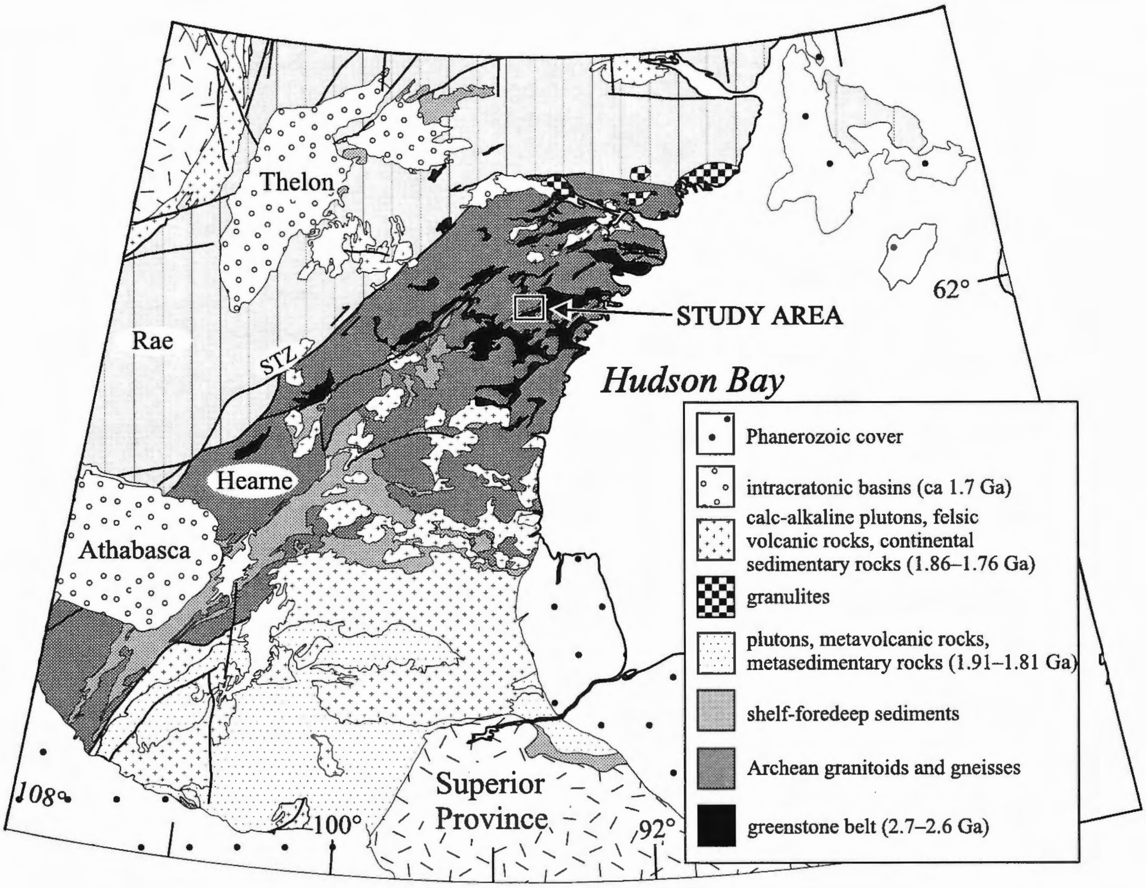

Figure 1. *Simplified geological map of the north-central Canadian Shield showing the location of the study area (Kaminak–Quartzite lakes) in the western Churchill Province (modified from Hoffman, 1988).*

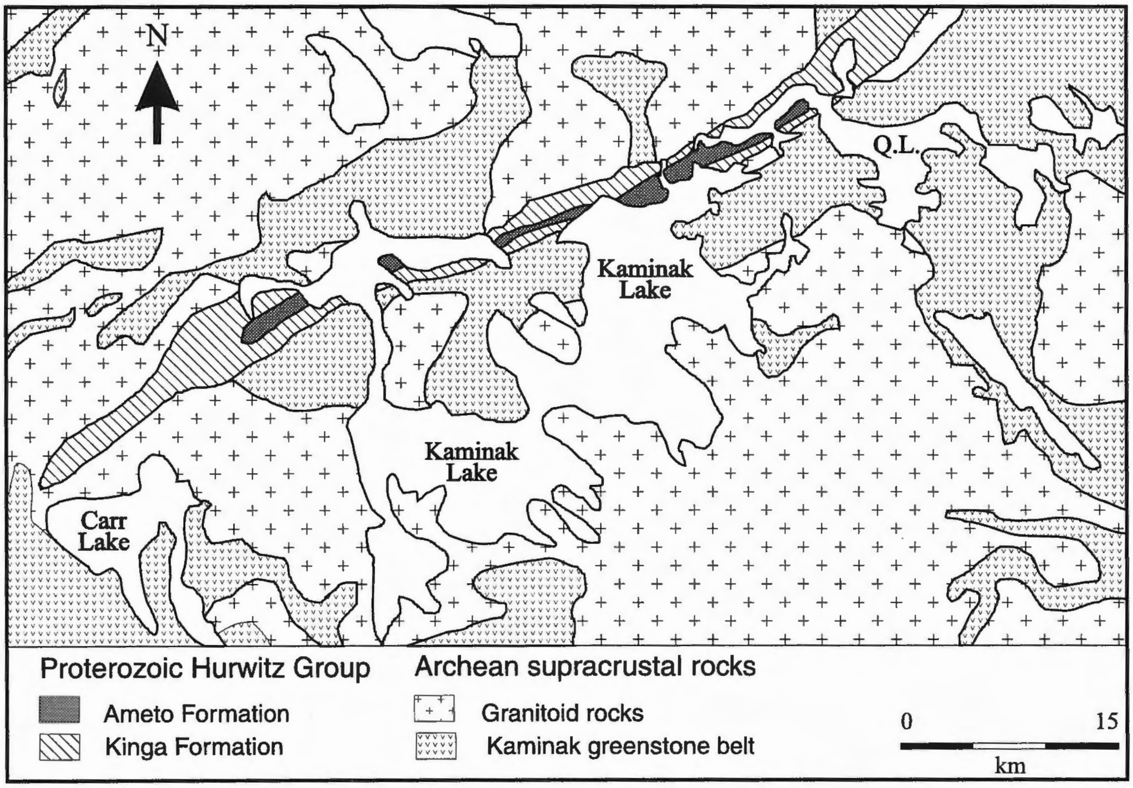

Figure 2. *Generalized geology of the Kaminak–Quartzite lakes area (modified from Hanmer et al., 1998).*

a wide range of Neoarchean plutonic rocks, ranging in composition from gabbro to syenogranite. The Archean rocks of the study area are intruded by a suite of 2450 Ma (Heaman, 1994), northeast-trending diabase dykes (Kaminak dykes; Christie et al., 1975), all of which are overlain by the Proterozoic Hurwitz Group (Davidson, 1970).

The Hurwitz Group represents the erosional remnants of an extensive, relatively shallow, Paleoproterozoic, intracratonic basin now preserved as a series of outliers across the Hearne Province in an area covering ca. 14 000 km² (Aspler and Chiarenzelli, 1996, 1997). A maximum age of 2450 Ma for the Hurwitz Group is implied by U-Pb dating of baddeleyite in the Kaminak dykes (Heaman, 1994), whereas a U-Pb baddeleyite age of 2111 ± 1 Ma from gabbroic sills in the Ameto Formation provides a minimum age of deposition for the Hurwitz Group (Heaman and LeCheminant, 1993). Deformation of the Hurwitz Group occurred subsequent to intrusion of the 2111 ± 1 Ma gabbro sills, but prior to intrusion of the ca.1830 Ma lamprophyre dykes associated with the ultrapotassic lavas of the Baker Lake basin (Tella et al., 1985; Roddick and Miller, 1994; MacRae et al., 1995).

Hurwitz Group stratigraphy

The Hurwitz Group is divided into the Noomut, Padlei, Kinga, Ameto, Watterson, Ducker, and Tavani formations (Fig. 3). The lower part of the stratigraphy, the Noomut, Padlei, and Kinga formations, represents a conformable onlap sequence

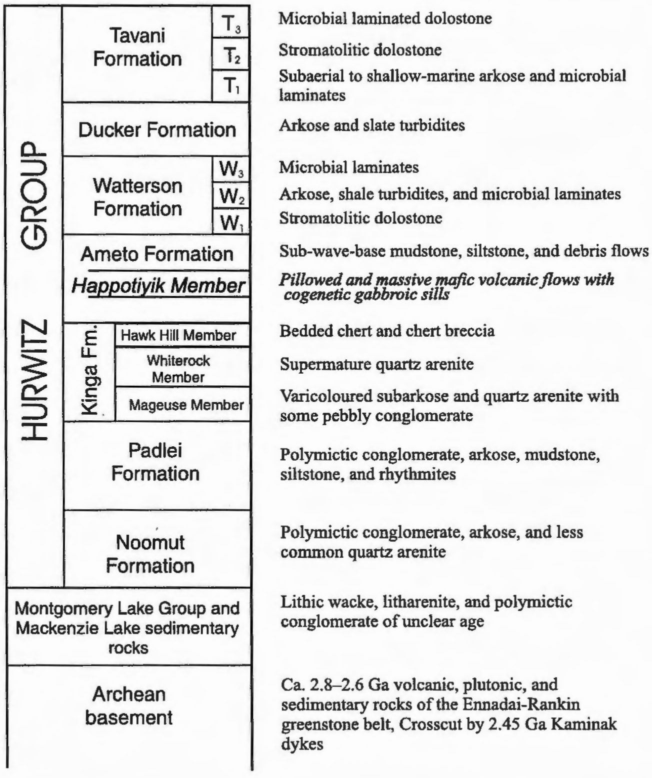

Figure 3. *Simplified composite stratigraphic section of the Hurwitz Group (after Aspler and Chiarenzelli, 1997).*

that spreads out radially from a centre southwest of the Kaminak Lake area. The upper part of the stratigraphy, the Ameto, Watterson, Ducker, and Tavani Formations, defines an offlap sequence (Aspler and Chiarenzelli, 1997). The abrupt, but conformable, change from the conglomerate and quartz arenite typical of the lower part of the Hurwitz Group to the mudstone and siltstone of the Ameto Formation represents a sudden deepening of the basin.

The Happotiyik Member, a unit of massive and pillowed mafic volcanic flows (Bell, 1970), represents an integral part of the Ameto Formation in the Kaminak Lake area. Gabbro sills, intrusive into the Ameto Formation, are considered coeval with the upper part of the Happotiyik Member (Bell, 1970) because of their documented presence as feeder dykes to the mafic flows and their general restriction to the Ameto Formation. Although the gabbro sills typically are not observed to crosscut other units of the Hurwitz Group, Bell (1968) describes a gabbro dyke, in an area on the east side of the north arm of Quartzite Lake, that crosscuts the Whiterock Member of the Kinga Formation at a shallow angle to bedding. Aspler and Chiarenzelli (1997) described angular, Ameto Formation xenoliths within the gabbros and a lack of soft-sediment deformation structures in the sedimentary rocks of the Ameto Formation immediately adjacent to the sills, suggesting that the Hurwitz Group was well lithified prior to their emplacement.

FIELD AND PETROGRAPHIC OBSERVATIONS

The rocks of the Hurwitz Group contain mineral assemblages characteristic of greenschist-facies metamorphic rocks, but for simplicity, all rock types will hereinafter be referred to by their protolith name. The Happotiyik Member comprises pillowed and massive mafic flows and is associated spatially with sills of Hurwitz Group gabbro, all of which are intercalated over metre-scale intervals with mudstone, siltstone, and diamictite of the Ameto Formation. The development of moderate to intense cleavage, combined with the tendency of the sedimentary rocks to weather out preferentially, commonly obscures contact relationships.

The massive mafic flows tend to be very fine grained, medium to dark green, and essentially featureless in outcrop, although rare, 0.2–10.0 mm plagioclase phenocrysts may comprise <1–2 per cent of the rock. Pillowed flows are common throughout the area, but lichen cover prevents reliable, systematic determination of younging directions. The pillowed flows tend to weather medium to dark green-brown, similar to the massive flows. Pillow sizes range from approximately 30 to 50 cm on average in their long dimension, with aspect ratios of about 2:1. The pillows have thin, 1–2 cm thick selvages and commonly contain chert in the interstices. Except for rare plagioclase phenocrysts, the pillows are devoid of internal structure. In thin section, the very fine grain size and the metamorphic character of the massive and pillowed flows hamper the establishment of precise modal mineralogy; however, the major constituent minerals can be identified. Plagioclase, actinolite, and epidote form the coarsest grained phases in the volcanic rocks. Identification of groundmass phases is less certain, but these include chlorite, fine-grained plagioclase, and minor muscovite.

The gabbroic rocks tend weather light green to medium green and are typically fine- to medium-grained, massive, and featureless, except for heterogeneously distributed ≤10 mm plagioclase phenocrysts. The gabbros are generally inequigranular and fine- to medium-grained in thin section. Primary igneous textures are rarely preserved, except in less altered samples that exhibit relict ophitic and subophitic textures. Other primary igneous textures have been destroyed by the metamorphic growth of minerals such as chlorite, biotite, and epidote. The dominant mineral composition, typical of low-grade greenschist-facies mafic rocks, is actinolite+plagioclase (albite)+chlorite+epidote+biotite±leucoxene±ilmenite±muscovite±pyrite±chalcopyrite. Quartz is found in very small quantities in the groundmass and in veinlets, where it can occur in equal amounts with epidote.

GEOCHEMISTRY

Analytical methods

Representative, fresh, unweathered specimens comprising three mafic volcanic and three gabbroic rocks, were crushed using a Braun Chipmunk jaw-crusher and then pulverized to a fine, homogeneous powder using an agate ring mill. Major-element geochemical composition was determined by X-ray fluorescence (XRF) on fused discs at the Geological Survey of Canada. The concentrations of the transition metals Cr, Ni, Co, Sc, V, Cu, Zn, and Be were determined by inductively coupled plasma-emission spectrometry (ICP-ES) at the Geological Survey of Canada. The concentrations of some trace elements (Nb, Rb, Sr, Y, Zr, Ga) were determined by XRF on pressed-powder discs at McGill University, Montréal. The remaining trace- and rare-earth-element (REE) analyses presented in Table 1 were determined by inductively coupled plasma-mass spectrometry (ICP-MS) at Memorial University of Newfoundland.

Analytical procedures for Sm-Nd analyses are a variant of those employed by Richard et al. (1976). Whole-rock powders (ca. 0.2 g) were spiked with a ^{148}Nd-^{149}Nd mixed solution and dissolved in teflon bombs in a warm HF-HNO_3 solution. Once dissolution was complete, the bombs were inserted into steel jackets and placed in a furnace at 170°C for five days. The bombs were removed and the solutions were dried down using a hot plate. The rare-earth elements were converted to chloride complexes through addition of 6 N HCl to each bomb and all bombs were returned to the steel jackets and placed in the furnace (T = 170°C) for 12 hours.

Neodymium and samarium were separated using wet-chemical chromatographic methods, ultra-pure acids, and conventional, cation-specific separation resins. Isotopic ratios were determined by thermal ion mass spectrometry using a Finnigan Mat 261 mass spectrometer run in the static mode. Neodymium isotopic compositions were normalized to ^{146}Nd/^{144}Nd = 0.7219 and corrected to La Jolla

Table 1. Rock type, location (eastings and northings; UTM zone 15) and major-, trace-, and rare-earth-element data for samples of the Happotiyik Member and associated gabbroic rocks from the Kaminak Lake area. Major-element oxides in wt %; trace elements and rare-earth elements in ppm; b/dl indicates an element concentration below detection limit; LOI indicates volatiles lost on ignition.

Sample Rock type Easting Northing	**H439 gabbro 381347 6908681**	**H442 gabbro 379815 6909734**	**C227 gabbro 390295 6910987**	**C211 pillow basalt 415102 6920530**	**C216b basalt flow 412897 6919566**	**C224 pillow basalt 391188 6911135**
SiO_2	49.3	48.1	51.3	50.6	49.8	51.2
TiO_2	0.99	1.15	1.51	0.94	1.15	1.15
Al_2O_3	14.4	14.7	13.2	14.3	14.4	14.1
Fe_2O_3	2.5	3.2	3.1	2.7	3.7	1.8
FeO	8.9	9.0	10.8	8.8	8.1	9.7
MnO	0.18	0.19	0.22	0.24	0.19	0.19
MgO	7.99	7.15	4.76	6.98	6.82	6.93
CaO	9.69	9.91	9.62	10.37	9.37	7.09
Na_2O	2.6	2.5	2.2	2.3	2.5	4.0
K_2O	0.45	0.19	0.61	0.42	0.49	0.29
P_2O_5	0.10	0.12	0.16	0.10	0.12	0.12
LOI	2.0	2.3	1.5	1.7	2.1	1.9
Total	99.1	98.5	99.0	99.5	98.7	98.5
Cr	290	220	64	190	230	210
Ni	160	110	48	85	100	100
Co	54	52	55	52	50	55
Sc	32	36	37	36	34	34
V	240	270	330	260	260	250
Cu	100	81	180	95	160	120
Pb	2.8	3.8	5.4	3.2	7.7	2.1
Zn	58	72	110	61	64	74
Mo	0.6	0.7	1.0	1.3	0.8	0.5
Rb	13	5	22	10	12	5
Cs	0.6	b/dl	3.8	0.4	1.5	0.3
Ba	121.0	69.9	146.0	238.9	107.5	184.7
Sr	175	210	184	192	181	115
Tl	0.1	b/dl	0.2	0.1	0.1	b/dl
Ga	17	19	19	16	18	16
Ta	0.3	0.3	0.5	0.3	0.3	0.3
Nb	6	7	8	7	7	7
Hf	2.1	2.0	3.1	2.0	2.0	2.0
Zr	79	94	126	76	97	96
Y	21	24	30	21	24	23
Th	1.4	1.5	1.8	1.5	1.5	1.6
U	0.3	0.4	0.5	0.4	0.4	0.4
Be	b/dl	b/dl	0.6	0.5	0.5	b/dl
La	9.44	10.07	14.12	9.11	10.69	9.71
Ce	20.64	23.60	31.11	20.19	23.86	22.97
Pr	2.93	3.29	4.53	2.75	3.30	3.20
Nd	12.39	14.30	18.83	11.55	13.76	13.14
Sm	3.18	3.63	4.65	3.00	3.49	3.31
Eu	1.07	1.20	1.57	0.98	1.10	0.96
Gd	3.69	4.10	5.69	3.31	4.16	3.88
Tb	0.59	0.68	0.83	0.58	0.65	0.63
Dy	3.70	4.24	5.52	3.58	4.10	4.02
Ho	0.75	0.89	1.13	0.72	0.84	0.82
Er	2.09	2.42	2.98	2.09	2.27	2.22
Tm	0.27	0.34	0.45	0.29	0.33	0.31
Yb	1.69	1.97	2.57	1.69	1.91	1.90
Lu	0.27	0.28	0.39	0.26	0.27	0.25

$^{143}Nd/^{144}Nd$ = 0.511860. Repeated analysis of an internal laboratory Nd AMES metal solution yielded $^{143}Nd/^{144}Nd$ = 0.512165 ± 0.000020 (2σ: n = 15). Values of ε_{Nd} were calculated using a present-day chondritic uniform reservoir (CHUR) composition of $^{143}Nd/^{144}Nd$ = 0.512638 and $^{147}Sm/^{144}Nd$ = 0.1967. The 2σ reproducibility of the ε_{Nd} values is calculated to be ca. ±0.5 ε units. The Nd isotopic data for the six samples are presented in Table 2.

Alteration

Isotopic, major-, trace-, and rare-earth-element analyses are presented for six samples, including pillowed and massive volcanic rocks from the Happotiyik Member and associated gabbroic sills. The samples show some effects of alteration, with total volatile content exceeding 2 wt. % in two of the samples.

The volcanic and gabbroic rocks have a typical greenschist-facies mineral assemblage of actinolite+albite ±chlorite±epidote and it is possible, therefore, that elements known to be mobile in aqueous solution (e.g. Na, K, Ca, Ba, Rb, Sr, and to some degree the light rare-earth elements [LREEs]) were redistributed during metamorphism. However, the homogeneity of the major elements suggests that they have not been redistributed to a degree that renders them inadequate for use in the chemical classification of rock types. The intersample coherency in the major-, trace-, and rare-earth-element data suggests that the elemental abundances of these rocks reflect primary igneous compositions.

Major- and trace-element geochemical composition

The mafic rocks of the Happotiyik Member are basaltic and, with few exceptions, little intersample variation exists in major-element compositions. On the total alkalies versus SiO_2 diagram of Le Bas et al. (1986), the six samples plot as a tight cluster in the basaltic field (Fig. 4) with SiO_2 ranging from 48.1 to 51.2 wt % (Table 1). They exhibit typical tholeiitic iron-enrichment trends on a total-iron (as FeO^T)-MgO--alkali diagram (Fig. 5) after Irvine and Barager (1971). Magnesium numbers (Mg number: molecular MgO/MgO+FeO^T) range from 0.52 to 0.56, indicating only minor intersample differentiation. Sample C227, however, has an anomalously low Mg number of 0.38 compared to other samples, suggesting that, with a larger data set, significant intersuite differentiation might be observed. Mafic volcanic rocks of the Happotiyik Member and associated gabbroic rocks are depleted in the elements Cr (64–290 ppm) and Ni (48–160 ppm) (Table 1) relative to melts derived directly from asthenospheric mantle. This depletion indicates that either their parental magmas underwent fractional crystallization in crustal magma chambers or they assimilated lower crustal material depleted in those elements.

Although the data set is small, the major-element oxides, with the exception of TiO_2 and P_2O_5, plot as tight clusters on variation diagrams when MgO or SiO_2 are used as a fractionation index and therefore are not very useful in determining fractionation trends. Variation diagrams of TiO_2 and P_2O_5 and all other high-field-strength elements (HFSEs) (Nb, Y, Zr, Th, Ta, and REEs) versus MgO (not shown) demonstrate essentially negative linear covariation of these elements with MgO, suggesting that the specimens are related through fractional crystallization.

The REE profiles for the six specimens are parallel, exhibit negative slopes, and rise uniformly with inferred fractionation (Fig. 6). The La_N/Yb_N ratios range from 6.19 to 7.78 (normalizing values from Sun and McDonough, 1989), indicating a moderate enrichment in the LREEs. Sample C227 shows significantly higher abundances of HFSEs and

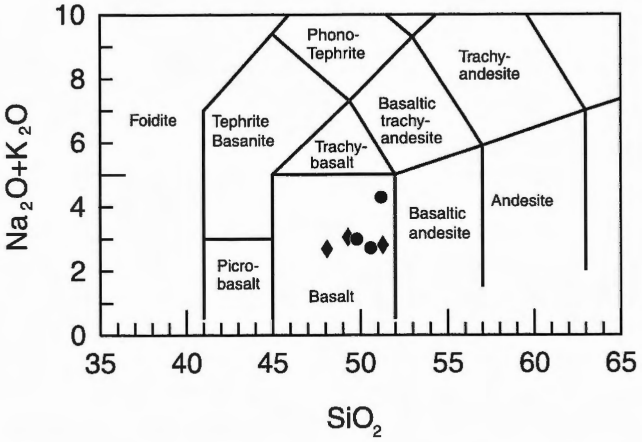

Figure 4. *The total alkalies versus SiO_2 classification diagram for the volcanic rocks of the Happotiyik Member and associated gabbros (after Le Bas et al., 1986). Diamonds = gabbroic rocks; circles = volcanic rocks*

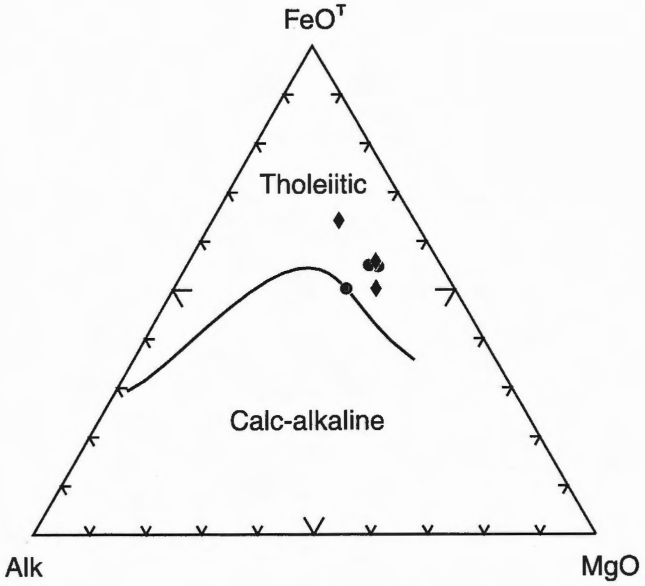

Figure 5. *FeO^T-Alk-MgO plot (after Irvine and Barager, 1971) for specimens of the Happotiyik Member and associated Hurwitz Group gabbros. Diamonds = gabbroic rocks; circles = volcanic rocks.*

REEs on this diagram than the other samples, which, combined with its low Mg number, indicates that it may represent a more evolved melt. The Th/Nb ratios (0.214–0.233) do not seem to correlate with MgO, Cr, or Ni values, suggesting that the mantle source has had a greater influence on the abundances of Th and Nb than either crustal contamination or fractional crystallization. The elements Nb, Ta, and Ti are depleted relative to other elements in all samples, a feature that is characteristic of magmas generated at volcanic arcs (Pearce, 1982), but is also observed in some continental tholeiites (Thompson et al., 1984).

Nd isotopic data

The six samples from the Happotiyik Member and associated gabbros yielded present-day $^{143}Nd/^{144}Nd$ ratios of 0.511900 to 0.512027 and corresponding $\varepsilon_{Nd(t\,=\,2111\ Ma)}$ values of -0.54 to + 0.25 (Fig. 7, Table 2). These values cluster in and around the chondritic uniform reservoir (CHUR), a feature characteristic of many continental tholeiites and in particular of continental flood basalts and associated dyke swarms (Thompson et al., 1984; Turner and Hawkesworth, 1995). The samples yielded T_{DM} ages (time of extraction from a

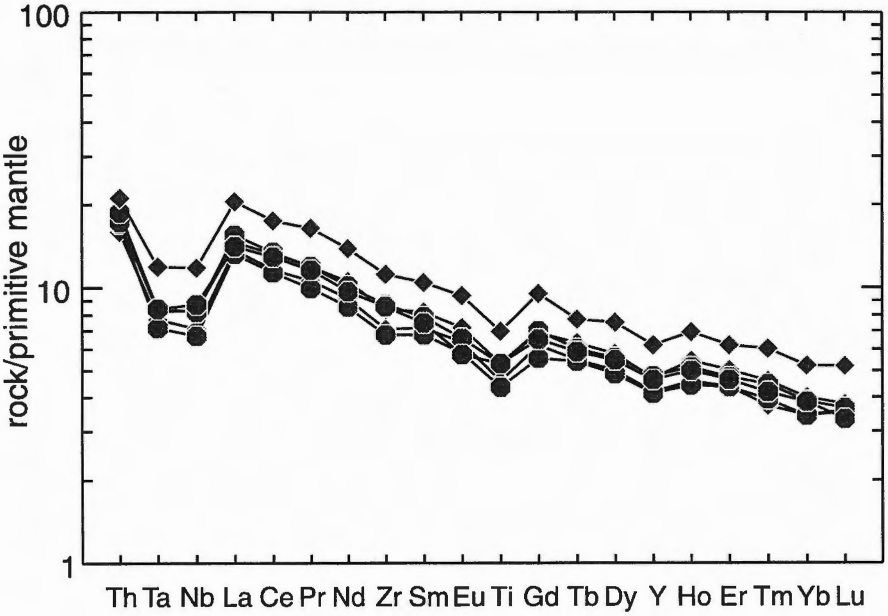

Figure 6.

Primitive-mantle-normalized REE diagram for the six samples analyzed (normalizing values from Sun and McDonough, 1989). Diamonds = gabbroic rocks; circles = volcanic rocks

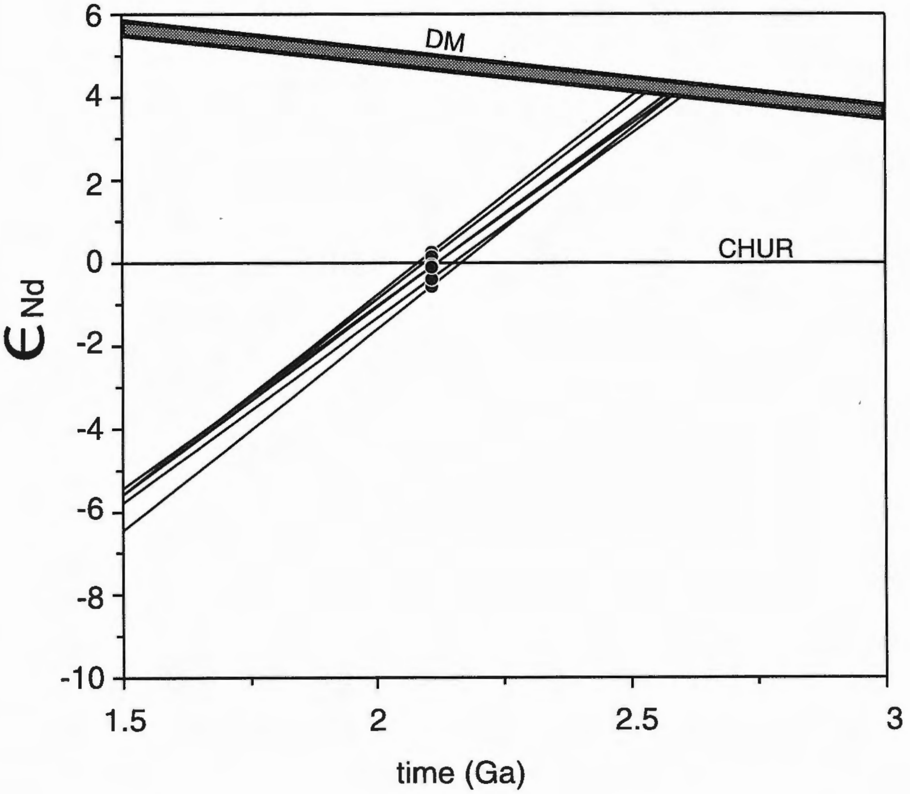

Figure 7.

ε_{Nd} versus time plot showing the Nd isotopic evolution lines for the six samples from the Happotiyik Member and associated gabbroic sills. T_{DM} ages calculated according to the model of DePaolo (1981). DM = depleted mantle evolution line; CHUR = chondritic uniform reservoir

Table 2. Neodymium isotope data for six samples of basaltic and gabbroic rocks of the Hurwitz Group. T_{DM} ages calculated after DePaolo, 1981.

Sample	Sm (ppm)	Nd (ppm)	$^{147}Sm/^{144}Nd$ measured	$^{143}Nd/^{144}Nd$ measured	$^{143}Nd/^{144}Nd$ at t = 2111 Ma	ε_{Nd}	T_{DM}(Ma)
C216B	3.43	13.89	0.1496	0.511996	0.509917	0.254	2508
C211	2.89	12.02	0.1456	0.511900	0.509876	-0.544	2580
C224	3.16	12.47	0.1530	0.512027	0.509900	-0.076	2576
C227	4.67	18.69	0.1512	0.512013	0.509912	0.158	2531
H442	3.28	13.04	0.1520	0.512013	0.509900	-0.061	2566
H439	2.96	11.89	0.1508	0.511980	0.509884	-0.377	2598

depleted mantle source) of 2598–2508 Ma (DePaolo, 1981), model ages that are slightly less than the age of formation of the mafic juvenile crust of the Neoarchean Kaminak greenstone belt (Mortensen and Thorpe, 1987; Davis et al., 1998) whose units form the basement to the Hurwitz Group. These data indicate that basalts of the Ameto Formation and associated gabbroic sills were derived, at least in part, from a mantle source that underwent metasomatic enrichment in incompatible trace elements immediately after accretion of the Neoarchean Kaminak belt.

DISCUSSION

Implications of field and petrographic observations

Field observations imply that the Happotiyik Member comprises a suite of mafic volcanic rocks that were erupted in a deep-water environment as pillowed and massive flows. Field relationships in the study area are ambiguous and it is unclear whether the gabbros are coeval with the volcanic rocks (as high-level sills or feeder dykes to the volcanic rocks) or whether they postdate the volcanism.

The intercalation of volcanic rocks with mudstone and, locally, black shale indicates that magmas were erupted in pulses during active sedimentation. Assuming that the mudstone and shale were deposited over relatively long periods, these interruptions imply that the volcanic rocks of the Happotiyik Member and their associated gabbroic sills were emplaced episodically over a moderately protracted time interval. This is a feature apparently at odds with their remarkably homogeneous chemical and isotopic compositions.

Except for rare occurrences of ophitic and subophitic textures in some gabbro specimens, most primary igneous textures were destroyed by greenschist facies metamorphism. Scanning electron microscope (SEM) analyses demonstrate that the plagioclase is albitic and the amphiboles actinolitic, confirming greenschist-facies metamorphism.

Implications of whole-rock geochemical analyses

The whole-rock analyses of these rocks reveal a suite of tholeiitic volcanic and gabbroic rocks that have homogeneous isotopic compositions and parallel, incompatible-trace-element profiles. The significance of this observation is that it demonstrates the compositional coherency of the basaltic flows; moreover, it suggests that the widespread gabbroic sills in the Hurwitz Group are intrusive equivalents of the volcanic flows, particularly in the study area.

The six samples analyzed exhibit little intersample variation in major-element compositions. The high SiO_2 contents, low Mg numbers, and low abundances of the transition metals, in particular Cr and Ni, demonstrate that these mafic rocks are not primary asthenospheric mantle melts. Tectonic discrimination diagrams (not shown) based on major and trace elements cannot discriminate between either a continental or volcanic-arc setting for these rocks.

Negative linear covariance between the HFSEs and MgO imply that the six samples are related through fractional crystallization of a chemically similar, perhaps common, parental magma.

Although the presence of negative Nb and Ta anomalies and enrichment of the large-ion lithophile elements (LILEs) relative to the HFSEs is characteristic of volcanic-arc magmas, the intracratonic, basinal setting of the rocks of the Happotiyik Member and Hurwitz Group gabbros, in conjunction with an absence of geological elements characteristic of volcanic arcs, indicates that these magmas were not formed in an arc setting; they more likely represent a suite of continental tholeiites with arc-like characteristics (*see* Carlson, 1991).

Although the petrogenesis of continental flood basalts has received much attention in the literature, controversy about their origin is widespread. Various models have ascribed the enriched geochemical and primordial isotopic characteristics of these rocks to subcrustal mixing of distinct, mantle-derived magmas, commonly oceanic-island basalt and mid-ocean ridge basaltic melts. The somewhat evolved major element and compatible trace element compositions, however, are typically attributed to assimilation-fractional crystallization processes in the lower crust (*see* discussions in Thompson et al. [1984], Boily and Ludden [1991], and Turner and Hawkesworth [1995]). The preliminary data presented herein demonstrates the 'volcanic-arc-like' trace-element signatures of basaltic rocks of the Ameto Formation and associated gabbroic sills and indicates that these were derived, at least in part, from a LILE- and LREE-enriched mantle source. The corresponding Nd isotopic data lend support to this conclusion and, furthermore, constrain enrichment of the subcrustal mantle to have occurred at ca. 2600–2500 Ma, immediately after accretion of the Neoarchean Kaminak greenstone belt. Further constraints on the origin of these rocks awaits additional whole-rock geochemical and Nd isotopic investigation followed by petrogenetic modelling of the possible processes involved in the generation of mafic rocks of the Ameto Formation.

CONCLUSIONS

Field relationships between the mafic flows and sills of the Happotiyik Member and the sedimentary rocks of the Ameto Formation imply that volcanic units were emplaced in a deep-water environment. Petrographic features including a mineral assemblage dominated by actinolite+chlorite+albite and only rare relict primary igneous textures indicate that the flows and sills have been metamorphosed at low-grade, greenschist-facies conditions. Major-, trace-, and rare-earth-element geochemical data demonstrate that both the volcanic rocks of the Happotiyik Member and the gabbroic rocks of the Hurwitz Group are tholeiitic and that the gabbros are probably intrusive equivalents of the basalts. The six samples exhibit negative covariation trends between the HFSEs and MgO, a feature attributed to fractional crystallization of a common parental magma.

Although these rocks have geochemical characteristics similar to both continental and volcanic-arc tholeiites, the intracratonic basinal setting predicates the former. The ε_{Nd} values cluster near the chondritic uniform reservoir, a feature common to continental flood basalts and associated dyke swarms. T_{DM} ages of 2598–2508 Ma suggest that metasomatic enrichment of the mantle source, in LILEs and REEs, occurred sometime prior to eruption, apparently subsequent to formation of the Kaminak greenstone belt. Derivation from a mantle source region beneath the Hearne Province is inferred, at least in part, and this lithospheric mantle was metasomatized immediately after accretion of the Neoarchean greenstone belt.

ACKNOWLEDGMENTS

Yannick Beaudoin, Thomas Hadlari, and Jim Ryan are thanked for their assistance in the field. Brian Cousens of Carleton University assisted in the interpretation of the geochemical data. Thomas Skulski and Otto van Breemen are thanked for their insightful reviews. The analytical staff at the Geological Survey of Canada is thanked for providing the whole-rock geochemical data.

REFERENCES

Aspler, L.B. and Chiarenzelli, J.R.

1996: Relationship between the Montgomery Lake and Hurwitz groups, and stratigraphic revision of the lower Hurwitz Group, District of Keewatin; Canadian Journal of Earth Sciences, v. 33, p. 1243–1255.

1997: Archean and Proterozoic geology of the North Henik Lake area, District of Keewatin, Northwest Territories; *in* Current Research 1997-C; Geological Survey of Canada, p. 145–155.

Bell, R.T.

1968: Preliminary notes on the Proterozoic Hurwitz Group, Tavani (55K) and Kaminak Lake (55L) areas, District of Keewatin; Geological Survey of Canada, Paper 68-36, 16 p.

1970: Preliminary notes on the Hurwitz Group, Padlei map area, Northwest Territories; Geological Survey of Canada, Paper 69-52, 13 p.

Boily, M. and Ludden, J.N.

1991: Trace-element and Nd isotopic variations in Early Proterozoic dyke swarms emplaced in the vicinity of the Kapuskasing structural zone: enriched mantle or assimilation and fractional crystallization (AFC) process?; Canadian Journal of Earth Sciences, v. 28, p. 26–36.

Carlson, R.W.

1991: Physical and chemical evidence on the cause and source of flood basalt volcanism; Australian Journal of Earth Sciences, v. 38, p. 525–544.

Christie, K.W., Davidson, A., and Fahrig, W.F.

1975: The paleomagnetism of Kaminak dikes — no evidence of significant Hudsonian plate motion; Canadian Journal of Earth Sciences, v. 12, p. 2048–2064.

Davidson, A.

1970: Precambrian geology, Kaminak Lake map area, District of Keewatin; Geological Survey of Canada, Paper 69-51, 27 p.

Davis, W.J., Hanmer, S., Peterson, T.D., Rainbird, R., Ryan, J.J., and Sandeman, H.A.I.

1998: Preliminary U-Pb geochronology of volcanic rocks in the Kaminak belt, western Churchill Province, Kivalliq region, Northwest Territories; 26th Yellowknife Geoscience Forum, Program and Abstracts of Talks and Posters, 25–27 November, 1998, p. 30 (abstract).

DePaolo, D.J.

1981: Neodymium isotopes in the Colorado Front Range and crust-mantle evolution in the Proterozoic; Nature, v. 291, p. 193–196.

Hanmer, S., Peterson, T.D., Sandeman, H.A., Rainbird, R.H., and Ryan, J.J.

1998: Geology of the Kaminak greenstone belt from Padlei to Quartzite Lake, Kivalliq region, Northwest Territories; *in* Current Research 1998-C; Geological Survey of Canada, p 85–94.

Heaman, L.M.

1994: 2.45 Ga global mafic magmatism: Earth's oldest superplume?; *in* Abstracts of the 8th International Conference on Geochronology, Cosmochronology, and Isotope Geology, (ed.) M.A. Lanphere, G.B. Dalrymple, and B.D. Turrin; United States Geological Survey, Circular 1107, p. 132.

Heaman, L.M. and LeCheminant, A.N.

1993: Paragenesis and U-Pb systematics of baddeleyite (ZrO_2); Chemical Geology, v. 110, p. 95–126.

Hoffman, P.F.

1988: United Plates of America, the birth of a craton: Early Proterozoic assembly and growth of Laurentia; Annual Review of Earth and Planetary Science Letters, v. 16, p. 543–603.

Irvine, T.N. and Barager, W.R.A.

1971: A guide to the chemical classification of the common volcanic rocks; Canadian Journal of Earth Sciences, v. 8, p. 523–548.

Le Bas, M.J., LeMaitre, R.W., Streckeisen, A., and Zanettin, B.

1986: A chemical classification of volcanic rocks based on the total alkali silica diagram; Journal of Petrology, v. 27, p. 745–750.

MacRae, N.D., Armitage, A.E., and Jones, A.L.

1995: A diamondiferous lamprophyre dike, Gibson Lake area, Northwest Territories; International Geology Review, v. 37, p. 212–229.

Mortensen, J.K. and Thorpe, R.I.
1987: U-Pb zircon ages of felsic volcanic rocks in the Kaminak Lake area, District of Keewatin; Geological Survey of Canada, Paper 87-2, p. 123–128.

Pearce, J.A.
1982: Trace element characteristics of lavas from destructive plate boundaries; *in* Andesites, (ed.) R.S. Thorpe; John Wiley and Sons, p. 525–548.

Richard, P., Shimuzu, N., and Allègre, C.J.
1976: $^{143}Nd/^{146}Nd$, a natural tracer: an application to oceanic basalts; Earth and Planetary Science Letters, v. 31, p. 269–278.

Roddick, J.C. and Miller, A.R.
1994: An ^{40}Ar-^{39}Ar age from the REE-enriched Enetatcha ultrapotassic intrusive suite and implications for timing of ultrapotassic magmatism in the central Churchill Structural Province, Northwest Territories; *in* Radiogenic Age and Isotopic Studies: Report 8; Geological Survey of Canada, Current Research 1994-F, p. 69–74.

Sun, S.S. and McDonough, W.F.
1989: Chemical and isotopic systematics of oceanic basalts: implications for mantle composition and processes; *in* Magmatism in the Ocean Basins, (ed.) A.D. Saunders and M.J. Norry; Geological Society Special Publication no. 42, p. 313–345.

Tella, S., Heywood, W.W., and Loveridge, W.D.
1985: A U-Pb age on zircon from a quartz syenite intrusion, Amer Lake, District of Keewatin, NWT; *in* Current Research, Part B; Geological Survey of Canada, Paper 85-1B, p. 367–370.

Thompson, R.N., Morrison, G.L., Hendry, G.L., and Parry, S.J.
1984: An assessment of the relative roles of crust and mantle in magma genesis: an elemental approach; Philosophical Transactions of the Royal Society of London, v. 310, p. 549–590.

Turner, S. and Hawkesworth, C.
1995: The nature of the subcontinental mantle: constraints from the major element composition of continental flood basalts; Chemical Geology, v. 120, p. 295–314.

Other publications containing age and isotopic data generated in the GSC Geochronology Laboratory

Anderson, R.G., Whalen, J.B., and Villeneuve, M.E.

1998: Triassic to Eocene composite intrusions and molybdenum metallogeny: the Endako Batholith redefined; *in* New Geological Constraints on Mesozoic to Tertiary Metallogenesis and on Mineral Exploration in Central British Columbia: Nechako NATMAP Project; Geological Association of Canada Cordilleran Section Short Course, Geological Association of Canada, Vancouver, British Columbia.

Bingen, B. and van Breemen, O.

1998: U-Pb monazite ages in amphibolite- to granulite-facies orthogneiss reflect hydrous mineral breakdown reactions: Sveconorwegian Province of SW Norway; Contributions to Mineralogy and Petrology, v. 132, p. 336–353.

Bingen, B., Demaiffe, D., and van Breemen, O.

1998: The 616 Ma old Egersund basaltic dyke swarm, SW Norway, and Late Neoproterozoic opening of Iapetus Ocean; Journal of Geology, v. 106, p. 565–574.

Chiarenzelli, J., Aspler, L., Villeneuve, M., and Lewry J.

1998: Early Proterozoic evolution of the Saskatchewan Craton and its allochthonous cover Trans-Hudson Orogen; Journal of Geology, v. 106, p. 247–267.

Clark, A.H., Scott, D.J., Sandeman, H.A.I., Bromley, A.V., and Farrar, E.

1998: Siegenian generation of the Lizard ophiolite: U-Pb zircon age data for plagiogranite, Porthkerris, Cornwall; Journal of the Geological Society, London, England, v. 155, p. 595–598.

Corkery, M.T. and Skulski, T.

1998: Geology of the Little Stull Lake area (part of NTS 63K/10 and 7); *in* Manitoba Energy and Mines, Geological Services, Report of Activities, 1998, p. 111–118.

Corriveau, L., Rivard, B., and van Breemen, O.

1998: Rheological controls on Grenvillian intrusive suites: implications for tectonic analysis; Journal of Structural Geology, v. 20, p. 1191–1204.

Currie, K.L., Whalen, J.B., Davis, W.J., Longstaffe, F.J., and Cousens, B.L.

1998: Geochemical evolution of peraluminous plutons in southern Nova Scotia, Canada — a pegmatite-poor suite; Lithos, v. 44, p. 117–140.

Evenchick, C.A., Crawford, M.L., McNicoll, V.J., Currie, L.D., and O'Sullivan, P.B.

1999: Early Miocene or younger normal faults and other Tertiary structures in west Nass River map area, northwest British Columbia, and adjacent parts of Alaska; *in* Current Research 1999-A; Geological Survey of Canada, p. 1–11.

Evenchick, C.A., McNicoll, V.J., Holm, K., Alldrick, D.J., and Snyder, L.D.

1997: Geology, Anyox Pendant and surrounding areas, Observatory Inlet (103P/5), and parts of Hastings Arm (103P/12) and 103O/9 map areas, British Columbia; Geological Survey of Canada, Open File map 3453, scale 1:50 000.

Hinners, T.A., Hughes, R. Outridge, P.M., Davis, W.J., Simon, K., and Woolard, D.R.

1998: Interlaboratory comparison of mass spectrometric methods for lead isotopes and trace elements in NIST SRM 1400 Bone Ash; Journal of Analytical Atomic Spectrometry, v. 13, p. 963–970.

Percival, J.A., Castonguay, S., Whalen, J.B., Brown, J.L., McNicoll, V., and Harris, J.R.

1999: Geology of the central Wabigoon region in the Sturgeon Lake–Obonga Lake corridor, Ontario; *in* Current Research 1999-C; Geological Survey of Canada, p. 197–208.

Rainbird, R.H., Stern, R.A., Khudoley, A.K., Kropachev, A.P., Heaman, L.M., and Sukhorukov, V.I.

1998: U-Pb geochronology of Rhipean sandstone and gabbro from southeast Siberia and its bearing on the Laurentia-Siberia connection; Earth and Planetary Science Letters, v. 164, p. 409–420.

Rogers, N., van Staal, C.R., and McNicoll, V.

1999: Recent advances in the geology and structure of the Confederation Lake region, northwestern Ontario; *in* Current Research 1999-C; Geological Survey of Canada, p. 187–195.

Sanborn-Barrie, M. and Skulski, T.

1999: Tectonic assembly of continental margin and oceanic terranes at 2.7 Ga in the Savant Lake–Sturgeon Lake greenstone belt, Ontario; *in* Current Research 1999-C; Geological Survey of Canada, p. 209–220.

Scott, D.J.

1999: U-Pb geochronology of the eastern Hall Peninsula, southern Baffin Island, Canada: a northern link between the Archean of West Greenland and the Paleoproterozoic Torngat Orogen of northern Labrador; Precambrian Research, v. 93, p. 5–26.

Scott, D.J. and St-Onge, M.R.

1998: Paleoproterozoic assembly of NE Laurentia revisited: a model based on southward extrapolation of Ungava-Baffin crustal architecture; *in* Report of 1998 ECSOOT Transect Meeting, (ed.) R.J. Wardle and J. Hall; LITHOPROBE Report 68, p 134–147.

Scott, D.J., Stern, R.A., and St-Onge, M.R.

1997: An overview of the geochronology of detrital zircons in Paleoproterozoic metasedimentary rocks, southern Baffin Island; *in* Report of ECSOOT Transect Meeting, LITHOPROBE Workshop Report 61, p. 181–185.

Skulski, T. and Villeneuve, M.

1999: Geochronological compilation of the Rae and Hearne provinces; Geological Survey of Canada, Open File D3706, 1 diskette.

1999: Geochronological compilation of the Superior Province; Geological Survey of Canada, Open File D3715, 1 diskette.

Stern, R.A.

1998: High-resolution SIMS determination of radiogenic tracer-isotope ratios in minerals; *in* Modern Approaches to Ore and Environmental Mineralogy, (ed.) L.J. Cabri and D.J. Vaughan; Mineralogical Association of Canada, Short Course Series, v. 27, p. 241–268.

Stern, R.A. and Bleeker, W.

1998: Age of the world's oldest rocks refined using Canada's SHRIMP: the Acasta Gneiss Complex, Northwest Territories, Canada; Geoscience Canada, v. 25, p. 27–31.

St-Onge, M.R., Scott, D.J., Wodicka, N., and Lucas, S.B.

1998: Crustal architecture of the Trans-Hudson Orogen in northern Quebec and southern Baffin Island: plate margin configuration between 2.04 and 1.76 Ga; *in* Report of 1998 ECSOOT Transect Meeting, (ed.) R.J. Wardle and J. Hall; LITHOPROBE Report 68, p. 151–166.

Thériault, R.J.

1998: Nd and Pb isotopic and geochemical framework of Paleoproterozoic southern Baffin Island, and comparisons with other segments of the eastern Trans-Hudson Orogen; *in* Eastern Canadian Shield Onshore-Offshore Transect (ECSOOT), (comp.) R.J. Wardle and J. Hall; The University of British Columbia, LITHOPROBE Secretariat, Report 68, p. 170–187.

Villeneuve, M.E. and Relf, C.

1998: Tectonic setting of 2.6 Ga carbonatites in the Slave Province, northwest Canada; Journal of Petrology, v. 39, p. 1975–1986.

Wodicka, N., St-Onge, M.R., Scott, D.J., and Lucas, S.B.

1998: Timing and nature of tectonothermal events in the Quebec–Baffin segment of Trans-Hudson Orogen: comparisons with Cordilleran models; *in* Eastern Canadian Shield Onshore-Offshore Transect (ECSOOT), (comp.) R.J. Wardle and J. Hall; The University of British Columbia, LITHOPROBE Secretariat, Report 68, p. 188–206.

Zaleski, E, Duke, N., L'Hereux, R., Davis, W.J., and Wilkinson, L.

1999: Clastic and chemical sedimentary sequences, Woodburn Lake group, Amarulik Lake to Tehek Lake, western Churchill Province, Northwest Territories (Nunavut); *in* Current Research 1999-C; Geological Survey of Canada, p. 19–28.

Zaleski, E, L'Hereux, R., Duke, N., Wilkinson, L., and Davis, W.J.

1999: Komatiitic and felsic volcanic rocks overlain with quartzite, Woodburn Lake group, Meadowbank River area, western Churchill Province, Northwest Territories (Nunavut); *in* Current Research 1999-C; Geological Survey of Canada, p. 9–18.

AUTHOR INDEX

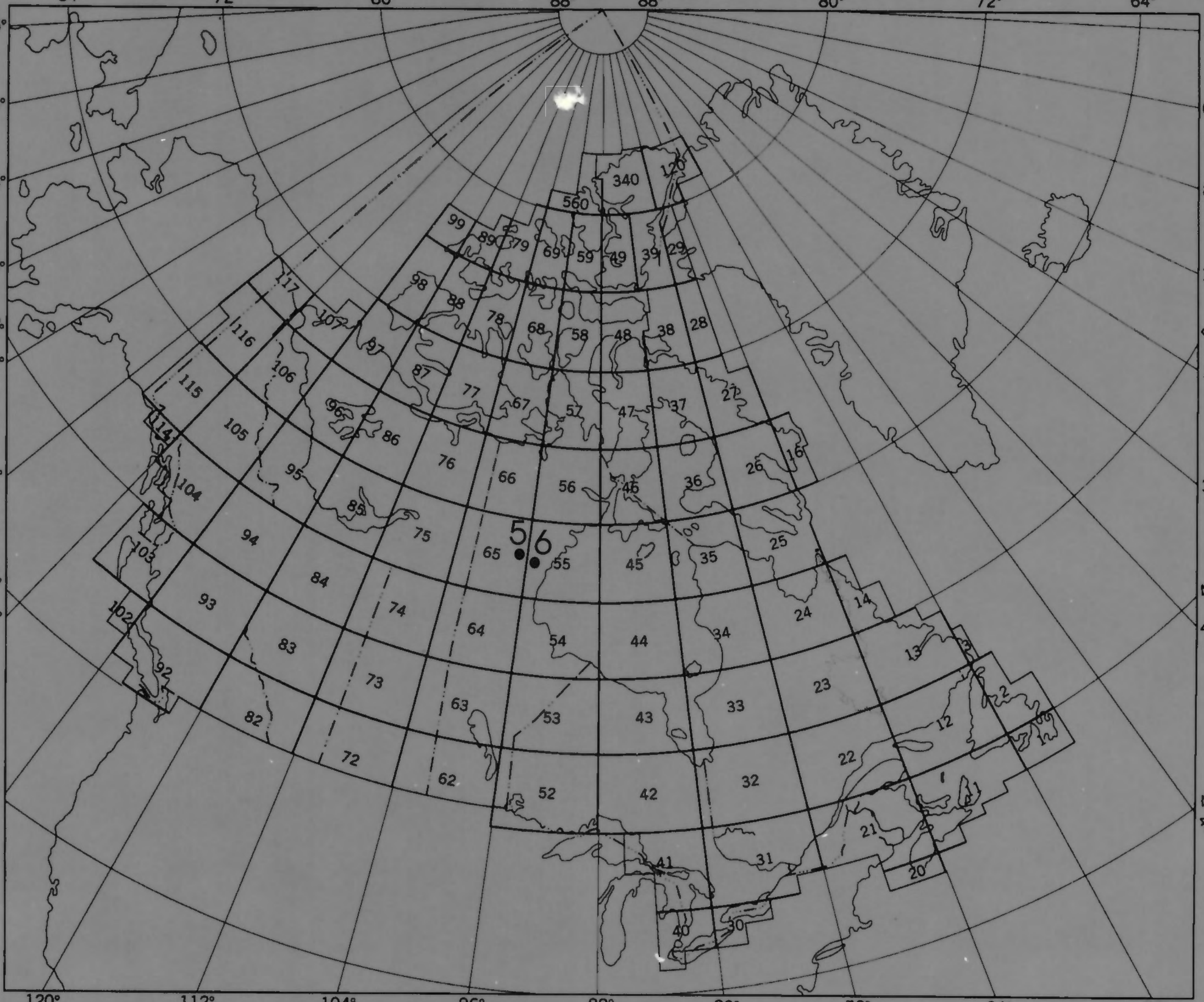

Locations on the map refer to reports in this volume
Les localités indiquées sur la carte correspondent aux rapports contenus dans le présent volume